DALHOUSIE UNIVERSITY

To comply with the Canadian Privacy Act the National Library of Canada has requested that the following pages be removed from this copy of the thesis:

Preliminary Pages
- Examiners Signature Page
- Dalhousie Library Copyright Agreement

Appendices
- Copyright Releases (if applicable)

A Higher Precision Technique for Modelling Wave-body Interactions

by

Mahmoud Ghiasi

Submitted
in partial fulfillment of the requirements
for the degree of

DOCTOR OF PHILOSOPHY

Major Subject: Mechanical Engineering (Naval Architecture)

DALHOUSIE UNIVERSITY

Halifax, Nova Scotia December, 2004

Your file Votre référence
ISBN: 0-494-02118-7
Our file Notre référence
ISBN: 0-494-02118-7

Contents

List of Tables

List of Figures

NOMENCLATURE

A_{WP} : water plane area of a ship

$\bar{A}$: added-mass

$\overline{A}$: mass matrix

$\bar{B}$: damping coefficient

$\overline{B}$: damping coefficient matrix

$\overline{C}$: matrix of restoring force

C_p : pressure coefficient

F_j : radiated wave force of the jth mode of motion

F_w : wave exciting force

F^D : diffracted wave force

F^I : incident wave force

F_n : Froude number

g : gravitational accelaration

G_{st} : Green's function for steady motion

G_{db} : double body Green's function

G_I : Green's function of image

G_w : wave part of Green's function

H, h : submergence depth

I_{WP} : moment of inertia of water plane

L: length of the body

L_w: wave length

M_{WP} : moment of water plane

$\overline{M}$: generalized mass matrix

$\mathcal{N}_{i,p}$: pth degree of B-spline basis function

$NURBS$: Non-Uniform Rational B-Spline

$oxyz$: steady moving coordinate system

$OXYZ$: body-fixed coordinate system

$\bar{o}\bar{x}\bar{y}\bar{z}$: space fixed coordinate system

P_i : control point in the NURBS surface

p_r : radiated wave pressure

p_w : diffrected wave pressure

S_b : body boundary

S_F : free surface boundary

S_R : boundary at infinity

U : steady forward speed of the body

W : velocity vector of the steady flow

$\overline{\Phi}$, ϕ_T : total velocity potential

ϕ_d : disturbance potential

$\bar{\phi}_D$, ϕ_D : diffracted wave potential

ϕ_I : incident wave potential

Φ_s : steady disturbance potential

Φ : unsteady potential

$\bar{\phi}_j$, ϕ_j : radiated wave potential in jth mode

ψ : strem function

ρ : density of water

λ_{ii} : non-dimensional damping coefficient

μ_{ii} : non-dimensional added-mass

∇ : volume displacement of a ship

Δs : distance between two consecutive points

ω : wave frequency

ω_e : frequency of encounter

$\bar{\omega}$: weighting factor

Γ : vortex strength

ν : wave number

η : wave elevation

η_j : amplitude of the jth mode of motion

ACKNOWLEDGEMENTS

I would like to express my gratitude to God who has given me the power to carry out this work. Further, I wish to express my sincere thanks to my supervisor Professor M.R. Islam for his supervision. Also, thanks to my co-supervisor Professor M. Kujath and other members of my supervisory committee, Professor M. Rahman and Professor J. Militzer. In addition, I express my great appreciation and thanks to Professor S. Calisal as the external examiner for this thesis.

I would like to thank my friend Dr. H. Basirat Tabrizi for his suggestions. My special thanks extend to my wife, daughters and my family for their support, patience and understanding throughout this course of study.

The support provided by Iranian Ministry of Culture and Higher Education is greatly appreciated.

ABSTRACT

This dissertation consists of two parts. In the first part, the desingularized Cauchy's formula is derived to solve the two-dimensional potential flow problem in an infinite domain. The Gaussian quadrature is applied to discretize the desingularized Cauchy's formula. An efficient method for implementation of Kutta condition is developed. Finally, formulations of fully nonlinear free surface flow past a two-dimensional body are also developed.

In the second part, the desingularized formulation of the problem of a ship advancing through regular waves is presented. Traditionally, ship motion problems are investigated by using either two-dimensional strip theory or three-dimensional panel method. In the desingularized formulation, the singularity involved in the Rankine source of the integral equation is removed by using the "adding and subtracting back" technique. The Gaussian quadrature is applied to distribute the source on the body surface. In general, the body surface of a ship has no mathematical description. Therefore, the Non-Uniform Rational B-Spline (NURBS) surface is employed to model the body surface.

The influence of the desingularized formulation is demonstrated by computing hydrodynamic coefficients and wave exciting forces of several mathematically defined bodies and some ship hulls. The comparisons between the present numerical solutions and existing analytical results demonstrate the superiority of the desingularized method compared to the panel method. A series of computations are carried out and compared with the experimental results and numerical results published in the literature.

PART ONE:

THE NUMERICAL SOLUTION OF TWO-DIMENSIONAL WATER-WAVE PROBLEMS USING CAUCHY'S FORMULA

Chapter 1

Introduction

1.1 Wave-Body Interactions

Potential flow methods are widely used to analyze two- and three-dimensional wave-body interaction. Common applications of two-dimensional potential flow problems are to study the hydrodynamic properties of arbitrary bodies or lifting surfaces, such as, hydrofoils, rudder and keels. Two-dimensional solutions of potential flow problems can be extended by means of strip theories to solve three-dimensional wave-body interaction. Study of ship behavior in water waves, sea-keeping and manoeuvring are the area of interest for potential flow applications.

Many theories and methods have been developed to predict the behavior of a ship advancing with constant steady forward speed in water waves. The problem can be solved by experimental observations of a ship model or by developing hydrodynamic theories to predict ship behavior in waves. Theoretical approaches are often adopted in

the early stages of ship design, due to the fact that they are less costly than experimental approaches and also they provide a comprehensive explanation for ship behaviors in a particular wave. In developing a theoretical model of ship motion in water waves, the spectral representation of sea waves is commonly used. This method was introduced by St. Denis and Pierson [66] in their spectral representation of sea waves. They assumed that the water motion could be described as the sum of many simple sinusoidal waves. The response of the ship to each sinusoidal wave can be obtained by classical formulas of water waves. The response of the ship is then the sum of its response to the various components which can be found by the spectrum method.

The potential flow theory has been widely employed by researchers to analyze two- and three-dimensional wave-body interactions. Analytical solutions of potential flow problems can be obtained for few simple three-dimensional geometries through the application of the theory of multi-pole expansion. The multi-pole expansion theory was developed by Ursell [70]. Newman [48], Wu [75], Hulme [20] and Rahman [54, 55] successfully applied it to various geometries, including submerged or floating sphere, spheroid and circular cylinder. Kokkinowrachos *et al* [31] also applied the method to the analysis of hydrodynamics of arbitrary shaped bodies of revolution with vertical axis of revolution in which the velocity potential is expressed by Jacobis's expansion.

In the theory of multi-pole expansion, velocity potentials are expressed in terms of an infinite series of polynomials with unknown coefficients. The unknown coefficients are obtained by imposing the body surface conditions. Due to complexity of the ship body geometry, this method is rarely used for computation of ship hydrodynamic

characteristics.

For the general body shapes, such as the shapes of ships, submarines, and offshore structures, the numerical methods are commonly adopted. Different numerical approaches, namely, finite element, finite difference, and boundary element methods are developed to solve the potential flow problems. For the exterior domain, the boundary element methods are usually preferred because these methods decrease the dimensionality of the problems and, therefore, decrease the computational effort. Moreover, computation based on the finite difference and finite element can become more costly since the exterior domain of the computation extends to infinity. However, the boundary integral method, only requires the discretization of the boundary surface and, therefore, needs a smaller computational effort.

Linear and nonlinear theories have been developed to solve the ship motion problems. The measured and computed free-surface elevation along the hull for the Wigley hull at Froude numbers between 0.26 and 0.32 obtained by several researchers such as Kime and Locase [29], Kim [28] and Maruo and Song [43]. Hendrix [14] compared these elevations and showed that the results of nonlinear methods are not generally in better agreement with the experimental measurements than the linear solutions. The comparison of differences among linear predictions and nonlinear predictions suggests that the errors due to numerical computation or discretization are more important than the nonlinearities of the problem as discussed by Hendrix [14]. In spite of this fact, the linear theory has limitations when considering the extreme motions. For instance, according to Inglis [23], the roll motion of a ship may be quite nonlinear and

the nonlinearity must be considered particularly in prediction of roll amplitude near resonance.

In general, two different theories, the strip theory and the three-dimensional theory have been developed to solve ship motion problems. The strip theory is based upon the slender theory in which the beam and draught of the ship are assumed to be small compared to the length of the ship. In the strip theory, each cross-section of the ship is considered to be a part of an infinitely long cylinder. By solving two-dimensional potential flow problem for each cross-section and integrating the two-dimensional solutions over the length of the ship, the three-dimensional solutions are obtained as described by Journee [24]. Since each cross-section is considered separately, some effects which can significantly influence the results, are lost. For example, the interaction between one part of the ship hull and another part or the flow at the bow and the stern of the ship which cannot be adequately treated. The strip theories are usually validated through calibrating the theoretical results with model experiments. In general, it has been found that, the results obtained by most theories agree quite well with each other and with experiments at zero forward speed, but the differences occur at higher speeds as indicated by Journee [24] and Inglis [23].

The varieties of three-dimensional formulation have been developed without any restriction on the body geometry. Most of these formulations used the boundary integral methods, to solve the potential flow around ships moving in water waves. For numerical solutions of integral equations different panel methods have been commonly used. The panel method was originally presented by Hess and Smith [16].

In the panel method, the body surface is divided into a number of panels. Each panel can be defined as a plane or a quadratically curved surface. Constant or linear function source density values are distributed over each panel. The strength of the sources which are primary unknown are then calculated from the boundary condition on the body surface. In the plane panel method, by locating a singularity with an unknown constant strength on the centroid of each panel, a system of linear equations can be obtained from the integral equations for solving the unknown strength. The accuracy of the solutions depend directly, on the number of panels, on the body surface, and a large number of panels are required to obtain the accurate solutions for hydrodynamic problems especially for complex geometries. Although the implementation of constant panel method is simple, the computational effort increases when large number of panel are taken into consideration and sometimes the difficulty in convergence of the solution also occur. Hess and Smith [16], Webster [71]and Söding [65] used plane panels. In a different numerical scheme used by Kehr and Chou [26], the panels are defined quadratically which are better for representing curved surfaces. Comprehensive reviews of panel methods have been made by Atkinson [1] and Hunt [21]

All above panel methods use an approximation of the body surface and the errors are produced due to this approximation. An additional error is also introduced by assuming a simple source density distribution over each panel. If the geometrical data used for the numerical computation are taken to be as accurate as possible and if the number of collocation points on each panel can be chosen to be adjustable to the curvature of each panel, then the accuracy of the computation can be improved.

The idea of developing the higher-order panel methods is to increase the accuracy of the solution of integral equations. In other word, in the higher-order panel methods, the equivalent accuracy of constant panel methods can be obtained by less number of panels. The body surface is approximated by a number of panels where the panel can be defined by interpolating polynomials through a mesh of points located on the surface of the body. A higher-order panel method based on source distribution and Gaussian quadrature to solve potential flow problem was presented by Kouh *et al* [32]. They used Gaussian quadrature to discretize the integral equation over the body surface. These Gaussian points were calculated from the mathematical surface definition of the body surface and the source densities were determined at these points. The high order panel method based on interpolation of triangular and rectangular panels with quadratic polynomials have also been used by Atkinson [1] and Xü [76].

The higher-order panel method based on the B-spline to solve the potential flow problems have been developed and used by several researchers. For example, Maniar [40] presented a three-dimensional higher-order panel method based on B-spline and investigated the accuracy of different panel method. The same approach was used by Lee *et al* [38]. It was shown that the method is very accurate and efficient for solving a variety of potential problems.

Generally, in the boundary integral equation method (also known as surface source distribution method or Green function method), the numerical models are based on the distribution of source on the submerged portion of the body surface. Green's theorem is applied to derive the integral equations in the domain of the body surface.

Three distinct numerical problems must be overcome to implement this approach and to obtain accurate solutions of hydrodynamic problems for three-dimensional bodies. First, the body surface which in general has no mathematical description must be described with a reasonable accuracy so that the collocation points can be placed precisely on the body surface. In the panel method, the body surface is approximated by the panels and a large number of panels are utilized to carry out a good approximation.

The second numerical problem is the evaluation of the source potential and its derivatives in performing hydrodynamic computation for three-dimensional bodies. Wehausen and Laitone [72] , Newman [49] and Telste and Noblesse [68] gave the mathematical expression for the oscillatory source potential for finite and infinite depth of the fluid.

The third numerical difficulty in solving the boundary integral equations for potential flow arising from the singular behavior of the kernel functions involved in the equations. Different methods have been developed in the past to deal with the singular behavior of the kernel functions for easing the computation of boundary integral equations. However, the most commonly-used desingularization scheme in potential problem is the "subtracting and adding back" technique. In this technique, a function is subtracted from the integrand so that the resultant kernel becomes non singular and then the integration function is added to the equation.

1.2 Objectives and Scope of the Present Work

The two main objectives of this work are:

- To formulate a consistent fully nonlinear method for potential flow of two-dimensional body moving beneath the free surface using desingularized Cauchy's formula and to investigate the accuracy of this method.

  The accurate numerical solutions can be obtained by using the desingularized Cauchy's formula. The Gaussian quadrature can be applied to discretize the integral equations. Since there is no assumption for linearization of the problem in developing the Cauchy's formula, the fully nonlinear solutions for free surface problems can be investigated.

- To formulate a higher precision technique, for numerical modelling of ship motion, with steady forward speed in regular waves and to investigate the accuracy of this technique.

Two types of Green's functions can be used to develop three-dimensional theories for computation of wave body interactions, the forward-speed Green's function and zero-speed Green's function. The main difficulty in applying the forward-speed Green's function is due to the oscillatory part of integral in the Green's function, which requires very long computing time in order to obtain an accurate result. Since, the intervals of the discretized integral have to be very small. Also, it is mentioned by Hsiung and Huang [18] that the accurate and converged solutions were more difficult to obtain with Green's function of forward-speed than in the case of zero-speed Green's function.

The formulation of wave-body interactions can be further developed by using desingularization technique for more accurate results of the problem. This study follows first by presenting the desingularized formulation for numerical solutions of potential flow in infinite domain. Hence, the desingularized formula is applied for computation of the disturbance and total velocity potential. The Gaussian quadrature is used to discretize the integral equations. In order to implement the Kutta condition for a hydrofoil, the iteration method is employed by setting the pressure differences between closed neighboring collocation points to the trailing edge in the upper and lower parts of the hydrofoil. The pressure difference has to be very small (close to zero).

Further, the formulation of fully nonlinear free surface flow past a two-dimensional hydrofoil using desingularized Cauchy's formula is derived. Then, the numerical simulation of ellipses and hydrofoils in infinite domain as well as numerical simulation of a hydrofoil shaped body traveling beneath the free surface are carried out and the result are given in Chapter 3.

In Chapter 4, the linear formulation for a ship advancing with steady forward speed in water waves is presented. This formulation is based on the usage of zero-speed Green' s function and forward speed correction. Then, the radiation and diffraction of a submerged or floating body with zero speed in regular waves is formulated. The singularities in the integral equations are removed using desingularized technique to obtain a desingularized form of the integral equations. The advantage of desingularization of the integral equations before the discretization is that, the integrals can be directly applied to the exact boundary geometry. The desingularized integral equa-

tions are discretized using proper Gaussian quadrature in which the Gaussian points are selected as the collocation points.

To obtain the parameters, i.e., coordinates and normal at the collocation points, an accurate description of the body surface is required. Non Uniform Rational B-Spline (NURBS) surface representation is employed to describe the three-dimensional arbitrary body shape.

In Chapter 5, the discretized integral equations are applied to compute the hydrodynamic coefficients of mathematically defined body with zero forward speed for which the analytical solution are available. Simulation studies are carried out for motion of a Wigley hull and a series 60 container ship at different Froude numbers. The results are compared with the results published in the literature. Conclusions based on the numerical simulation studies are given in Chapter 6.

Chapter 2

Cauchy Formula for Two-Dimensional Potential Flow

This chapter is concerned with the flow of a potential flow about a hydrofoil immersed beneath the free surface. The study of potential flow about a two-dimensional body has a history of more than a century. A linearized solution of a dipole moves with constant speed beneath the free surface presented by Havelock [13]. Since then, linear and nonlinear solutions for two-dimensional potential problems have been investigated by various researchers and many theories and methods to solve the problems have been developed using different levels of approximations. Detailed solutions for a point source, a point vortex and a dipole are given by Kochin *et al* [30], Wehausen and Laiton [72] and Lamb [34].

Nonlinear solutions of a two-dimensional free surface problem have been studied by many authors, for example; Campana *el al* [3], Chen and Hafezi [4] , Thiart and

Bertram [69]. The Cauchy's formula is also used to solve potential flow problems in the hydrodynamics field, by many authors such as Yükselen [78] , Schwarts [61] and Forbes [8–11]. The application of Cauchy's formula was mostly based on the traditional boundary element method and local shape function. Chuang [6] developed a desingularized procedure for Cauchy's formula where a global Gaussian quadrature technique was used to solve an interior potential problem.

In this chapter, the desingularized Cauchy's formulas for exterior infinite domain with and without free surface are derived and discretized with global Gaussian quadrature. For an infinite domain, the integral equations for disturbance potential, disturbance velocity and total potential are presented. To solve the free surface problem, two integral equations are obtained by setting the sources to be located either at the free surface or on the body surface.

2.1 Formulation of Desingularized Cauchy's Formula for an Infinite Domain

Consider a two-dimensional body in an infinite domain R, subject to a uniform flow U as shown in Figure 2.1. A complex analytic function $\mathcal{X}(z)$ in the domain R in terms of its boundary value can be expressed using Cauchy's formula.

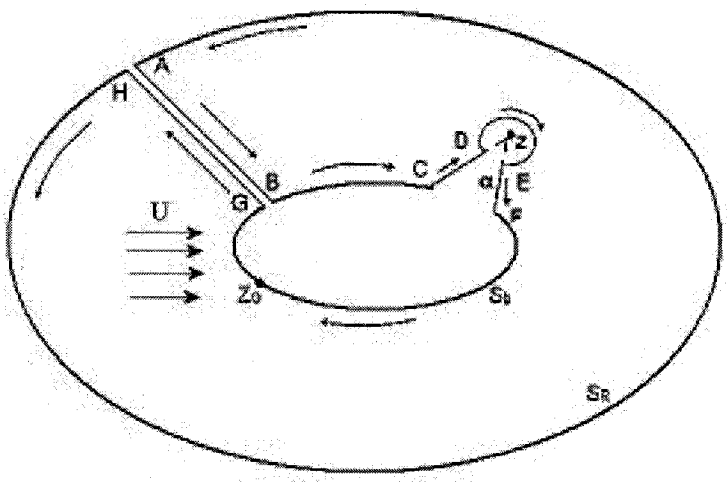

Figure 2.1: Domain R and Boundary S_b

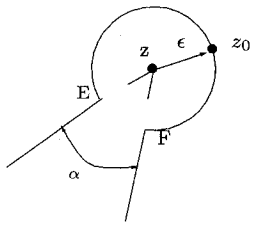

Figure 2.2: Semicircle with radius of ϵ

$$\int_{S_R} \frac{\mathcal{X}(z_0)}{z_0 - z}\, dz_0 + \int_{AB} \frac{\mathcal{X}(z_0)}{z_0 - z}\, dz_0 + \int_{BC} \frac{\mathcal{X}(z_0)}{z_0 - z}\, dz_0 + \int_{CD} \frac{\mathcal{X}(z_0)}{z_0 - z}\, dz_0$$
$$+ \int_{DE} \frac{\mathcal{X}(z_0)}{z_0 - z}\, dz_0 + \int_{EF} \frac{\mathcal{X}(z_0)}{z_0 - z}\, dz_0 + \int_{FG} \frac{\mathcal{X}(z_0)}{z_0 - z}\, dz_0 + \int_{GH} \frac{\mathcal{X}(z_0)}{z_0 - z}\, dz_0 = 0 \quad (2.1)$$

Let z be a field point inside the domain or on the body surface S_b and let z_0 be a source point in the contour as shown in Figure 2.1. For point z_0 on the contour DE of

a semi-circle with the radius of ϵ, we have

$$z_0 = z + \epsilon e^{\mathbf{i}\theta}, \qquad dz_0 = \mathbf{i}\epsilon e^{\mathbf{i}\theta} d\theta \qquad (0 \leq \theta \leq 2\pi) \tag{2.2}$$

and hence there follows

$$\int_{DE} \frac{\mathcal{X}(z_0)}{z_0 - z}\, dz_0 = \int_{2\pi-\alpha}^{0} \frac{\mathcal{X}(z + \epsilon e^{\mathbf{i}\theta})}{\epsilon e^{\mathbf{i}\theta}}\, \mathbf{i}\, d\theta \tag{2.3}$$

for all positive value of ϵ. Equation (2.3) must remain true in the limit as $\epsilon \to 0$, therefore Equation (2.3) is written as

$$\int_{DE} \frac{\mathcal{X}(z_0)}{z_0 - z}\, dz_0 = \mathbf{i}(\alpha - 2\pi)\mathcal{X}(z) \tag{2.4}$$

For point z on the body surface, the contours CD and EF are vanished from Equation (2.1) and the value of α is equal to π. Contours AB and GH have the same length but opposite direction, therefore their corresponding integrals are canceled out form Equation (2.1). For point z on S_R, we have $(z - z_0) \to \infty$ and the first integral in Equation (2.1) is equal to zero. Thus, for the exterior domain R , the Cauchy's formula is written as

$$2\pi\mathbf{i}\Big[\frac{k}{2\pi} - 1\Big]\mathcal{X}(z) = \int_{S_b} \frac{\mathcal{X}(z_0)}{z_0 - z}\, dz_0 \tag{2.5}$$

where

$$k = \begin{cases} 0 & \text{for} \quad z \in R \\ \alpha & \text{for} \quad z \in S_b \end{cases}$$

and α is the angle between two tangents to the contour S_b at the point z which is equal to π for continuous surface. Fundamental properties for Cauchy integrals and the singular integral with Cauchy type kernels are given by Muskhelishevili [45]. Based on the "subtracting and adding back" technique, the Cauchy's formula can be written in the following form

$$2\pi\mathbf{i}\Big[\frac{k}{2\pi} - 1\Big]\mathcal{X}(z) = \int_{S_b} \frac{\mathcal{X}(z_0) - \mathcal{X}(z)}{z_0 - z}\, dz_0 + \mathcal{X}(z) \int_{S_b} \frac{1}{z_0 - z}\, dz_0 \tag{2.6}$$

Now, using

$$\int_{S_b} \frac{1}{z_0 - z} dz_0 = k\,\mathbf{i} \qquad \text{for} \qquad z_0 \in S_b \tag{2.7}$$

Equation (2.6) reduces to Equation (2.8) which is valid at any point inside the domain R, on the smooth boundary S_b and even at the corner point on the boundary:

$$-2\pi\mathbf{i}\mathcal{X}(z) = \int_{S_b} \frac{\mathcal{X}(z_0) - \mathcal{X}(z)}{z_0 - z} dz_0 \qquad \text{for} \qquad z_0 \in S_b \tag{2.8}$$

On the boundary, we assume that the function $\mathcal{X}(z)$ satisfies the Hölder's condition so that the integrand in Equation (2.8) has a finite value when z_0 approaches z. Hence,

$$\lim_{z_0 \to z} \frac{\mathcal{X}(z_0) - \mathcal{X}(z)}{z_0 - z} = \left. \frac{d\mathcal{X}(z_0)}{dz_0} \right|_{z_0 = z} = \mathcal{X}'(z) \tag{2.9}$$

The integral in Equation (2.8) is a non singular integral and can be carried out using an arbitrary Gaussian quadrature with N Gaussian points.

Let field point z be located on the boundary S_b. The integral Equation (2.8) can be expressed in terms of the arc length of S as

$$-2\pi \mathbf{i} \mathcal{X}(z(s)) = \int_{S_b} \left\{ \frac{\mathcal{X}(z_0(s)) - \mathcal{X}(z(s))}{z_0(s) - z(s)} \right\} \frac{dz_0}{ds} ds \qquad \text{for} \qquad z, z_0 \in S_b \tag{2.10}$$

When z_0 approaches to z, the limit on the boundary can be written as

$$\lim_{z_0 \to z} \left\{ \frac{\mathcal{X}(z_0(s)) - \mathcal{X}(z(s))}{z_0(s) - z(s)} \right\} \frac{dz_0}{ds} = \frac{d\mathcal{X}}{dz_0} \frac{dz_0}{ds} = \frac{d\mathcal{X}}{ds} \tag{2.11}$$

To carry out the integral Equation (2.10), Gaussian quadrature with N Gaussian points is applied. Hence, the discretized form of Equation (2.10) can be written as a system of complex equations

$$-2\pi \mathbf{i} \mathcal{X}(z_i) = \sum_{j=1, j \neq i}^{N} \frac{\mathcal{X}(z_j) - \mathcal{X}(z_i)}{z_j - z_i} \left. \frac{dz_0}{ds} \right|_j \bar{w}_j + \left. \frac{d\mathcal{X}}{dz_0} \right|_i \left. \frac{dz_0}{ds} \right|_i \bar{w}_i \qquad i = 1, ..., N \tag{2.12}$$

If the values of the function $\mathcal{X}(z)$ is known on the boundary, then the function may be

easily and accurately computed at any point inside the domain.

2.1.1 Disturbance and Total Velocity Formulation

Let $\mathcal{X}(z)$ be the complex disturbance potential of a uniform flow past a body which is given in the z-plane in terms of the arc length as

$$\mathcal{X}(z(s)) = \phi_d(s) + \mathbf{i}\psi(s) \tag{2.13}$$

where $\phi_d(s)$ and $\psi(s)$ are the disturbance potential and stream function in terms of the arc length of S. The position vector of the point is written in terms of the arc length as

$$z(s) = x(s) + \mathbf{i}y(s) \tag{2.14}$$

where $x(s)$ and $y(s)$ are the coordinates of the point in x and y directions, respectively. The derivatives of Equations (2.13) and (2.14) with respect to the arc length are found to be

$$\begin{aligned} \frac{d\mathcal{X}}{ds} &= \frac{d\phi_d}{ds} + \mathbf{i}\frac{d\psi}{ds} = \phi_d' + \mathbf{i}\psi' \\ \frac{dz}{ds} &= \frac{dx}{ds} + \mathbf{i}\frac{dy}{ds} = x' + \mathbf{i}y' \end{aligned} \tag{2.15}$$

where the real and imaginary parts of dz/ds represent the components of the tangent vector $\vec{s}$ along the boundary curve S_b.

Substituting Equations (2.13), (2.14) and (2.15) into Equation (2.12) gives

$$\sum_{j=1,j\neq i}^{N}\left\{\frac{(\phi_{dj}-\phi_{di})+\mathbf{i}(\psi_j-\psi_i)}{(x_j-x_i)+\mathbf{i}(y_j-y_i)}\right\}(x'_j+\mathbf{i}y'_j)\bar{w}_j$$

$$+(\phi'_{di}+\mathbf{i}\psi'_i)\bar{w}_i=-2\pi\mathbf{i}\,(\phi_{di}+\mathbf{i}\psi_i)\qquad\text{for}\qquad i=1,\ldots,N \tag{2.16}$$

where subscriptions i and j are pointed to the field point z_i and source point z_j, respectively. Separating the real and the imaginary parts of Equations (2.16) through (2.18), one obtains the following matrix form:

$$\sum_{j=1}^{N}(A_{ij}\psi_j)=\sum_{j=1}^{N}(B_{ij}\phi_{dj})+\bar{w}_i\phi'_{di}\qquad\text{for}\qquad i=1,\ldots,N \tag{2.17}$$

$$\sum_{j=1}^{N}(A_{ij}\phi_{dj})=-\sum_{j=1}^{N}(B_{ij}\psi_j)-\bar{w}_i\psi'_i\qquad\text{for}\qquad i=1,\ldots,N \tag{2.18}$$

where

$$\begin{cases}A_{ij}=\frac{\vec{r}_{ij}\cdot\vec{n}_j}{|r_{ij}^2|}\bar{w}_j & j\neq i\\ A_{ii}=2\pi-\sum_{j=1,j\neq i}^{N}\frac{\vec{r}_{ij}\cdot\vec{n}_j}{|r_{ij}^2|}\bar{w}_j\end{cases}$$

$$\begin{cases}B_{ij}=\frac{\vec{r}_{ij}\cdot\vec{s}_j}{|r_{ij}^2|}\bar{w}_j & j\neq i\\ B_{ij}=-\sum_{j=1,j\neq i}^{N}\frac{\vec{r}_{ij}\cdot\vec{s}_j}{|r_{ij}^2|}\bar{w}_j\end{cases}$$

$\vec{r}_{ij}=(x_j-x_i)\,\vec{i}+(y_j-y_i)\,\vec{j}$ is the distance vector between the source point and the field

point. $\vec{n}_j$ and $\vec{s}_j$ are the unit normal and tangential vectors at point j, respectively.

To derive the formulation of the total velocity potential, the exterior incident flow potential ϕ_I can be extended into the interior region; then, the interior region becomes the domain [22]. Using the Cauchy's formula for interior domain [6] and adding the incident potential to the disturbance potential, Equations (2.17) and (2.18) reduce to a versatile form for total complex potential as shown in:

$$\sum_{j=1}^{N}(B_{ij}\overline{\Phi}_j) = -\bar{w}_i\overline{\Phi}'_i - 2\pi\psi_{Ii} \qquad \text{for} \qquad i = 1, \ldots, N \tag{2.19}$$

$$\sum_{j=1}^{N}(A_{ij}\overline{\Phi}_j) = 2\pi\phi_{Ii} \qquad \text{for} \qquad i = 1, \ldots, N \tag{2.20}$$

where $\overline{\Phi}_i = \phi_{di} + \phi_{Ii}$ is the total potential at the ith node , ϕ_{Ii} and ψ_{Ii} are the incident velocity potential and stream function at the ith node respectively.

2.1.2 Complex Velocity Formulation

If the complex disturbance velocity of a uniform flow past a body is given by $w(z) = \frac{d\chi}{dz}$ in the z-plane, the desingularized Cauchy integral equation for complex velocity can be written as

$$-2\pi \mathbf{i} w(z) = \int_{S_b} \frac{w(z_0) - w(z)}{z_0 - z}\, dz_0 \qquad z,\ z_0 \in S_b \tag{2.21}$$

Using the same procedure as for Equation 2.12, the discretized form of Equation (2.21) is obtained as

$$-2\pi \mathbf{i} w(z_i) = \sum_{j=1, j\neq i}^{N} \frac{w(z_j) - w(z_i)}{z_j - z_i} \frac{dz}{ds}\bigg|_j \bar{w}_j + \frac{dw}{dz}\bigg|_i \frac{dz}{ds}\bigg|_i \bar{w}_i \qquad i = 1, ..., N \tag{2.22}$$

Additionally, the complex velocity $w(z)$ may be expressed as

$$w(z) = \frac{d\mathcal{X}}{dz} = \frac{d\mathcal{X}/ds}{dz/ds} \tag{2.23}$$

Substituting Equation (2.15) into Equation (2.23) gives

$$\begin{aligned} w(z) &= \frac{\phi'_d + \mathbf{i}\psi'}{x' + \mathbf{i}y'} \cdot \frac{x' - \mathbf{i}y'}{x' - \mathbf{i}y'} \\ &= \frac{(\phi'_d + \mathbf{i}\psi') \cdot (x' - \mathbf{i}y')}{x'^2 + y'^2} \\ &= (\phi'_d x' + \psi' y') - \mathbf{i}(\phi'_d y' - \psi' x') \\ &= u(x, y) - \mathbf{i}v(x, y) \end{aligned} \tag{2.24}$$

and

$$\frac{dw}{ds} = \frac{du}{ds} - \mathbf{i}\frac{dv}{ds} = u' - \mathbf{i}v' \tag{2.25}$$

$u(s)$ and $v(s)$ are the x and y components of the velocity along the boundary S_b, respectively, and can be written

$$u(s) = \phi'_d x' + \psi' y' \qquad \textit{and} \qquad v(s) = \phi'_d y' - \psi' x' \tag{2.26}$$

We denote the unit tangential vector by $\vec{\mathbf{u}}$,

$$\vec{\mathbf{u}} = \frac{dx}{ds}\vec{i} + \frac{dy}{ds}\vec{j} \tag{2.27}$$

Since along the boundary curve $\vec{\mathbf{u}} \cdot \vec{n} = 0$, the unit normal vector is obtained to be

$$\vec{n} = \frac{dy}{ds}\vec{i} - \frac{dx}{ds}\vec{j} \tag{2.28}$$

Using Equation (2.26) and the boundary conditions; $\psi_i = -y_i$ and $\psi_i' = -\frac{dy_i}{ds}$, the kinematic boundary condition along the boundary S_b might be specified as

$$\begin{aligned} \vec{V}(s).\vec{n}(s) &= \left[u(s)\vec{i} + v(s)\vec{j}\right].\left[y'(s)\vec{i} - x'(s)\vec{j}\right] \\ &= u(s)y'(s) - v(s)x'(s) \\ &= (\phi_d' x' + \psi' y')y' - (\phi_d' y' - \psi' x')x' \\ &= \psi'(y'^2 + x'^2) = \psi' = -\frac{dy}{ds} \end{aligned} \tag{2.29}$$

Thus, the relation between velocity components along the boundary is obtained as:

$$v(s) = \frac{y'}{x'}(u(s) + 1) \tag{2.30}$$

$$v' = u\left[\frac{x'y'' - x''y'}{x'^2}\right] + u'\frac{y'}{x'} + \frac{x'y'' - x''y'}{x'^2} \tag{2.31}$$

Substituting Equations (2.23) and (2.25) into Equation (2.22) gives

$$\sum_{j=1,j\neq i}^{N}\left\{\frac{(u_j-u_i)-\mathbf{i}(v_j-v_i)}{(x_j-x_i)+\mathbf{i}(y_j-y_i)}\right\}(x'_j+\mathbf{i}y'_j)\bar{w}_j$$

$$+(u'_i-\mathbf{i}v'_i)\bar{w}_i=-2\pi\mathbf{i}\,(u_i-\mathbf{i}v_i)\qquad\text{for}\qquad i=1,\ldots,N \tag{2.32}$$

Separating the real part and imaginary part of Equation (2.32), two sets of real equations are obtained

$$-\sum_{j=1}^{N}(A_{ij}v_j)=\sum_{j=1}^{N}(B_{ij}u_j)+\bar{w}_iu'_i\qquad\text{for}\qquad i=1,\ldots,N \tag{2.33}$$

$$\sum_{j=1}^{N}(A_{ij}u_j)=\sum_{j=1}^{N}(B_{ij}v_j)+\bar{w}_iv'_i\qquad\text{for}\qquad i=1,\ldots,N \tag{2.34}$$

Substituting v and v' from Equations (2.30) and (2.31) into Equations (2.33) and (2.34), $2N$ equations with $2N$ unknowns, namely, u_j and u'_j are obtained

$$[C_{ij}]\{u_j\}=D_i+\bar{w}_iu'_i\qquad\text{for}\qquad i=1,\ldots,N \tag{2.35}$$

$$[E_{ij}]\{u_j\}=F_i+G_i\bar{w}_iu'_i\qquad\text{for}\qquad i=1,\ldots,N \tag{2.36}$$

where

$$C_{ij}=-A_{ij}\frac{y'_j}{x'_j}-B_{ij}\qquad\text{and}\qquad D_i=A_{ij}\frac{y'_j}{x'_j}$$

$$E_{ij} = \begin{cases} A_{ij} - B_{ij}\frac{y'_j}{x'_j} & j \neq i \\ A_{ij} - B_{ij}\frac{y'_j}{x'_j} - \bar{w}_i\left[\frac{x'_i y''_i - x''_i y'_i}{x'^2_i}\right] & j = i \end{cases}$$

$$F_i = B_{ij}\frac{y'_j}{x'_j} + \bar{w}_i\left[\frac{x'_i y''_i - x''_i y'_i}{x'^2_i}\right] \quad \text{and} \quad G_i = \frac{y'_i}{x'_i}$$

A_{ij} and B_{ij} are the same as in Equations (2.17) and (2.18).

2.1.3 Implementation of Kutta Condition

In order to implement the Kutta condition, the hydrofoil is split into upper and lower parts as shown in Figure 2.3. The Cauchy's formula, Equation (2.8), for the field point

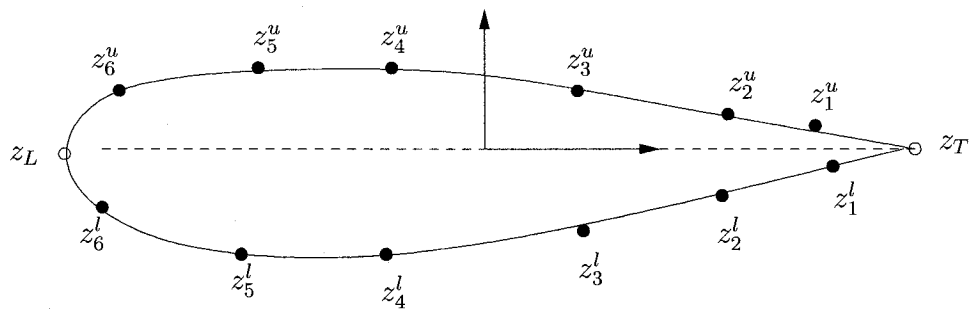

Figure 2.3: Points on the upper and lower part of an airfoil

located on the upper part of the body can be written as

$$-2\pi \mathbf{i}\mathcal{X}(z^u) = \int_{z_T}^{z_L} \frac{\mathcal{X}(z^u_0) - \mathcal{X}(z^u)}{z^u_0 - z^u} dz^u_0 + \int_{z_L}^{z_T} \frac{\mathcal{X}(z^l_0) - \mathcal{X}(z^u)}{z^l_0 - z^u} dz^l_0 \tag{2.37}$$

adding and subtracting an integral of the lower part to the integral equation, the following integral is obtained

$$\begin{aligned}
-2\pi \mathrm{i}\mathcal{X}(z^u) &= \int_{z_T}^{z_L} \frac{\mathcal{X}(z_0^u)-\mathcal{X}(z^u)}{z_0^u-z^u}dz_0^u + \int_{z_L}^{z_T} \frac{\mathcal{X}(z_0^l)-\mathcal{X}(z^u)}{z_0^l-z^u}dz_0^l \\
&\quad + \int_{z_L}^{z_T} \frac{\mathcal{X}(z_0^l)-\mathcal{X}(z^l)}{z_0^l-z^u}dz_0^u - \int_{z_L}^{z_T} \frac{\mathcal{X}(z_0^l)-\mathcal{X}(z^l)}{z_0^l-z^u}dz_0^l \\
&= \int_{z_T}^{z_L} \frac{\mathcal{X}(z_0^u)-\mathcal{X}(z^u)}{z_0^u-z^u}dz_0^u + \int_{z_L}^{z_T} \frac{\mathcal{X}(z_0^l)-\mathcal{X}(z^l)}{z_0^l-z^u}dz_0^l \\
&\quad + \Big\{\mathcal{X}(z^l)-\mathcal{X}(z^u)\Big\}\int_{z_L}^{z_T} \frac{dz_0^l}{z_0^l-z^u} \\
&= \int_{z_T}^{z_L} \frac{\mathcal{X}(z_0^u)-\mathcal{X}(z^u)}{z_0^u-z^u}dz_0^u + \int_{z_L}^{z_T} \frac{\mathcal{X}(z_0^l)-\mathcal{X}(z^l)}{z_0^l-z^u}dz_0^l \\
&\quad + \Big\{\mathcal{X}(z^l)-\mathcal{X}(z^u)\Big\}\log\frac{z_T-z^u}{z_L-z^u}
\end{aligned} \tag{2.38}$$

Similarly, the integral equation for the field point located at the lower part of the body is written as

$$\begin{aligned}
-2\pi \mathrm{i}\mathcal{X}(z^l) &= \int_{z_L}^{z_T} \frac{\mathcal{X}(z_0^u)-\mathcal{X}(z^u)}{z_0^u-z^l}dz_0^u + \int_{z_T}^{z_L} \frac{\mathcal{X}(z_0^l)-\mathcal{X}(z^l)}{z_0^l-z^l}dz_0^l \\
&\quad + \Big\{\mathcal{X}(z_0^u)-\mathcal{X}(z^l)\Big\}\log\frac{z_L-z^l}{z_T-z^l}
\end{aligned} \tag{2.39}$$

Two system of equations are obtained from Equations (2.38) and (2.39) which can be written in matrix form as

$$[A_{ij}]\Big\{\psi_j\Big\} = [B_{ij}]\Big\{\phi_j\Big\} + \Big\{\bar{w}_i\phi_i'\Big\} \qquad i\,,j = 1,2,...,N,N+1,...,2N \tag{2.40}$$

and

$$[A_{ij}]\left\{\phi_j\right\} = -[B_{ij}]\left\{\psi_j\right\} + \left\{\bar{w}_i\psi_i'\right\} \qquad i\,,j = 1,2,...,N,N+1,...,2N \tag{2.41}$$

Here, N is the number of points in upper or lower part of the body and

$$\begin{cases} A_{ij} = \frac{\vec{r}_{ij}\cdot\vec{n}_j}{|r_{ij}^2|}\bar{w}_j & j \neq i \\ A_{ii} = 2\pi - \sum_{j=1,j\neq i}^{N} \frac{\vec{r}_{ij}\cdot\vec{n}_j}{|r_{ij}^2|}\bar{w}_j + a_i \end{cases}$$

$$\begin{cases} B_{ij} = \frac{\vec{r}_{ij}\cdot\vec{s}_j}{|r_{ij}^2|}\bar{w}_j & j \neq i \\ B_{ii} = -\sum_{j=1,j\neq i}^{N} \frac{\vec{r}_{ij}\cdot\vec{s}_j}{|r_{ij}^2|}\bar{w}_j + b_i \end{cases}$$

where

$$\begin{aligned} a_i &= \tan^{-1}\frac{y_T - y_i}{x_T - x_i} - \tan^{-1}\frac{y_L - y_i}{x_L - x_i} \qquad \text{for} \quad i = 1,...,N \\ a_i &= -\tan^{-1}\frac{y_T - y_i}{x_T - x_i} + \tan^{-1}\frac{y_L - y_i}{x_L - x_i} \qquad \text{for} \quad i = N+1,...,2N \\ b_i &= \frac{1}{2}\log\frac{(x_T - x_i)^2 + (y_T - y_i)^2}{(x_L - x_i)^2 + (y_L - y_i)^2} \qquad \text{for} \quad i = 1,...,N \\ b_i &= \frac{1}{2}\log\frac{(x_L - x_i)^2 + (y_L - y_i)^2}{(x_T - x_i)^2 + (y_T - y_i)^2} \qquad \text{for} \quad i = N+1,...,2N \end{aligned} \tag{2.42}$$

Following Choi and Kinnas [5], a vortex with unknown strength is added to the trailing edge, which induces the potential at the collocation points. This potential is written

as

$$\phi_i^{\Gamma} = \tan^{-1} \frac{y_i - y_T}{x_i - x_T} \tag{2.43}$$

The circulation around the body can be approximated as $\Phi_1 - \Phi_{2N}$ assuming that the first and the last collocation points are close to the trailing edge. Then, the integral equation for total potential is written as

$$[A_{ij}]\left\{\Phi_j\right\} = -[B_{ij}]\left\{\psi_j\right\} + \left\{\bar{w}_i \psi_i'\right\} \qquad i\,, j = 1, 2, ..., N, N+1, ..., 2N \tag{2.44}$$

where coefficient matrices A_{ij} and B_{ij} are the same as for Equation (2.41) except that ϕ_j^{Γ} is added to A_{ij} for $i = 1, ..., 2N$, $j = 1$ and $-\phi_j^{\Gamma}$ is added to A_{ij} for $i = 1, ..., 2N$, $j = 2N$. By assuming a initial value for vortex strength, the total potential on the collocation points can be obtained. The pressure coefficient at the collocation points is computed form [15]

$$C_p = 1 - \left(\frac{V_t}{U}\right)^2 \tag{2.45}$$

where V_t is the total velocity. The differences of the pressure coefficients below and above the trailing edge is written

$$\Delta C_p = C_{p_1} - C_{p_{2N}} \tag{2.46}$$

By small increment on the strength of vortex and using the iteration method, the convergent solution can be obtained in the following form:

$$\Gamma^{(n+1)} = \Gamma^{(n)} - \frac{\epsilon \Delta C_p^(n)}{\Delta C_p^(n) - \Delta C_p^(n+1)} \tag{2.47}$$

where ϵ is the increment of the vortex strength on each iteration.

2.2 Formulation of Desingularized Cauchy's Formula for Free Surface

Consider a fluid of infinite depth flowing with a speed U from left to right. An airfoil is placed with the origin located on the distance H beneath the free surface. The Froude number based on the submergence depth is defined as $F_n = U/\sqrt{gH}$, where g is the acceleration due to gravity. Assuming that the fluid is ideal and the flow is irrotational, the velocity potential ϕ satisfies following conditions:

• Laplace's equation

$$\nabla^2 \phi = 0 \qquad \text{in the fluid domain.} \tag{2.48}$$

•Body boundary condition

$$\frac{\partial \phi}{\partial n} = \vec{U} \cdot \vec{n} \qquad \text{on} \quad S_b \tag{2.49}$$

• Far upstream, the fluid velocity satisfies the radiation condition

$$\frac{\partial \phi}{\partial x} \to 1, \quad \text{and} \quad \frac{\partial \phi}{\partial y} \to 0 \quad \text{as} \quad x \to -\infty \tag{2.50}$$

• On the free surface the kinematic and Bernoulli equations are imposed

$$\frac{1}{2}F_n^2(u^2+v^2)+y = \frac{1}{2}F_n^2 \quad \text{and} \quad u\eta'(x) = v \quad \text{on} \quad y = \eta(x) \tag{2.51}$$

where u and v are the components of velocity in x and y directions, respectively, and η is the wave elevation. Two different integral equations can be obtained by assuming the sources on the free surface and on the body surface. Suppose that a fixed point at

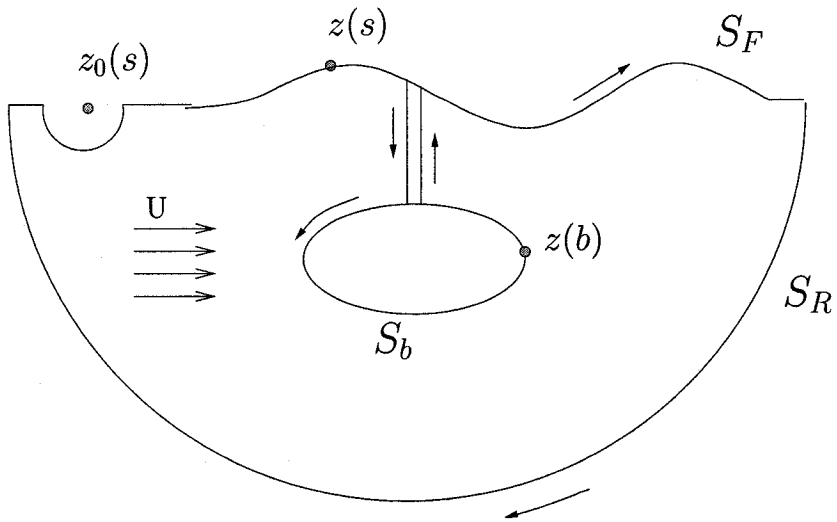

Figure 2.4: Source point at the free surface

the free surface is $z_0(s)$ and the moving point is $z(s)$, and the integral over the body is taken counterclockwise as shown in Figure 2.4. The Cauchy's integral formula can be

written as:

$$\pi i\, f(z(s)) = -\int_{S_F+S_R} \left\{ \frac{f(z_0(s))}{z_0(s)-z(s)} \right\} \frac{dz_0}{ds} ds - \int_{S_b} \left\{ \frac{f(z(b))}{z(b)-z(s)} \right\} \frac{dz_b}{ds} ds$$
$$\text{for} \qquad z, z_0 \in (S_F + S_R), z_b \in S_b \tag{2.52}$$

where

$$f(z) = \frac{d\chi(z)}{dz} - 1$$
$$f(z)_{z\to\infty} = u - iv - 1 = 0 \tag{2.53}$$

Here, the analytic function $\chi(z) = \phi + i\psi$ and $z = x + iy$. Using the "subtracting and adding back" technique for outer boundary Equation (2.52) can be written as:

$$\begin{aligned} \pi i\, f(z(s)) \;=\; & \int_{S_F+S_R} \left\{ \frac{f(z_0(s)) - f(z(s))}{z_0(s)-z(s)} \right\} \frac{dz_0}{ds} ds \\ & + f(z(s)) \int_{S_F+S_R} \left\{ \frac{1}{z_0(s)-z(s)} \right\} \frac{dz_0}{ds} ds \\ & - \int_{S_b} \left\{ \frac{f(z(b))}{z(b)-z(s)} \right\} \frac{dz_b}{ds} ds \end{aligned}$$
$$\text{for} \qquad z, z_0 \in (S_F + S_R), z_b \in S_b \tag{2.54}$$

since

$$\int_{S_F+S_R} \left\{ \frac{1}{z_0(s)-z(s)} \right\} \frac{dz_0}{ds} ds = \pi i \quad \text{for} \quad z, z_0 \in (S_F + S_R) \tag{2.55}$$

Equation (2.54) can be written:

$$-\int_{S_F+S_R}\left\{\frac{f(z_0(s))-f(z(s))}{z_0(s)-z(s)}\right\}\frac{dz_0}{ds}ds-\int_{S_b}\left\{\frac{f(z(b))}{z(b)-z(s)}\right\}\frac{dz_b}{ds}ds=2\pi i f(z(s))$$
$$\text{for} \qquad z, z_0 \in (S_F+S_R), z_b \in S_b \tag{2.56}$$

Equation (2.56) for the source point z(s) located at the free surface can be written as follows:

$$-\int_{S_F}\left\{\frac{f(z_0(s))-f(z(s))}{z_0(s)-z(s)}\right\}\frac{dz_0}{ds}ds-\int_{S_R}\left\{\frac{f(z_0(s))-f(z(s))}{z_0(s)-z(s)}\right\}\frac{dz_0}{ds}ds$$
$$-\int_{S_b}\left\{\frac{f(z(b))}{z(b)-z(s)}\right\}\frac{dz_b}{ds}ds=2\pi i f(z(s))$$
$$\text{for} \quad z(s)\in S_F, z_0(s)\in (S_F+S_R), z_b\in S_b \tag{2.57}$$

from Equation (2.53)

$$f(z_0(s))_{S_R\to\infty}=0$$

therefore Equation (2.57) becomes

$$-\int_{S_F}\left\{\frac{f(z_0(s))-f(z(s))}{z_0(s)-z(s)}\right\}\frac{dz_0}{ds}ds-\int_{S_b}\left\{\frac{f(z(b))}{z(b)-z(s)}\right\}\frac{dz_b}{ds}ds=2\pi i f(z(s))$$
$$\text{for} \quad z(s), z_0(s)\in S_F, z_b\in S_b \tag{2.58}$$

Discretizing the integral Equation (2.58) and separating it into two real equations, the real part of Equation (2.58) is obtained as:

$$\sum_{j=1,j\neq i}^{N}\left\{\frac{\phi_j'(x_j-x_i)-\phi_i'(x_j-x_i)\vec{s}_i\vec{s}_j-\phi_i'(y_j-y_i)\vec{s}_i\vec{n}_j}{|r_{ij}^2|}\right\}\bar{w}_j$$
$$+\phi_i''x_i'\bar{w}_i-\phi_i'\left\{x_i''(x_i'^2-y_i'^2)+2x_i'y_i'y_i''\right\}\bar{w}_i$$
$$+\sum_{m=1}^{M}\left\{\frac{\phi_m'(x_m-x_i)-\vec{r}_{im}\vec{s}_m}{|r_{im}^2|}\right\}w_m=2\pi\phi_j'y_j' \qquad \text{for} \qquad i=1,\ldots,N \quad (2.59)$$

and the imaginary part is obtained

$$-\sum_{j=1,j\neq i}^{N}\left\{\frac{\phi_j'(y_j-y_i)+\phi_i'(x_j-x_i)\vec{s}_i\vec{n}_j-\phi_i'(y_j-y_i)\vec{s}_i\vec{s}_j}{|r_{ij}^2|}\right\}\bar{w}_j$$
$$-\phi_i''y_i'\bar{w}_i-\phi_i'\left\{y_i''(x_i'^2-y_i'^2)-2x_i'y_i'y_i''\right\}\bar{w}_i$$
$$-\sum_{m=1}^{M}\left\{\frac{\phi_m'(y_m-y_i)+\vec{r}_{im}\vec{n}_m}{|r_{im}^2|}\right\}w_m=2\pi\phi_j'x_j'-2\pi \qquad \text{for} \qquad i=1,\ldots,N \quad (2.60)$$

Here, M and N are the numbers of collocation points on the body surface and the free surface, respectively. The terms ϕ' and ϕ'' represent the first and second derivatives of ϕ with respect to arc length s.

Multiplying the real part by y_i' and the imaginary part by x_i' and adding two equations yields

$$\sum_{j=1,j\neq i}^{N}\left\{\frac{-\phi'_j\vec{r}_{ij}\vec{n}_i+\phi'_i\vec{r}_{ij}\vec{n}_j}{|r^2_{ij}|}\right\}\bar{w}_j+\phi'_i(x'_iy''_i-x''_iy'_i)\bar{w}_i+$$
$$+\sum_{m=1}^{M}\left\{\frac{-\phi'_m\vec{r}_{im}\vec{n}_i}{|r^2_{im}|}\right\}w_m+\sum_{m=1}^{M}\left\{\frac{(x'_i\vec{r}_{im}\vec{n}_m+y'_i\vec{r}_{im}\vec{s}_m)}{|r^2_{im}|}\right\}w_m-2\pi\phi'_j+2\pi x'_j=0$$
$$\text{for}\qquad i=1,\ldots,N \tag{2.61}$$

Equation (2.61) can be written in a matrix form as

$$[A_{ij}]\left\{\phi'_j\right\}+[B_{im}]\left\{\phi'_m\right\}+[C_{im}]\left\{w_m\right\}+[D_{ij}]\left\{\bar{w}_j\right\}=0 \tag{2.62}$$

here

$$A_{ij}=\frac{-\vec{r}_{ij}\vec{n}_i}{|r^2_{ij}|}\bar{w}_j\qquad\qquad i\neq j$$
$$A_{ii}=-2\pi+(x'_iy''_i-x''_iy'_i)\bar{w}_i+\sum_{j=1,j\neq i}^{N}\frac{\vec{r}_{ij}\vec{n}_j}{|r^2_{ij}|}\bar{w}_j$$
$$B_{im}=\frac{-\vec{r}_{im}\vec{n}_i}{|r^2_{im}|}w_m$$
$$C_{im}=\frac{x'_i\vec{r}_{im}\vec{n}_m+y'_i\vec{r}_{im}\vec{s}_m}{|r^2_{im}|}$$
$$D_{ij}=2\pi\frac{x'_i}{\bar{w}_j}$$
$$\vec{r}_{ij}=(x_j-x_i)\vec{i}+(y_j-y_i)\vec{j}$$
$$\vec{n}_i=y'_i\vec{i}-x'_i\vec{j},\qquad\qquad \vec{s}_i=x'_i\vec{i}+y'_i\vec{j} \tag{2.63}$$

2.2.1 Source Point on the Body Surface

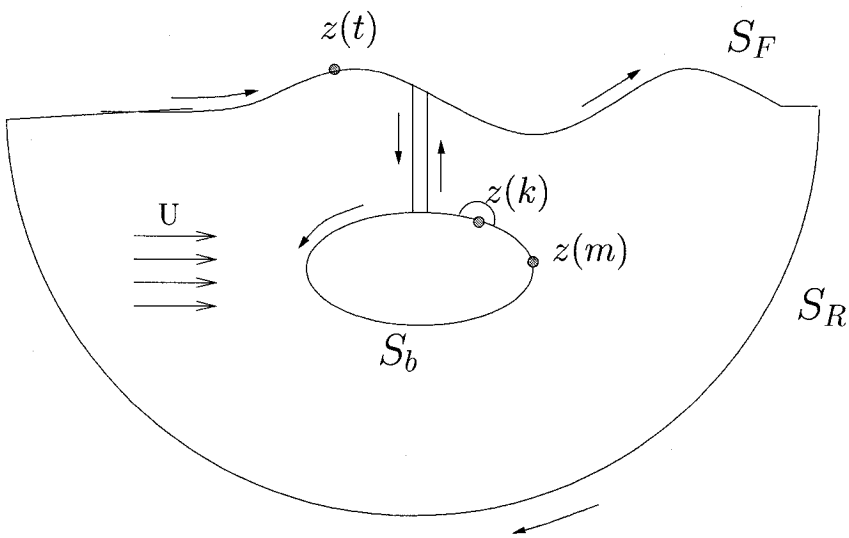

Figure 2.5: Source point on the body surface

Now, suppose that a fixed point on the body is $z(k)$ and the moving point is $z(m)$, and the integral over the body is taken counterclockwise. The Cauchy's integral formula can be written as:

$$\pi i f(z(k)) = -\int_{S_F+S_R} \left\{ \frac{f(z(t))}{z(t)-z(k)} \right\} \frac{dz(t)}{ds} ds - \int_{S_b} \left\{ \frac{f(z(m))}{z(m)-z(k)} \right\} \frac{dz_m}{ds} ds$$
$$\text{for} \qquad z(t) \in (S_F + S_R), z(k), z(m) \in S_b \quad (2.64)$$

Applying the "subtracting and adding back" technique and some manipulation, Equation (2.64) can be written in the following form

$$2\pi i f(z(k)) = -\int_{-\infty}^{\infty} \left\{ \frac{f(z(t))}{z(t)-z(k)} \right\} \frac{dz(t)}{ds} ds - \int_{S_b} \left\{ \frac{f(z(m))-f(z(k))}{z(m)-z(k)} \right\} \frac{dz_m}{ds} ds$$
$$\text{for} \quad z(t) \in (S_F) \quad \textit{and} \quad z(k), z(m) \in S_b \qquad (2.65)$$

The real part of Equation (2.65) is:

$$
\begin{aligned}
&-\sum_{j=1}^{N}\left\{\frac{\phi'_j(x_j-x_k)-\vec{r}_{kj}\vec{s}_j)}{|r_{kj}^2|}\right\}\bar{w}_j \\
&-\sum_{m=1,m\neq k}^{M}\left\{\frac{\phi'_m(x_m-x_k)-\phi'_k(x_m-x_k)\vec{s}_k\vec{s}_m-\phi'_k(y_m-y_k)\vec{s}_k\vec{n}_m}{|r_{kj}^2|}\right\}w_m \\
&-\phi''_k x'_k w_k+\phi'_k\left\{x''_k({x'_k}^2-{y'_k}^2)+2x'_k y'_k y''_k\right\}w_k=2\pi\phi'_k y'_k \\
&\qquad\qquad \text{for} \qquad k=1,\ldots,M
\end{aligned}
\tag{2.66}
$$

and the imaginary part of Equation (2.65) is

$$
\begin{aligned}
&\sum_{j=1}^{N}\left\{\frac{\phi'_j(y_j-y_k)+\vec{r}_{kj}\vec{n}_j}{|r_{kj}^2|}\right\}\bar{w}_j \\
&+\sum_{m=1,m\neq k}^{M}\left\{\frac{\phi'_m(y_m-yk)+\phi'_k(x_m-x_k)\vec{s}_k\vec{n}_m-\phi'_k(y_m-y_k)\vec{s}_k\vec{s}_m}{|r_{km}^2|}\right\}w_m \\
&+\phi''_k y'_k w_k+\phi'_k\left\{y''_k({x'_k}^2-{y'_k}^2)-2x'_k y'_k y''_k\right\}w_k=2\pi(\phi'_k x'_k-1) \\
&\qquad\qquad \text{for} \qquad i=1,\ldots,N
\end{aligned}
\tag{2.67}
$$

Multiplying the real part by y'_k and the imaginary part by x'_k and adding two equations yield

$$
\begin{aligned}
&\sum_{j=1}^{N}\left\{\frac{-\phi'_j\vec{r}_{kj}\vec{n}_k}{|r_{kj}^2|}\right\}\bar{w}_j+\sum_{j=1}^{N}\left\{\frac{y'_k\vec{r}_{kj}\vec{s}_j+x'_k\vec{r}_{kj}\vec{n}_j}{|r_{kj}^2|}\right\}\bar{w}_j+ \\
&\sum_{m=1\neq k}^{M}\left\{\frac{-\phi'_m\vec{r}_{km}\vec{n}_k+\phi'_k\vec{r}_{km}\vec{n}_m}{|r_{km}^2|}\right\}w_m+ \\
&+\phi'_k(y''_k x'_k-y'_k x''_k)-2\pi\phi'_k+2\pi x'_k=0 \qquad \text{for} \qquad k=1,\ldots,M
\end{aligned}
\tag{2.68}
$$

again, M and N are the numbers of collocation points on the body surface and the free surface, respectively. Above equation can be written in a matrix form

$$[A^*_{kj}]\left\{\phi'_j\right\} + [B^*_{km}]\left\{\phi'_m\right\} + [C^*_{kj}]\left\{\bar{w}_j\right\} + [D^*_{km}]\left\{w_m\right\} = 0 \tag{2.69}$$

where

$$\begin{aligned}
A^*_{kj} &= \frac{-\vec{r}_{kj}\vec{n}_k}{|r^2_{kj}|}w_m \\
B^*_{km} &= \frac{-\vec{r}_{km}\vec{n}_k}{|r^2_{km}|}w_m \qquad\qquad k \neq m \\
B^*_{kk} &= -2\pi + (y''_k x'_k - y'_k x''_k)w_k + \sum_{m=1\neq k}^{M} \vec{r}_{km}\vec{n}_m \\
C^*_{kj} &= \frac{y'_k \vec{r}_{kj}\vec{s}_j + x'_k \vec{r}_{kj}\vec{n}_j}{|r^2_{kj|}} \\
D^*_{km} &= \frac{2\pi x'_k}{w_k}w_m
\end{aligned} \tag{2.70}$$

Matrix system (2.62) gives N equations for N points at the free surface with $N + M$ unknowns. Matrix (2.69) also gives M equations for M points on the body surface with the same $N + M$ unknowns. By combining of these two system of equations a $(N + M) \times (N + M)$ system of equations with $N + M$ unknowns can be obtained

$$\begin{pmatrix} A_{ij} & B_{im} \\ A^*_{kj} & B^*_{km} \end{pmatrix} \begin{pmatrix} \phi'_j \\ \phi'_m \end{pmatrix} + \begin{pmatrix} D_{ij} & C_{im} \\ C^*_{kj} & D^*_{km} \end{pmatrix} \begin{pmatrix} \bar{w}_j \\ w_m \end{pmatrix} = 0 \tag{2.71}$$

Chapter 3

Two-Dimensional Numerical Results

The discretized form of the desingularized Cauchy formula is solved and simulated for two kinds of body geometry. The one is an elliptical cylinder and the other, Joukowski airfoil. The discussion of simulation results are followed in next sections.

3.1 Uniform Flow Past an Elliptical Cylinder

The boundary of the elliptical cylinder is computed from a conformal mapping given by [44]

$$\zeta(\theta) = e^{\mathrm{i}\theta} + \frac{c}{e^{\mathrm{i}\theta}} \qquad 0 \leq \theta < 2\pi \tag{3.1}$$

and the complex potential $\Omega(\zeta(\theta))$ on the body of the elliptical cylinder is given by

$$\Omega(\zeta(\theta)) = U\Big\{\zeta(\theta) + \frac{1}{\zeta(\theta)}\Big\} \tag{3.2}$$

In the computational procedure, the Gaussian points are used as the collocation points, and the corresponding parameter θ of the collocation points are computed using the Newton Raphson iteration technique.

$$\theta_j^{(n+1)} = \theta_j^{(n)} - \frac{\Omega(\theta_j^{(n)})}{\Omega'(\theta_j^{(n)})} \tag{3.3}$$

where (n) and $(n+1)$ denotes the nth and the $(n+1)$th iterations respectively.

The boundary conditions which are $\psi_j = -y_j$ and $\psi'_j = -\left[\frac{dy}{ds}\right]_j$ are imposed at the collocation points. The complex disturbance velocity, w_j, at collocation point s_j, for $j = 1, 2, ...N$ can be written as

$$w_j = u_j - \mathbf{i}v_j = \frac{d\Omega}{dz}\Big|_j = \frac{\phi'_j + \mathbf{i}\psi'_j}{x'_j + \mathbf{i}y'_j} \tag{3.4}$$

and the pressure coefficient $C_p^{(j)}$ at collocation point s_j, for $j = 1 \ldots, N$ is [15]:

$$C_p^{(j)} = 1 - \frac{[u_j^2 + v_j^2]}{U^2} \tag{3.5}$$

where U is the velocity of the uniform flow.

Based on this procedure, five different elliptical cylinders are chosen, corresponding to $c = 0$, $c = 0.3$, 0.5, 0.7 and $c = 0.99$. Each elliptical cylinder has the major semi-axis and the minor semi-axis of $1+c$ and $1-c$, respectively. Moreover, the boundary of each elliptical cylinder is divided into four equal parts on which 4, 8, 12, 16 and 30-points Gaussian quadratures are applied. In addition, the root mean square error for pressure

for pressure coefficient, RMS, are calculated as follows;

$$\text{RMS} = \sqrt{\frac{1}{N}\sum_{j=1}^{N}\left\{\frac{C_{panalytic}^{(j)} - C_{pnum}^{(j)}}{C_{panalytic}^{(j)}}\right\}^2} \tag{3.6}$$

where, the pressure coefficient, $C_{p_{analytic}}$, at the Gaussian points is computed based on the above procedure and $C_{p_{num}}$ is computed using proposed complex potential formulation and complex velocity formulation. N is the number of Gaussian points in the entire length of the body surface. Figure 3.1 shows the distribution of pressure coefficient on the surface of an ellipse with varying c. The pressure coefficients for a circle which is an ellipse with equal semi-axis ($c = 0$), and for a very thin ellipse ($c = 0.99$) are shown in Figures 3.2 and 3.3, respectively. Figure 3.4 shows the results of simulations carried out for ellipses with major semi-axis in y direction and minor semi-axis in x direction. They indicate that even with a few number of Gaussian points, the results obtained from the proposed methods are very accurate when the ellipse is not very thin. For a thin ellipse ($c > 0.95$), the differences between numerical and analytical results are noticeable. Root mean square error of pressure coefficient is depicted in Figure 3.5. It is indicated that the velocity formulation gives more accurate results than the potential formulation. However, these results show that increasing the number of collocation points beyond a certain threshold does not significantly improve the accuracy of computation. Figure 3.5 also shows that the RMS error of pressure coefficients increase by increasing the value of c for an elliptical cylinder.

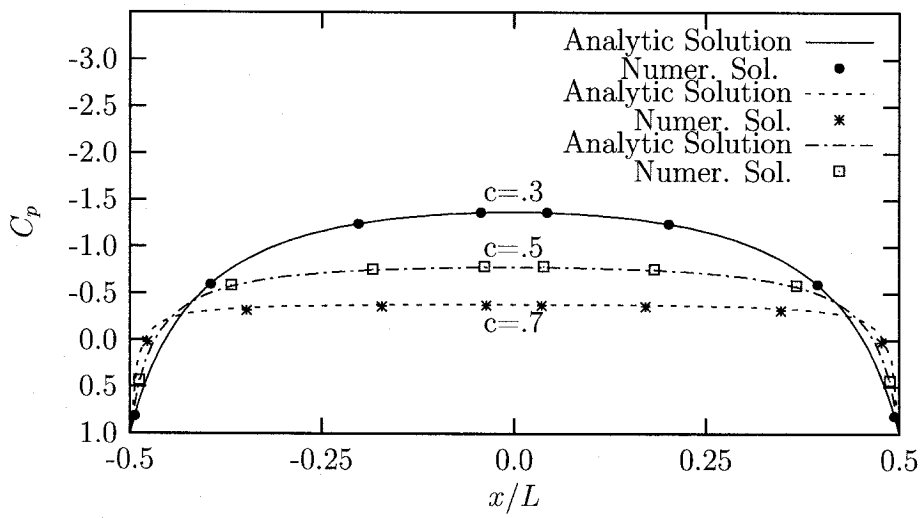

Figure 3.1: Pressure coefficient vs. non-dimensional length, x/L, for ellipse with different c.

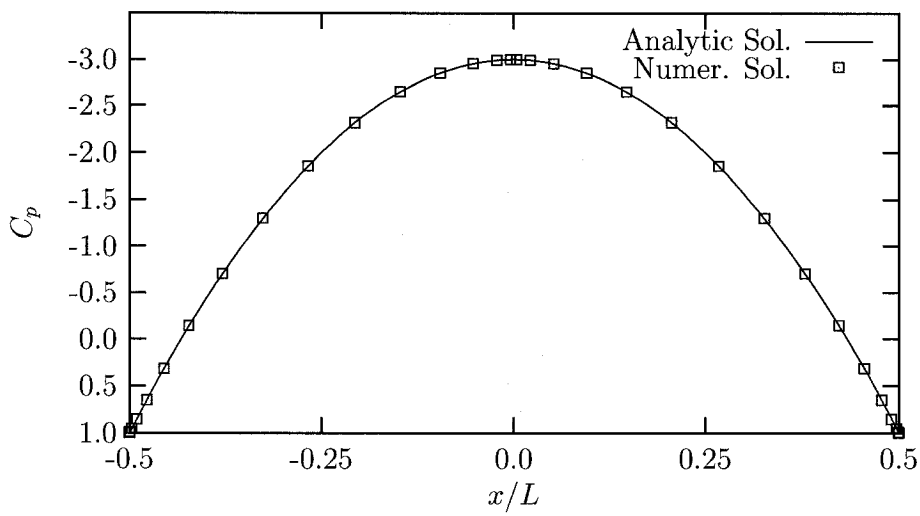

Figure 3.2: Pressure coefficient vs. non-dimensional length, x/L, for a circle ($c = 0$).

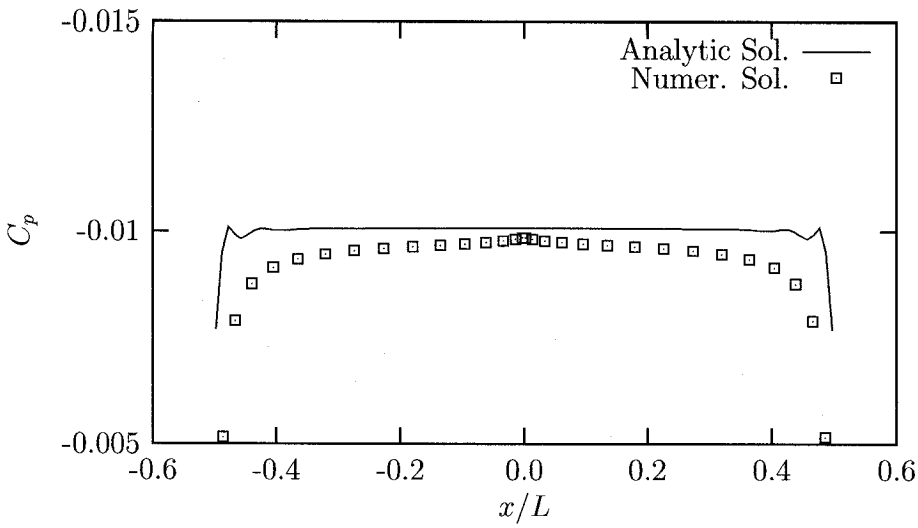

Figure 3.3: Pressure coefficient vs. non-dimensional length, x/L, for a thin ellipse ($c = 0.99$).

3.2 Uniform Flow Past a Joukowski Airfoil

The mapping function which maps a unit circle to a Joukowski airfoil is given by [44]

$$\zeta(\theta) = e^{\mathrm{i}\theta} + \sqrt{c} - e^{\mathrm{i}\beta} + \frac{c}{e^{\mathrm{i}\theta} + \sqrt{c} - e^{\mathrm{i}\beta}} \tag{3.7}$$

where $\beta = 0$ is the angle of attack.

The complex potential on the boundary of the airfoil and the computational procedure in this example is the same as that of the elliptical cylinder in the previous section.

In the numerical simulation, three different Joukowski airfoils are computed, corresponding to $c = 0.3$, 0.5 and 0.7. The total arc length of the airfoil is divided into

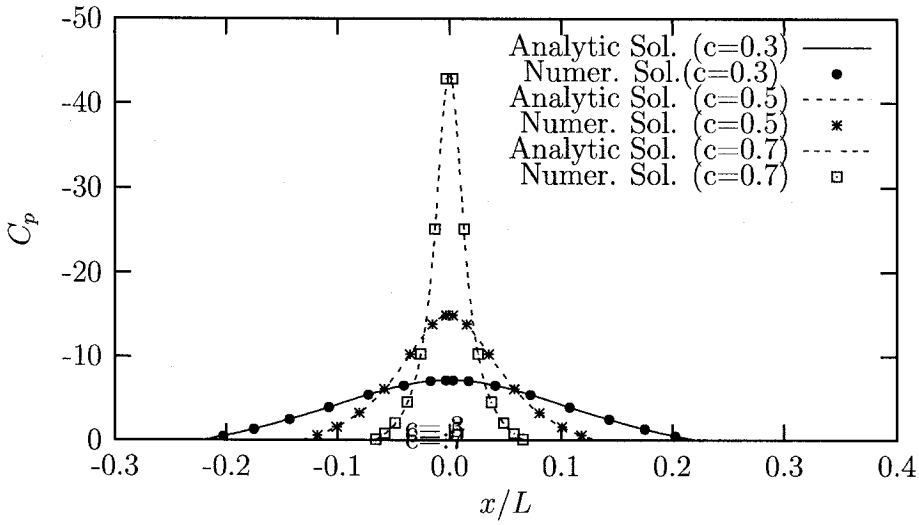

Figure 3.4: Pressure coefficient vs. non-dimensional length, x/L, for a circle ($c = 0$).

two equal parts on which 4, 8, 12, 16, 30 and 50-points Gaussian quadratures are again applied. The pressure coefficient for a Joukowski airfoil is plotted in Figure 3.7. It is shown that the numericalal solutions are in good agreement with the analytic solution. However, since the thickness at the trailing edge of the Joukowski airfoil is zero, all boundary element method codes encounter numerical difficulties in the computation.

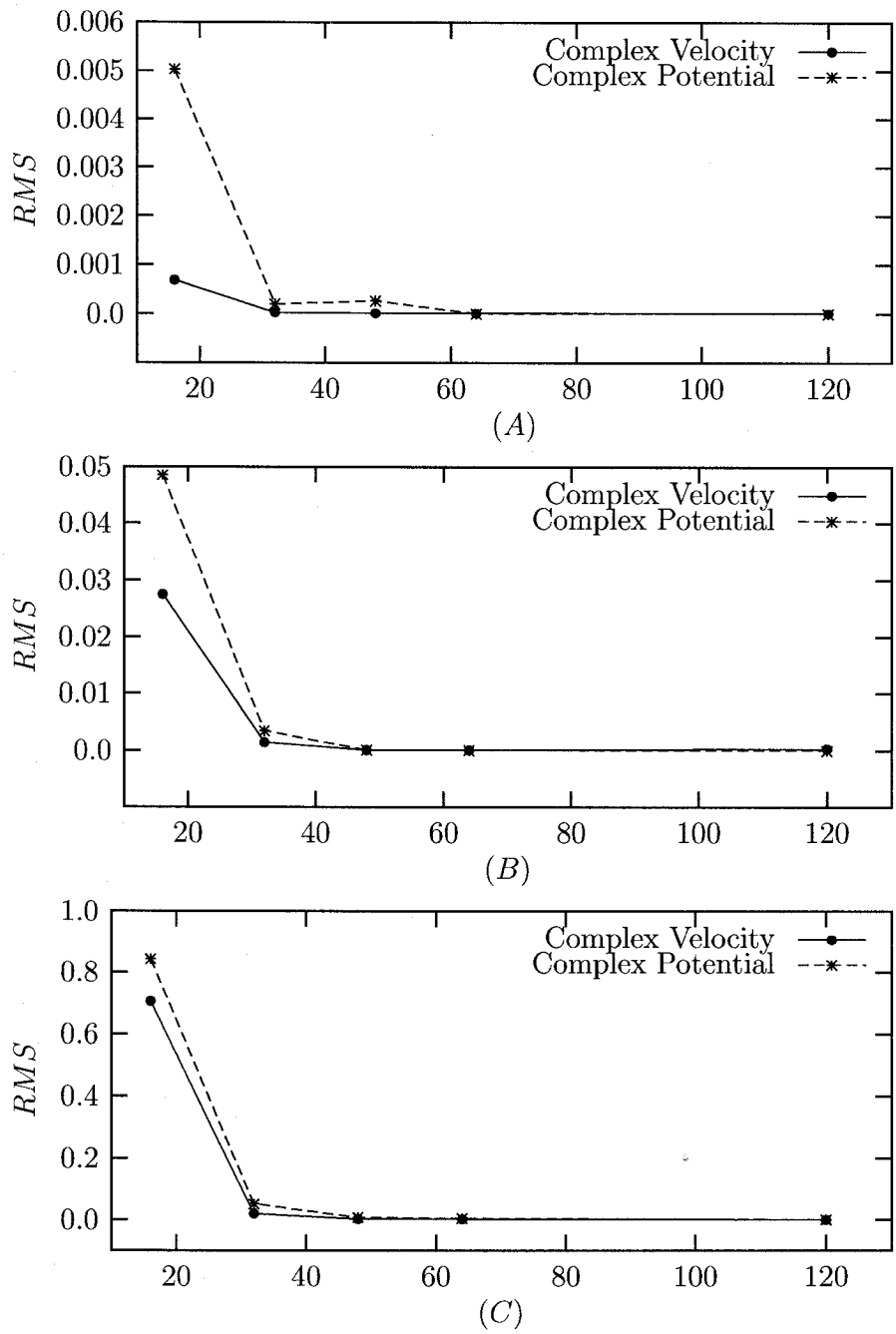

Figure 3.5: RMS of pressure coefficient, C_p, for an ellipse; (A) c=0.3, (B) c=0.5, (C) c=0.7

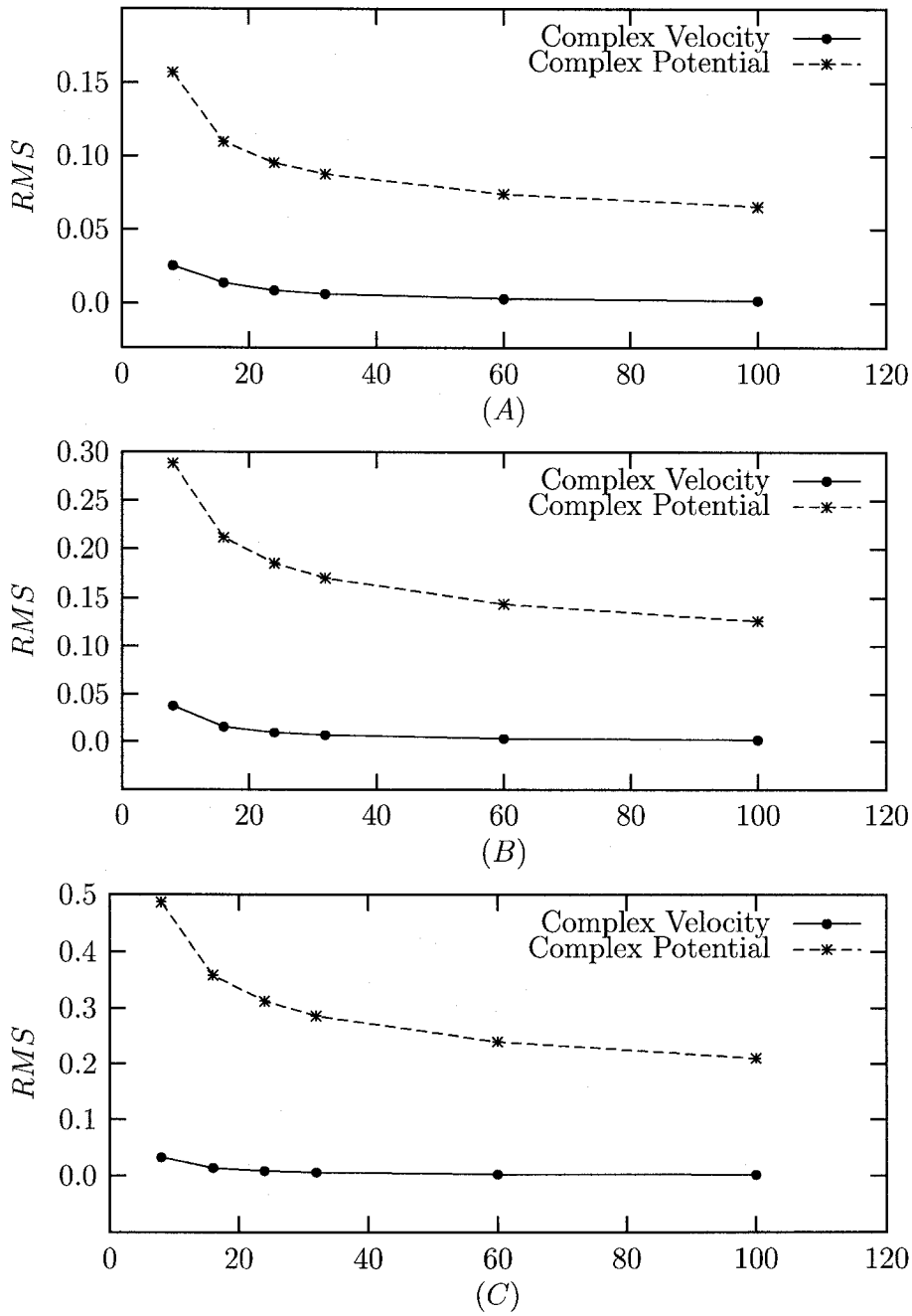

Figure 3.6: RMS of pressure coefficient (C_p) for a Joukowski Airfoil; (A) c=0.3, (B) c=0.5, (C) c=0.7

Figure 3.6 shows the RMS error of pressure coefficient for Joukowski airfoil. It indicates that the velocity formulation gives more accurate results than that of complex potential formulation. It also indicates that increasing the number of collocation points beyond a certain threshold does not significantly improve the accuracy of computation.

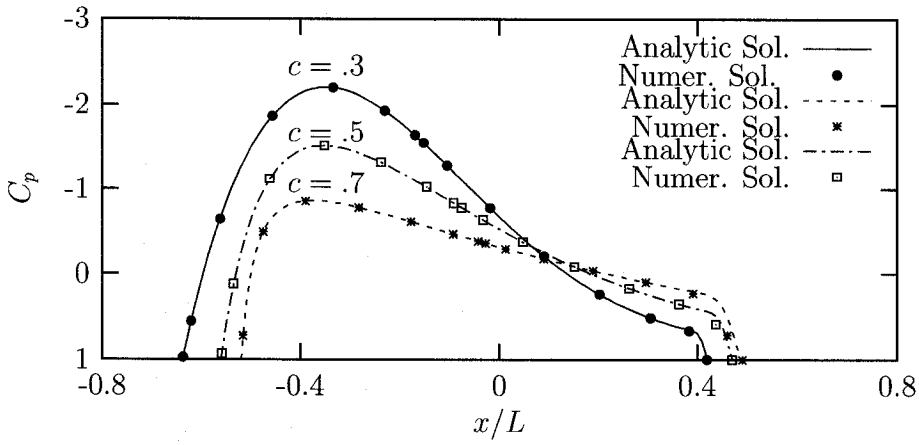

Figure 3.7: Pressure coefficient, C_p, for Joukowski airfoil with different c.

3.3 Hydrofoil Beneath the Free Surface

The desingularized Cauchy's formula is applied for a symmetric foil beneath the free surface. The foil is described by

$$y_{\pm}(x) = -1 \pm \frac{3}{4}b\left(1 - \frac{x}{a}\right)\sqrt{\frac{3}{2}\left(1 + \frac{x}{a}\right)} \tag{3.8}$$

here a is the half length and b is the half breadth of the foil. This foil is the same foil used by Forbes [11] for computation of nonlinear free surface flow. To obtain

numerical values for the unknowns at the free surface and at the body surface, the Gaussian points are distributed on the body surface and the points on the surface are chosen to be equally spaced in the truncated domain. The truncated free surface is from $-l_s/2$ to $l_s/2$, where l_s is the length of truncated free surface and is set to be equal to 20.The radiation condition, Equation (2.50), is imposed at the first surface point, i.e. $-l_s/2$. At this point the Bernoulli's equation also must be satisfied. Hence,

$$y_1 = y_1' = y_1'' = 0, \qquad x_1' = \phi_1' = 1, \qquad x_1 = \phi_1 = s_1 \tag{3.9}$$

where s_1 is the arc length corresponding to the first point at the free surface. Since the free surface is unknown, all the variables on the free surface are also unknown and determination of these variables are also a part of the solution. The $7N + M$ unknown variables are considered in the formulation where $7N$ unknowns are corresponding to free surface and M unknowns are corresponding to the body. The free surface variables are x_i, x_i', x_i'', y_i, y_i', y_i'', and ϕ_i' for $i = 1, 2..., N$ and the variables on the body surface are ϕ_m for $m = 1, 2..., M$. To obtain sufficient equations for determination of dependent functions, the following equations can be written using Equation (2.51), definition of arc length and trapezoidal rule integration.

$$
\begin{aligned}
x'_i &= \sqrt{(1 - y'^2_i)} \\
x_i &= x_{i-1} + \frac{1}{2}(x'_i + x'_{i-1})\Delta s \\
y_i &= y_{i-1} + \frac{1}{2}(y'_i + y'_{i-1})\Delta s \\
x'_i &= x'_{i-1} + \frac{1}{2}(x''_i + x''_{i-1})\Delta s \\
y'_i &= y'_{i-1} + \frac{1}{2}(y''_i + y''_{i-1})\Delta s \\
\phi'_i &= \sqrt{\left(1 - \frac{2y_i}{F^2}\right)} \\
\phi_i &= \phi_{i-1} + \frac{1}{2}(\phi'_i + \phi'_{i-1})\Delta s \qquad \text{for} \quad i = 2, ..., N
\end{aligned} \tag{3.10}
$$

the prime and double prime superscripts in the formula represents the first and second derivatives of the function with respect to the arc length. The algorithm is prepared based on the above procedure and tested for several Froude numbers, various dimensions of the foil and various criteria for implementation of Kutta condition. It was found that no converging solution can be obtained for the problem when the desingularized formulations for free surface and the body are used. However, the modified algorithm prepared in which, the desingularization technique only applied to the body surface part of the integral equation. To obtain the numerical solution the estimate has been made for y'_j and improved using Newton's method. The estimate $y'^{(k)}_j$ at the

kth iteration is updated according to formula

$$y_j'^{(k+1)} = y_j'^{(k)} + \Lambda_j^{(k)} \tag{3.11}$$

where Λ_j is a correction vector. Equation (2.52) at the free surface provides a system of N equations of the form

$$E_i(y_1', y_2', ..., y_N') = 0 \quad \text{for} \quad i = 1, ..., N \tag{3.12}$$

and the correction vector is computed from the matrix equation

$$\sum_{j=1}^{N} \frac{\partial E_i}{\partial y_j'} = -E_i \quad \text{for} \quad i = 1, ..., N \tag{3.13}$$

If at any iteration in the Newton process, a worse estimate than before is obtained, then the correction vector $\Lambda_j^{(k)}$ is halved and the iteration is repeated. For this foil the converged solution was obtained after 23 iteration. The criterion for implementation of Kutta condition, ΔC_p is set to be less than 0.002. Figure 3.8 compares the wave profile obtained by the present method and obtained by nonlinear formulation of Forbes [11]. There are slight errors in the wave profile due to truncation of the free surface in the upstream and downstream. This error seems to be less for the present method than the results obtained by Forbes. A substantial rise can be seen at the free surface obtained by Forbes which does not occur with the present method. The wave height in the present method is less and there is no significant differences between the height of first

wave in the downstream with other wave as can be seen in Forbes results. Figure 3.9 shows the converged solution for various Froude numbers. There is also slight rise in the first wave for different Froude numbers. Numerical simulation studies were carried out to investigate the nonlinear solutions of the foil with an angle of attack, and no converged solutions were obtained. The simulation was also carried out for an ellipse with major semi-axis $a = 1.$ and minor semi-axis $b = 0.25$ moving in the depth of $h = 1.7a$. Fiqure 3.10 shows the wave pattern obtained by the present method and the results of linear and nonlinear solutions given by Campana *et al* [3] and the experimental results given in reference [42]. It is shown that there are differences between the results obtained by the present method and the experimental results, also between the present method and both linear and nonlinear results given by Campana *et al* [3].

The simulation was also carried out for a Joukowski hydrofoil. For the cases of zero angle of attack, the program converged but the results were not as expected. Instead of initial periodic motion, governed by a single frequency, an aperiodic (or perhaps chaotic) wave was observed. However, the amplitude of the wave, gradually declined to eventually reach the convergence criterion.

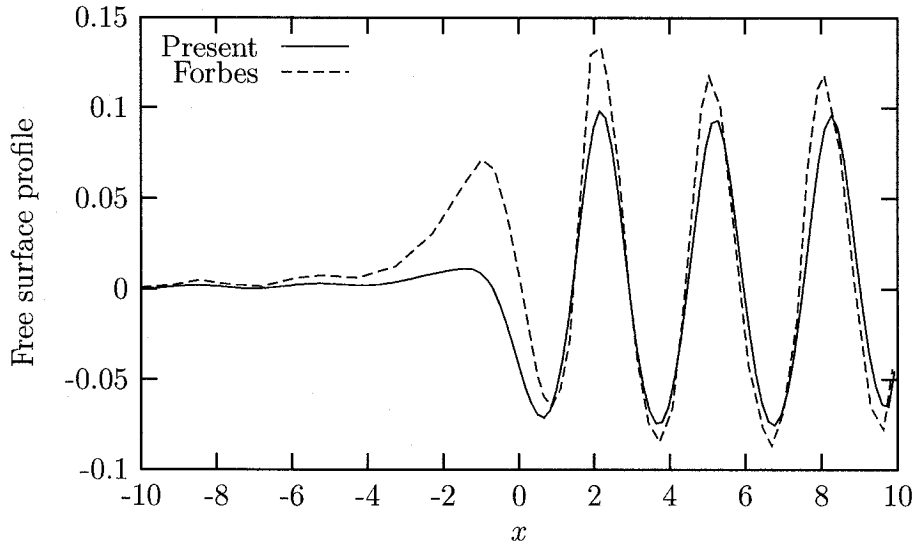

Figure 3.8: Free surface profile generated by a moving hydrofoil beneath the free surface with $F_n = 0.7$, $a = 1$ and $b = 0.15$ ($\beta = 0$)

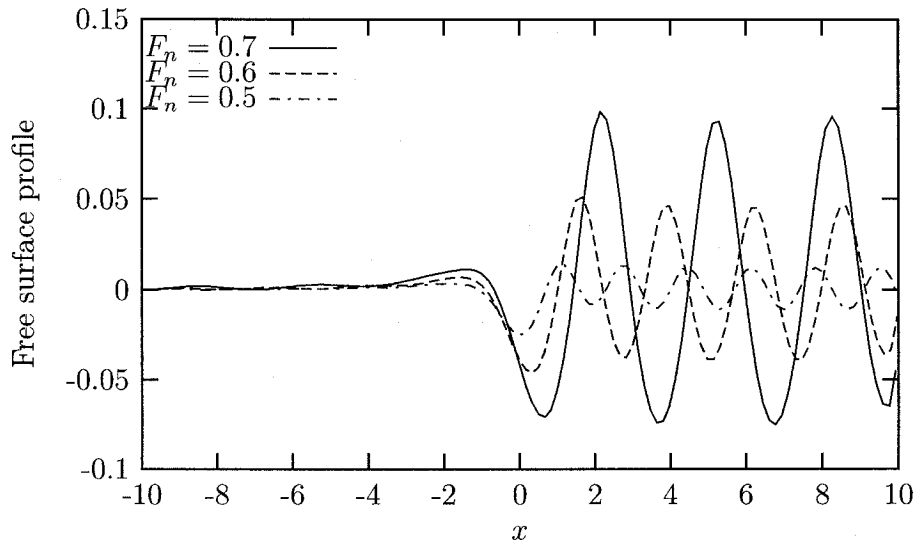

Figure 3.9: Free surface profile generated by a moving hydrofoil beneath the free surface at different F_n; $a = 1$ and $b = 0.15$ ($\beta = 0$)

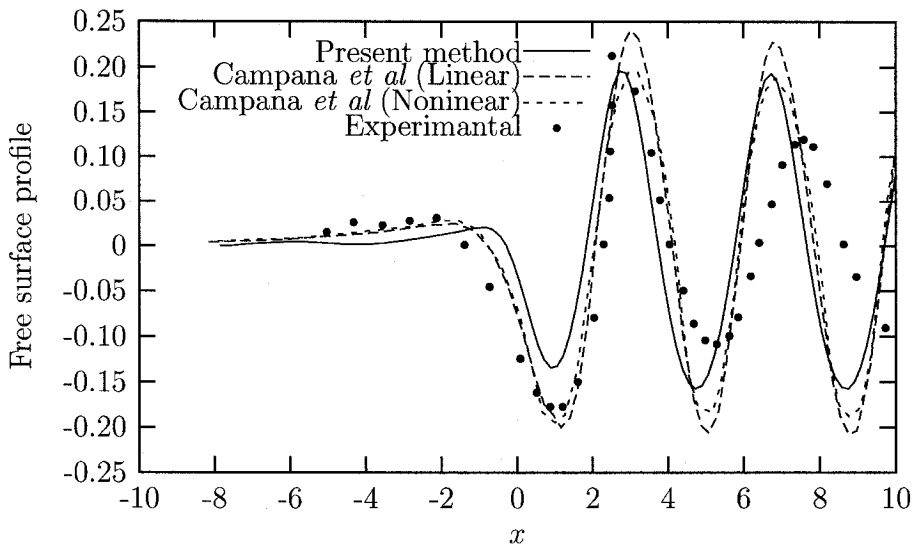

Figure 3.10: Wave pattern generated by a submerged elliptical cylinder; $F_n = 0.57$, $h = 1.7a$, $a = 1$ and $b = 0.15$ ($\beta = 0$)

PART TWO:

THE NUMERICAL SOLUTION OF THREE-DIMENSIONAL WAVE-BODY INTERACTIONS

Chapter 4

Formulation of the Ship Motion Problems

The boundary value problem for analyzing the linear interaction between surface regular waves and a ship moving with steady forward speed is described in this chapter. Assumptions of small waves amplitude and small waves slope and neglecting the viscous effect and the nonlinearities due to free surface and wave-body dynamics allow us to apply the potential theory in this kind of boundary value problem.

The flow potential around a ship is considered to be the sum of the steady flow potential and the unsteady flow potential. The steady flow potential is associated with the forward motion of the ship and the unsteady flow potential is associated with oscillatory motion of the ship. To compute the steady flow potential, the discretized form of the Green's function of double body is derived and used. The unsteady flow potential is obtained using the discretized form of the Green's function of pulsating

source.

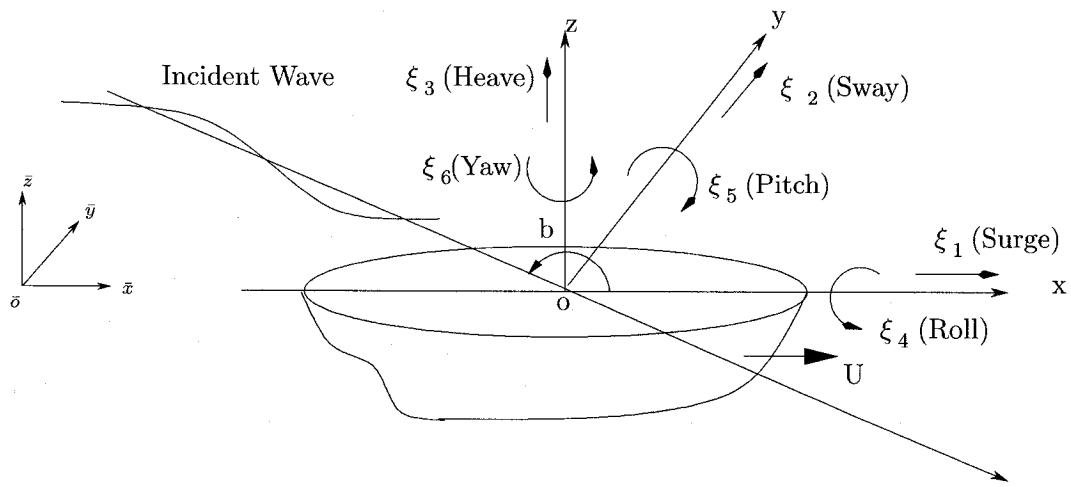

Figure 4.1: Coordinate systems for ship motion.

4.1 Mathematical Formulation for Ship with Steady Forward Speed

The ship advancing at constant steady forward speed in regular waves is considered as shown in Figure 4.1. Three Cartesian coordinate systems are employed to formulate the problem. The space-fixed coordinate system $\bar{o}\bar{x}\bar{y}\bar{z}$ with $\bar{o}\bar{x}\bar{y}$ plane on the undisturbed free surface and the positive $\bar{o}\bar{z}$ axis in upward direction. The coordinate system $oxyz$ is a steady moving system which moves with the mean velocity of the body U with respect to the $\bar{o}\bar{x}\bar{y}\bar{z}$ coordinate system, with the origin o located at the point of intersection of vertical line through center of gravity and undisturbed water surface and the ox axis is in the same direction as the $\bar{o}\bar{x}$ axis. The coordinate $OXYZ$ is fixed in the body with

OX on the direction of ox and OZ pointing upward. The ship has three translational and three rotational motions. Three components of translations are surge, parallel to the longitudinal axis ox, sway in the directional orthogonal to the ox axis and heave in the vertical direction. Three components of rotational motions are roll, pitch and yaw about ox, oy and oz respectively. It is assumed that the fluid is inviscid, homogeneous and incompressible and the flow is irrotational so that the flow around the ship can be described by the potential theory. A linearized analysis of ship motion in incident waves is given by Newman [47].

The fluid velocity vector, $V(\bar{x}, \bar{y}, \bar{z}, t)$, in $\bar{o}\bar{x}\bar{y}\bar{z}$ frame of reference can be represented by

$$V(\bar{x}, \bar{y}, \bar{z}, t) = \nabla\overline{\Phi}(\bar{x}, \bar{y}, \bar{z}, t) \qquad \text{in the fluid domain.} \tag{4.1}$$

where the velocity potential, $\overline{\Phi}(\bar{x}, \bar{y}, \bar{z}, t)$ satisfies Laplace's equation

$$\nabla^2\overline{\Phi} = 0 \qquad \text{in the fluid domain.} \tag{4.2}$$

The fluid pressure is given by Bernoulli's equation

$$p(\bar{x}, \bar{y}, \bar{z}, t) = -\rho(\overline{\Phi}_t + \frac{1}{2}V^2 + g\bar{z}) + p_a \tag{4.3}$$

where ρ is the fluid density, g is the gravitational acceleration, and p_a is the atmospheric pressure, which is assumed to be constant. Appearance of independent variables $\bar{x}, \bar{y}, \bar{z}, t$ as subscript indicates partial differentiation i.e. $\overline{\Phi}_t = \frac{\partial\overline{\Phi}}{\partial t}$. To define the

problem, boundary conditions are imposed on the immersed body surface, on the free surface and at the infinity.

• The local velocity V_s on the body surface and the velocity of the adjacent fluid V match at their interface, thus

$$(V_s - V) \cdot n = 0 \qquad \text{on } S_b \tag{4.4}$$

where the unit normal n is defined to point out of the fluid domain.

• If the free surface is given by $\bar{z} = \zeta(\bar{x}, \bar{y}, t)$, the kinematic boundary condition on the free surface can be expressed by

$$\frac{D}{Dt}(\zeta - \bar{z}) = 0 \qquad \text{on } \bar{z} = \zeta \tag{4.5}$$

where $\frac{D}{Dt}$ is the material derivative given by $\frac{D}{Dt} = \frac{\partial}{\partial t} + \nabla\bar{\Phi} \cdot \nabla$

Since the position of the free surface is unknown, by letting the pressure on the free surface to be equal to atmospheric pressure, additional boundary condition is obtained. Thus, Bernoulli's equation gives

$$\bar{\Phi}_t + \frac{1}{2}V^2 + g\bar{z} = 0 \qquad \text{on } \bar{z} = \zeta \tag{4.6}$$

Equation (4.6) holds on the free surface for all times, therefore, a single boundary condition for the velocity potential can be obtained by setting the material derivative

of Equation (4.6) equal to zero [47]

$$\frac{D}{Dt}\left[\overline{\Phi}_t + \frac{1}{2}|\nabla\overline{\Phi}|^2 + g\bar{z}\right] = 0 \qquad \text{on } \bar{z} = \zeta \tag{4.7}$$

$$\frac{D}{Dt}\left[\overline{\Phi}_t + \frac{1}{2}(\nabla\overline{\Phi}\cdot\nabla\overline{\Phi})\right] + g\frac{D\zeta}{Dt} = 0 \qquad \text{on } \bar{z} = \zeta \tag{4.8}$$

Since $\frac{D\zeta}{Dt} = \frac{\partial\overline{\Phi}}{\partial\bar{z}}$

$$\begin{aligned}
&\left(\frac{\partial}{\partial t} + \nabla\bar{\Phi}\cdot\nabla\right)\left[\overline{\Phi}_t + \frac{1}{2}(\nabla\overline{\Phi}\cdot\nabla\overline{\Phi})\right] + g\frac{D\zeta}{Dt} = \\
&\overline{\Phi}_{tt} + \frac{1}{2}\frac{\partial}{\partial t}(\nabla\overline{\Phi}\cdot\nabla\overline{\Phi}) + \nabla\overline{\Phi}\cdot\nabla\overline{\Phi_t} + \frac{1}{2}\nabla\overline{\Phi}\cdot(\nabla\overline{\Phi}\cdot\nabla\overline{\Phi}) + g\overline{\Phi_{\bar{z}}} = \\
&\overline{\Phi}_{tt} + 2\nabla\overline{\Phi}\cdot\nabla\overline{\Phi}_t + \frac{1}{2}\nabla\overline{\Phi}\cdot\nabla(\nabla\overline{\Phi}\cdot\nabla\overline{\Phi}) + g\overline{\Phi}_Z = 0 \qquad \text{on } \bar{z} = \zeta
\end{aligned} \tag{4.9}$$

Equations (4.4) and (4.9) are the principal boundary conditions for the body surface and the free surface respectively. Following conditions are also imposed to define the problem.

• Bottom boundary condition, that there is no fluid motion at the sea bed

$$V \to 0 \qquad \text{as } \bar{z} \to -\infty \tag{4.10}$$

• Radiation condition which states that the energy flux associated with the disturbance of ship is required to be directed away from the body at infinity.

4.1.1 Linearization of the Problem

Simplifications are needed to solve the problem, because the nonlinear boundary condition, Equation (4.9) preclude any solution of unsteady motion problem. Assuming the amplitude of the oscillatory wave motion is small comparing to the wave length, the body motion and the resulting fluid disturbance is assumed to be small. The second order terms in Equation (4.9) can then be neglected and the linearized free surface boundary condition is obtained

$$\frac{\partial^2 \overline{\Phi}}{\partial t^2} + g\frac{\partial \overline{\Phi}}{\partial \bar{z}} = 0 \qquad \text{on } \bar{z} = 0 \tag{4.11}$$

This condition can be applied on the undisturbed free surface because the difference between the value of $\overline{\Phi}$ or its derivatives on $\bar{z} = \zeta$ and $\bar{z} = 0$ is a second order quantity.

In the steady moving frame of reference $oxyz$, the velocity potential can be expressed as

$$\overline{\Phi}(\bar{x}, \bar{y}, \bar{z}; t) = \overline{\Phi}(x + Ut, y, z) \equiv \Phi_T(x, y, z; t) \tag{4.12}$$

where the total velocity potential Φ_T describes the time independent flow due to the forward motion of the ship and time dependent flow due to oscillatory motion of the ship. The total potential can be written as

$$\begin{aligned} \Phi_T(x, y, z; t) &= U\bar{\phi}(x, y, z) + \Phi(x, y, z; t) \\ &= [-Ux + \phi_s(x, y, z)] + \Phi(x, y, z; t) \end{aligned} \tag{4.13}$$

where Ux is the velocity potential of the uniform flow and ϕ_s is the steady disturbance potential. The sum of velocity potential of uniform flow and the steady disturbance potential $(-Ux + \phi_s)$ is called the steady flow potential.

The boundary condition on the hull surface can be written as

$$W \cdot n = 0 \qquad \text{on } S_b \tag{4.14}$$

where $W = U\nabla(\bar{\phi} - x)$ is the velocity vector of the steady flow relative to the moving frame of reference. By using Taylor series expansion, Newman [47] showed that the unsteady velocity potential is governed by the following first order free surface condition on the steady state free surface $z = \bar{\zeta}$

$$\begin{aligned} &\frac{-(\phi_t + W \cdot \nabla\phi)[\frac{1}{2}\frac{\partial}{\partial z}(W \cdot \nabla W^2) + g\bar{\phi}_{zz}]}{(g + W \cdot W_z)} + \phi_{tt} + 2W \cdot \nabla\phi_t \\ &+W \cdot \nabla(W \cdot \nabla\phi) + \frac{1}{2}\nabla\phi \cdot \nabla(W^2) + g\phi_z = 0 \qquad \text{on } z = \bar{\zeta} \end{aligned} \tag{4.15}$$

Neglecting the perturbation of the flow due to steady forward motion of the ship $(\bar{\phi} = 0)$, i.e. $W = -Ui$, Equation (4.15) reduced to

$$\frac{\partial^2\phi}{\partial t^2} - 2U\frac{\partial^2\phi}{\partial x \partial t} + U^2\frac{\partial^2\phi}{\partial x^2} + g\frac{\partial\phi}{\partial z} = 0 \qquad \text{on } z = 0 \tag{4.16}$$

which is the linear free surface condition in the moving frame of reference.

For a body with steady forward motion, Equation (4.16) becomes

$$U^2\frac{\partial^2\phi}{\partial x^2}+g\frac{\partial\phi}{\partial z}=0 \qquad \text{on } z=0 \tag{4.17}$$

and for a body with no forward speed ($U=0$), Equation (4.16) reduces to

$$\frac{\partial\phi}{\partial z}=0 \qquad \text{on } z=0 \tag{4.18}$$

4.2 Steady Flow Potential

The steady forward motion of a ship will affect the radiated waves and therefore the radiated forces on the ship. In general, the steady potential due to steady forward motion of a ship can not be regarded as a small quantity as described by Wu [74]. The effect of steady flow on the radiated wave is called the steady flow effect which can be represented by well known m_j terms given by Newman [47] as

$$\begin{aligned}(m_1,m_2,m_3)&=-(n\cdot\nabla)W\\(m_4,m_5,m_6)&=-(n\cdot\nabla)(X\times W)\end{aligned} \tag{4.19}$$

where n is the outward normal of the body surfaces and X is the position vector in the steady moving frame of reference $oxyz$.

The steady potential ϕ_s must satisfy the following conditions

•Governing equation:

$$\nabla^2 \phi_s = 0 \qquad \text{for} \quad z < 0 \tag{4.20}$$

•Body boundary condition

$$\frac{\partial \phi_s}{\partial n} = \vec{U} \cdot \vec{n} \qquad \text{on} \quad S_b \tag{4.21}$$

•Linearized free surface condition

$$U^2 \frac{\partial^2 \phi_s}{\partial z^2} + \frac{\partial \phi_s}{\partial z} = 0 \qquad \text{on} \quad z = 0 \tag{4.22}$$

• Radiation condition that the fluid is undisturbed very far from the body

$$\nabla \phi_s = 0 \qquad \text{at infinity} \tag{4.23}$$

For low forward speed the first term in the free surface condition Equation (4.22) can be neglected and the condition is reduced to

$$\frac{\partial \phi_s}{\partial z} = 0 \qquad \text{on} \quad z = 0 \tag{4.24}$$

This is the rigid wall boundary condition and is satisfied by double body potential.

Applying the Green's function method, ϕ_s can be represented as

$$2\pi \phi_s(p) = \int_{S_b} \left\{ \phi_q \frac{\partial G_{db}(p,q)}{\partial n_q} - \frac{\partial \phi}{\partial n_q} G_{db}(p,q) \right\} dS_q + 4\pi \phi_I \tag{4.25}$$

where $G_{db}(p,q)$ is the Green's function of double body potential described by

$$G_{db}(p,q) = \frac{1}{r} + \frac{1}{r_1} \tag{4.26}$$

and p and q are the source and field points, respectively, and

$$\begin{aligned} r &= \sqrt{(x_p - x_q)^2 + (y_p - y_q)^2 + (z_p - z_q)^2)} \\ r_1 &= \sqrt{(x_p - x_q)^2 + (y_p - y_q)^2 + (z_p + z_q)^2)} \end{aligned}$$

The desingularized form of integral equation for steady potential is derived in Appendix A and can be written as

$$2\pi\Phi_s(p) = \int_{S_b} \Phi_q \frac{\partial G_{db}(p,q)}{\partial n_q} dS_q + 4\pi\phi_I \tag{4.27}$$

where Φ_s denotes the total potential of steady flow. When the potential is found, the m_j terms can be obtained from Equation (4.19) which can be used in determination of oscillatory potential components.

4.3 Unsteady Flow Potential

To formulate the unsteady potential function, the idea of Salvesen *et al* [58] is adopted in this work. They used two-dimensional Green function associated with the strip theory formulation to compute ship motions and sea loads. Here, three-dimensional

zero speed Green function is used associated with desingularized formulation instead of two-dimensional Green function. The idea presented by Salvesen *et al* [58] was also used by Inglis [23], Beck and Loken [2] and Hsiung and Huang [19] in computation of ship motion by panel methods and better results are obtained comparing to nonzero speed Green function.

The unsteady potential function for a ship moving in regular wave can be decomposed as suggested by Haskind [12]. It means that the hydrodynamic forces on an oscillating ship in the smooth water and the hydrodynamic forces of a fixed body in water waves can be computed separately.

$$\Phi = \Re\left\{\left(\sum_{j=1}^{6}\eta_j\bar{\phi}_j + \bar{\phi}_D + \phi_I\right)e^{-\mathrm{i}\omega_e t}\right\} \tag{4.28}$$

where $\bar{\phi}_j$ is the oscillatory potential, η_j is the amplitude of the jth mode of motion of the body (surge, sway, heave, roll, pitch and yaw, respectively), $\bar{\phi}_D$ is the diffraction potential, ϕ_I is the incident wave potential and ω_e is the frequency of encounter defined by

$$\omega_e = \omega - \frac{U\omega^2}{g}\cos\beta \tag{4.29}$$

Here, ω is the wave frequency, β is the angle of propagating wave relative to positive x-axis and g is the gravitational acceleration.

The incident wave potential is given in the following form

$$\phi_I = \frac{\mathrm{i}g\eta_a}{\omega}e^{\nu z - \mathrm{i}\nu(x\cos\beta + y\sin\beta)} \tag{4.30}$$

where η_a is the wave amplitude and $\nu = \omega^2/g$ is the wave number. The potentials $\bar{\phi}_D$ and ϕ_I satisfy Laplace's equation and the appropriate conditions at infinity

$$\nabla^2(\bar{\phi}_D, \phi_I) = 0 \qquad \text{in the fluid domain.} \tag{4.31}$$

The incident wave potential ϕ_I, and the diffraction wave potential $\bar{\phi}_D$, must satisfy

$$\frac{\partial \bar{\phi}_D}{\partial n} = -\frac{\partial \phi_I}{\partial n} \qquad \text{on} \quad S_b \tag{4.32}$$

$$\left(i\omega_e - U\frac{\partial}{\partial x}\right)^2 \bar{\phi}_D + g\frac{\partial \bar{\phi}_D}{\partial z} = 0 \qquad \text{on} \quad z = 0 \tag{4.33}$$

$$\left(i\omega_e - U\frac{\partial}{\partial x}\right)^2 \phi_I + g\frac{\partial \phi_I}{\partial z} = 0 \qquad \text{on} \quad z = 0 \tag{4.34}$$

and

the radiation condition.

The oscillatory potential components $\bar{\phi}_j$ $(j = 1, ..., 6)$ in the steady moving frame of reference also satisfy the following conditions

$$\nabla^2 \bar{\phi}_j = 0 \qquad \text{in the fluid domain.} \tag{4.35}$$

$$(i\omega_e - U\frac{\partial}{\partial x})^2 \bar{\phi}_j + g\frac{\partial \bar{\phi}_j}{\partial z} = 0 \qquad \text{on} \quad z = 0 \tag{4.36}$$

$$\frac{\partial \bar{\phi}_j}{\partial n} = -i\omega_e n_j + U m_j \qquad \text{on } S_b \tag{4.37}$$

and

the radiation condition,

where $n_j,\ j = 1, 2, 3$ are the components of a unit vector on the body surface, directed into the body and $n_j = (x, y, z) \times (n_1, n_2, n_3)$ for $j = 4, 5, 6$. m_j depends on the steady motion potential.

The diffraction potential $\bar{\phi}_D$ can be expressed in term of zero speed potential ϕ_D [19]

$$\bar{\phi}_D = \phi_D \tag{4.38}$$

and the oscillatory potential can be divided into two parts

$$\bar{\phi}_j = \phi_j + \frac{U}{i\omega_e}\phi_j^U \tag{4.39}$$

where ϕ_j is the speed independent and ϕ_j^U is speed dependent potentials. Substituting Equation (4.39) into Equation (4.37), two body conditions are obtained

$$\frac{\partial \phi_j}{\partial n} = -i\omega_e n_j \qquad \text{on} \quad S_b \tag{4.40}$$

$$\frac{\partial \phi_j^U}{\partial n} = i\omega_e m_j \qquad \text{on} \quad S_b \tag{4.41}$$

Both ϕ_j and ϕ_j^U satisfy the Laplace's equation, the free surface condition and the infinity conditions.

4.3.1 Hydrodynamic Coefficients

The hydrodynamic pressure p_r due to the radiated wave can be written as

$$p_r = \rho(i\omega_e - U\frac{\partial}{\partial x})\sum_{k=1}^{6}\eta_k\phi_k \tag{4.42}$$

The hydrodynamic forces due to the radiated waves on the ship body can be written as

$$F_j = -\int_{S_b} p_r n_j dS \qquad j = 1, 2, ..., 6 \qquad on \quad S_b \tag{4.43}$$

where n_j is the generalized unit normal of the ship

$$n_j = \begin{cases} \vec{n} & \text{if} \quad j = 1, 2, 3 \\ \vec{r} \times \vec{n} & \text{if} \quad j = 4, 5, 6 \end{cases}$$

Substituting p_r from Equation (4.42) gives

$$F_j = -\rho \int_{S_b} \left\{ n_j \left(\mathrm{i}\omega_e - U\frac{\partial}{\partial x} \right) \sum_{k=1}^{6} \eta_k \phi_k \right\} dS = \sum_{k=1}^{6} T_{jk}\eta_k \tag{4.44}$$

for

$$\begin{aligned} T_{jk} &= -\rho \int_{S_b} \left\{ n_j \left(\mathrm{i}\omega_e - U\frac{\partial}{\partial x} \right) \phi_k \right\} dS \\ &= \omega_e^2 \bar{A}_{jk} - i\omega_e \bar{B}_{jk} \end{aligned} \tag{4.45}$$

T_{jk} denotes the hydrodynamic force and moment in the jth direction per unit oscillatory displacement in the kth mode. The terms $\bar{A}_{jk}$ and $\bar{B}_{jk}$ are the added-mass and damping coefficient, respectively. Using Stokes theorem, T_{jk} can be written in the following form

$$T_{jk} = -\rho i\omega_e \int_{S_b} n_j \phi_k dS + \rho U \int_{S_b} m_j \phi_k dS - \rho U \int_{C_w} n_j \phi_k dl \tag{4.46}$$

C_w represents the ship's water line on the free surface. When the body is long and thin the line integral becomes very small and may be neglected [47]. If the body has no forward speed or is completely submerged the line integral disappears. Hence, T_{jk} can be written as

$$T_{jk} = -\rho i\omega_e \int_{S_b} n_j \phi_k dS + \rho U \int_{S_b} m_j \phi_k dS \tag{4.47}$$

4.3.2 Wave Exciting Forces and Moments

The hydrodynamic pressure due to diffracted and incident waves is

$$p_w = (i\omega_e - U\frac{\partial}{\partial x})(\phi_D + \phi_I) \tag{4.48}$$

The wave exciting forces and moments acting on the ship can be expressed as

$$\begin{aligned} F_{wj} &= -\rho i\omega_e \int_{S_b} (\phi_D + \phi_I) n_j dS + \rho U \int_{S_b} \frac{\partial}{\partial x}(\phi_D + \phi_I) n_j dS \\ &= F_j^D + F_j^I \qquad \text{for } j = 1, 2, ...6 \end{aligned} \tag{4.49}$$

where F^D and F^I are diffracted wave force and incident wave force respectively.

4.3.2.1 Diffracted Wave Force

The diffracted wave on the ship hull for jth mode of motion can be written as

$$F_j^D = -\rho i\omega_e \int_{S_b} \phi_D n_j dS + \rho U \int_{S_b} \frac{\partial}{\partial x}\phi_D n_j dS \qquad \text{for } j = 1, 2, ...6 \tag{4.50}$$

using the Stokes theorem Equation (4.50) can be expressed in the following form

$$F_j^D = -\rho i\omega_e \int_{S_b} \phi_D n_j dS + \rho U \int_{S_b} m_j \phi_D dS \qquad \text{for } j = 1, 2, ...6 \tag{4.51}$$

4.3.2.2 Incident Wave Force

Considering the contribution of incident potential and neglecting the contribution of radiated wave and diffracted wave on the ship hull, the wave force is the so called Froude-Krylov forces and moments or incident wave force expressed by

$$F_j^I = -\rho i\omega_e \int_{S_b} \phi_I n_j dS + \rho U \int_{S_b} \frac{\partial}{\partial x}\phi_I n_j dS \qquad \text{for } j = 1, 2, ...6 \tag{4.52}$$

Substituting ω_e and Φ_I from Equation 4.29 and Equation 4.30 into Equation 4.53 yield

$$\begin{aligned} F_j^I &= -\rho \mathbf{i}\left(\omega - \frac{U\omega^2}{g}\cos\beta\right)\int_{S_b}\phi_I n_j dS + \rho U\int_{S_b}(-\mathbf{i}\nu\cos\beta)\phi_I n_j dS \\ &= -\rho \mathbf{i}\left(\omega - \frac{U\omega^2}{g}\cos\beta\right)\int_{S_b}\phi_I n_j dS - \rho \mathbf{i}\frac{U\omega^2}{g}\cos\beta\int_{S_b}\phi_I n_j dS \\ &= -\rho \mathbf{i}\omega\int_{S_b}\phi_I n_j dS \qquad \text{for } j = 1, 2, ...6 \end{aligned} \tag{4.53}$$

Equation (4.53) states that the Froude-Krylov forces and moments are independent of forward speed. This implies that, if the steady perturbation potential is small and negligible then, the wave exciting forces and moments for motions which have speed independent velocity potential , i.e. surge, sway, heave and roll motions (corresponding to $m_j = 1, 2, 3, 4$, in Equation (4.51), respectively) are independent of the velocity of the ship and are determined by wave heading, wave frequency and wave amplitude.

4.3.3 Equation of Motions

The equation of motions of a ship advancing with constant speed in water waves can be written in the form

$$\sum_{k=1}^{6}\Big[-{\omega_e}^2(\overline{M}_{jk} + \overline{A}_{jk}) - i\omega_e\overline{B}_{jk} + \overline{C}_{jk}\Big]\eta_k = F_{wj} \qquad \text{for} \quad j = 1, 2, ..., 6 \tag{4.54}$$

where $\overline{M}_{jk}$ is the generalized mass matrix of the ship, $\overline{A}_{jk}$ and $\overline{B}_{jk}$ are the added-mass and damping coefficients matrix, respectively. $\overline{C}_{jk}$ is restoring force coefficient of the ship.

In order to solve the equations of motion, one need first to compute the wave exciting forces and moments, added-mass and damping coefficients, mass matrix and restoring coefficients of the ship.The wave exciting forces and moments can be obtained from Equation (4.49). The added-mass and damping coefficients are computed from Equation (4.45). These components are expressed in terms of radiation and diffraction of a body with zero speed in regular waves. Therefore by solving the radiation and diffraction problem of a ship with zero forward speed in regular waves the equation of motions of a ship advancing with constant speed in water wave can be solved.

For a body with lateral symmetry the generalized mass matrix, $\overline{M}_{jk}$ may be written [58]

$$\overline{M}_{jk} = \begin{pmatrix} M & 0 & 0 & 0 & Mz_g & 0 \\ 0 & M & 0 & -Mz_g & 0 & 0 \\ 0 & 0 & M & 0 & 0 & 0 \\ 0 & -Mz_g & 0 & I_4 & 0 & -I_{46} \\ Mz_g & 0 & 0 & 0 & I_5 & 0 \\ 0 & 0 & 0 & -I_{64} & 0 & I_6 \end{pmatrix} \tag{4.55}$$

where M is the mass of the ship, z_g is the position of center of gravity, I_j is the moment of inertia in the jth mode and I_{jk} is the cross product of inertia.

$\overline{C}_{jk}$ is the restoring force coefficient matrix of the ship defined by [58]

$$\overline{C}_{jk} = \begin{pmatrix} 0 & 0 & 0 & 0 & 0 & 0 \\ 0 & 0 & 0 & 0 & 0 & 0 \\ 0 & 0 & \rho g A_W & 0 & -\rho g M_{WP} & 0 \\ 0 & 0 & 0 & -\rho g M_{WP} & 0 & 0 \\ 0 & 0 & -\rho g M_{WP} & 0 & \rho g I_{WP} & 0 \\ 0 & 0 & 0 & 0 & 0 & 0 \end{pmatrix} \tag{4.56}$$

where A_{WP}, M_{WP} and I_{WP} are the area, moment and moment of inertia of water plane, respectively.

For ships with lateral symmetry the added-mass (or damping) coefficients are [58]

$$\overline{A}_{jk}(or\overline{B}_{jk}) = \begin{pmatrix} \bar{A}_{11} & 0 & \bar{A}_{13} & 0 & \bar{A}_{15} & 0 \\ 0 & \bar{A}_{22} & 0 & \bar{A}_{24} & 0 & \bar{A}_{26} \\ \bar{A}_{31} & 0 & \bar{A}_{33} & 0 & \bar{A}_{35} & 0 \\ 0 & \bar{A}_{42} & 0 & \bar{A}_{44} & 0 & \bar{A}_{46} \\ \bar{A}_{51} & 0 & \bar{A}_{53} & 0 & \bar{A}_{55} & 0 \\ 0 & \bar{A}_{62} & 0 & \bar{A}_{64} & 0 & \bar{A}_{66} \end{pmatrix} \tag{4.57}$$

4.4 Roll Motion Correction

Linear potential flow theory cannot give satisfactory roll motion results, when compared with the experimental results [58]. This is due to the significant effect of viscosity in

roll damping coefficient. A correction factor is obtained based on the method proposed by Schmitke [60] and adopted to calculate the viscous roll damping of the body.

4.5 Linearized Motion of a Body with Zero Forward Speed in Waves

Considering a body with no forward speed is moving in regular waves in water of infinite depth. The boundary conditions described for a body with forward speed are simplified and the boundary conditions, which the linearized velocity potential must satisfies can be written as [46]

•The free surface boundary condition

$$\frac{\partial \phi}{\partial z} - \nu\phi = 0 \qquad \text{on} \quad z = 0 \tag{4.58}$$

•The sea bed condition

$$\frac{\partial \phi}{\partial z} = 0 \qquad \text{on} \quad z = -\infty \tag{4.59}$$

•The radiation condition

$$\lim_{R\to\infty} \sqrt{R}(\frac{\partial \phi}{\partial R} - i\nu\phi) = 0 \tag{4.60}$$

•The body boundary condition

$$\begin{aligned} \frac{\partial \phi_D}{\partial n} &= -\frac{\partial \phi_I}{\partial n} \qquad \text{on} \quad S_b \\ \frac{\partial \phi_j}{\partial n} &= i\omega n_j \qquad j = 1, 2, ..., 6 \qquad \text{on} \quad S_b \end{aligned} \tag{4.61}$$

where $R = \sqrt{(x - x_o)^2 + (y - y_o)^2}$ and ν is the wave number.

Wehausen and Laiton [72] gave the Green function for Laplace's equation satisfying

the boundary conditions for a source of unit strength situated at (x_0, y_0, z_0) in water of infinite depth as

$$G(p,q) = \frac{1}{r} + PV \int_0^\infty \frac{\nu + \nu_0}{\nu - \nu_0} e^{\nu(z+z_0)} J_0(\nu_0 R)\, d\nu_0 - 2\pi i \nu e^{\nu(z+z_0)} J_0(\nu R) \tag{4.62}$$

where

$$\begin{cases} R = \sqrt{(x-x_o)^2 + (y-y_o)^2} \\ r = \sqrt{(x-x_o)^2 + (y-y_o)^2 + (z-z_o)^2} \end{cases}$$

p and q denote the field point and source point, respectively, and J_0 is the first kind Bessel function of zero order. PV indicates that the integral is to be interpreted in the Cauchy principal value sense.

In another form, the Green function can be expressed as the summation of three terms

$$G(p,q) = G_s(p,q) + G_I(p,q) + G_w(p,q) \tag{4.63}$$

where $G_s(p,q) = \frac{1}{r}$ is the part of Green function corresponding to the simple singularity, $G_I(p,q)$ is due to the image of the singularity

$$G_I(p,q) = \frac{1}{r_1} = \frac{1}{\sqrt{(x-x_o)^2 + (y-y_o)^2 + (z+z_o)^2}} \tag{4.64}$$

and $G_w(p,q)$ is the wave part of the Green function. Another useful form of Green

function can be written as

$$\begin{aligned} G(p,q) &= \frac{1}{r} + \frac{1}{r_1} + 2\nu\, PV \int_0^\infty \frac{1}{\nu - \nu_0} e^{\nu(z+z_0)} J_0(\nu R)\, d\nu - 2\pi i \nu e^{\nu(z+z_0)} J_0(\nu R) \\ &= \frac{1}{r} + G^*(p,q) \end{aligned} \tag{4.65}$$

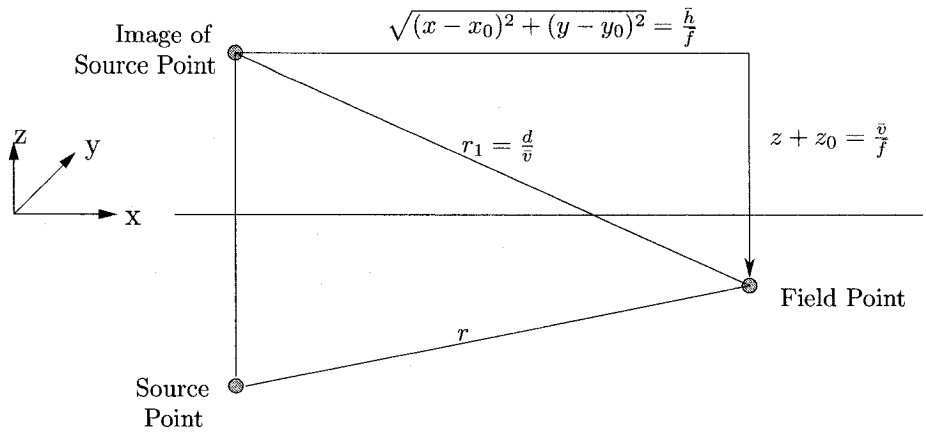

Figure 4.2: Definition of points (adopted from Ref. [68])

An efficient and accurate form of the Green function for numerical computation of wave diffraction and radiation problem given in Equation (4.65) has been developed by Talste and Noblesse [68]. This form of Green function is adopted throughout this study. A definition sketch is depicted in Figure 4.2. Here, r and r_1 are the distance of

field point to source point and the image of source point, respectively, and

$$\begin{aligned} \bar{f} &= \frac{\omega^2 L}{g} \\ \bar{v} &= \bar{f}(z + z_0) \\ d &= \sqrt{\bar{h}^2 + \bar{v}^2} \\ R &= \sqrt{(x - x_0)^2 + (y - y_0)^2} \\ \bar{h} &= \bar{f} R \end{aligned} \tag{4.66}$$

4.6 Desigularization of Boundary Integral Equation

The desigularization technique in the boundary integral equation of potential flow problems has been used by several researchers. Maniar [40] used this technique in three-dimensional higher order panel method for potential problems. Kouh and Suen [33] also adopted the method to deal with the potential flow problem. An extensive review on the desigularization methods is presented by Yang [77]. The Green's formula for solving three-dimensional exterior potential problem which represents the Laplace's equation is written as [39]

$$\int_{S_b} \left\{ \phi_q \frac{\partial G}{\partial n_q} - G \frac{\partial \phi}{\partial n_q} \right\} dS_q = \begin{cases} 0 & p \in \Omega_i \text{ interior} \\ 2\pi\phi_p & p \in S_b \\ 4\pi\phi_p & p \in \Omega_e \text{ exterior} \end{cases} \tag{4.67}$$

where $\partial/\partial n_q$ denotes the differential in normal direction at the source point $q(x_o, y_o, z_o)$ and the field point $p(x, y, z)$. Substituting Equation (4.63) into Equation (4.67), one obtains the integral equation for the point on the body surface in the following form

$$\begin{aligned}&\int_{S_b}\left\{\phi_q\frac{\partial G_s}{\partial n_q}-G_s\frac{\partial\phi}{\partial n_q}\right\}dS_q+\int_{S_b}\left\{\phi_q\frac{\partial G_I}{\partial n_q}-G_I\frac{\partial\phi}{\partial n_q}\right\}dS_q\\&+\int_{S_b}\left\{\phi_q\frac{\partial G_w}{\partial n_q}-G_w\frac{\partial\phi}{\partial n_q}\right\}dS_q=2\pi\phi_p\qquad p\in S_b\end{aligned}\tag{4.68}$$

The single and and double-layer kernel involved in the first integral of Equation (4.68) appear to be singular as the field point approaches source point, $r \to 0$. While no singularity involves in the kernel of second and third integral of Equation (4.68).

The singular integral in the boundary integral Equation (4.68) can be desingularized and the desingularized form of the integral equation based on the procedure proposed by Landweber and Macagno [36] can be written as

$$\begin{aligned}&\int_{S_b}(\phi_q-\phi_p)\frac{\partial G_s}{\partial n_q}dS_q+\phi_p\int_{S_b}\frac{\partial G_s}{\partial n_q}dS_q-\int_{S_b}G_s\left(\frac{\partial\phi}{\partial n_q}-\frac{\partial\phi}{\partial n_p}\frac{\sigma_q}{\sigma_p}\right)dS_q\\&-\frac{\partial\phi}{\partial n_p}\frac{1}{\sigma_p}\int_{S_b}G_s\sigma_q dS_q+\int_{S_b}\left\{\phi_q\frac{\partial G_I}{\partial n_q}-G_I\frac{\partial\phi}{\partial n_q}\right\}dS_q\\&+\int_{S_b}\left\{\phi_q\frac{\partial G_w}{\partial n_q}-G_w\frac{\partial\phi}{\partial n_q}\right\}dS_q=2\pi\phi_p\end{aligned}\tag{4.69}$$

According to the Gauss flux theorem, the flux through a closed surface due to a

unit source on the same surface is 2π. Hence,

$$\int_{S_b} \frac{\partial G_s}{\partial n_q} dS_q = -2\,\pi \tag{4.70}$$

where, σ is a source distribution on the body surface which makes the body surface an equipotential defined by

$$\phi_e = -\int_{S_b} G_s \sigma_q dS_q \tag{4.71}$$

Making use of Equations (4.70) and (4.71), Equation (4.69) can be re-written as

$$\begin{aligned}
&\int_{S_b} (\phi_q - \phi_p) \frac{\partial G_s}{\partial n_q} dS_q - \int_{S_b} G_s \left(\frac{\partial \phi}{\partial n_q} - \frac{\partial \phi}{\partial n_p} \frac{\sigma_q}{\sigma_p} \right) dS_q \\
&+ \frac{\partial \phi}{\partial n_p} \frac{\phi_e}{\sigma_p} \int_{S_b} G_s \sigma_q dS_q + \int_{S_b} \left\{ \phi_q \frac{\partial G_I}{\partial n_q} - G_I \frac{\partial \phi}{\partial n_q} \right\} dS_q \\
&+ \int_{S_b} \left\{ \phi_q \frac{\partial G_w}{\partial n_q} - G_w \frac{\partial \phi}{\partial n_q} \right\} dS_q = 4\pi \phi_p
\end{aligned} \tag{4.72}$$

The corresponding integral equation to solve source function σ on the body surface can be expressed as

$$2\pi\sigma_p = -\int_{S_b} \frac{\partial G_s}{\partial n_q} dS_q \tag{4.73}$$

Using the "subtracting and adding back" technique, Equation (4.73) can be written as

$$2\pi\sigma_p = -\int_{S_b} \left\{ \sigma_q \frac{\partial G_s}{\partial n_p} - \sigma_p \frac{\partial G_s}{\partial n_q} \right\} dS_q - \sigma_p \frac{\partial G_s}{\partial n_q} dS_q \tag{4.74}$$

Applying the Gauss flux theorem, Equation (4.73) is reduced to

$$\int_{S_b} \left\{ \sigma_q \frac{\partial G_s}{\partial n_p} - \sigma_p \frac{\partial G_s}{\partial n_q} \right\} dS_q = 0 \tag{4.75}$$

Equation (4.75) implies that σ is an eigenvector of the normal derivative of the single-layer operator [77]. By specifying a given value for σ at some point on the surface and making use of an iteration method, a unique solution for Equation 4.75 can be obtained

$$\sigma_p^{(m+1)} = \sigma_p^{(m)} + \int_{S_b} \left\{ \sigma_q^{(m)} \frac{\partial G_s}{\partial n_p} - \sigma_p^{(m)} \frac{\partial G_s}{\partial n_q} \right\} dS_q - \sigma_p \frac{\partial G_s}{\partial n_q} dS_q \tag{4.76}$$

The equipotential function ϕ_e can be obtained by locating p on the origin inside the boundary surface

$$\phi_e = -\int_{S_b} \frac{\sigma_q}{\sqrt{x_o^2 + y_o^2 + z_o^2}} dS_q \tag{4.77}$$

where superscript m refers to mth iteration. By locating p at the origin inside the body ϕ_e is obtained.

4.6.1 Radiation Problem

The associated boundary integral equation for a radiation problem is given as follows:

$$2\pi\phi_j(p) - \int_{S_b} \phi_j(q) \frac{\partial G^*(p,q)}{\partial n_q} dS_q = \int_{S_b} \frac{\partial \phi_j}{\partial n_q} G(p,q) dS_q \tag{4.78}$$

Using the desingularized technique, Equation (4.78) can be written in the following form

$$\begin{aligned} 4\pi\phi_j(p) \;-\; & \int_{S_b}\Big\{\phi_j(q)-\phi_j(p)\Big\}\frac{\partial G_r(p,q)}{\partial n_q}dS_q - \int_{S_b}\phi_j(q)\frac{\partial G^*(p,q)}{\partial n_q}dS_q \\ = \; & \int_{S_b} G^*(p,q)\frac{\partial \phi_j}{\partial n_q}dS_q - \int_{S_b} G_r(p,q)\left(\frac{\partial \phi_j}{\partial n_q} - \frac{\partial \phi_j}{\partial n_p}\frac{\sigma_q}{\sigma_p}\right)dS_q \\ & -\frac{\partial \phi_j}{\partial n_p}\frac{1}{\sigma_p}\phi_e \end{aligned} \tag{4.79}$$

4.6.2 Diffraction Problem

For the wave diffraction problem, the associated boundary integral equation is written as

$$2\pi\phi_A(p) - \int_{S_b}\phi_A(q)\frac{\partial G(p,q)}{\partial n_q}dS_q = 4\,\pi\phi_I(p) \tag{4.80}$$

and the desingularized form of Equation (4.80) can be written as

$$\begin{aligned} 4\pi\phi_A(p) \;-\; & \int_{S_b}\Big\{\phi_A(q)-\phi_A(p)\Big\}\frac{\partial G_r(p,q)}{\partial n_q}dS_q - \int_{S_b}\phi_A(q)\frac{\partial G^*(p,q)}{\partial n_q}dS_q \\ = \; & 4\,\pi\phi_I(p) \end{aligned} \tag{4.81}$$

where $\phi_A = \phi_D + \phi_I$.

4.7 Geometry Description of the Body by NURBS

A surface, over which the integral equation is to be solved, is generally given by a set of data points. In order to evaluate the desingularized boundary integral equation, a parametric description of the body geometry is required to distribute the collocation points over the body surface. B-splines and Non-Uniform Rational B-splines (NURBS) are the powerful methods for generating a curve or surface through a set of given data points to describe the geometry of the body. In hydrodynamic computation, the B-splines was used for two-dimensional potential flow by Okan and Umpleby [50,51] and Landrini *et al* [35]. A B-spline based panel method is also presented by Maniar [40]. Scalvounos and Nakos [59] applied the spline element to express the velocity potential distribution on the free surface for rankine panel method. Kouh and Suen [33], Lee [38], Sheng [62] and Qiu [53] applied the NURBS to model the geometry of the body for potential flow computation. In this study, the NURBS surface is used to describe the body geometry. The reason of choosing the NURBS surface to describe the geometry is that NURBS offers curve and surface fitting with very small curvature. It also offers one common mathematical form for representation of standard analytic shape (conic, circle,...) as well as free form shape. The NURBS representation of the geometry can also be used in other ship design applications. The flexibility to design a large variety of shapes as well as numerically stable and accurate algorithms are also provided by NURBS. Moreover, the NURBS description of the body also facilitates to modify the body if the satisfactory requirements of the hydrodynamic characteristic of the body are

not achieved. A brief description of of NURBS surface and generation of an arbitrary body surface by NURBS is given in Appendix B.

Chapter 5

Three-Dimensional Numerical Results and Discussions

This chapter provides validation of numerical simulations using the proposed method with analytical results, or available experimental data, or published numerical results in the literatures. First, the steady flow potentials are computed and compared with the analytical results for a sphere and an ellipsoid. Then, the hydrodynamic characteristics of a spheroid are computed and compared with the numerical results obtained by panel method and the published analytical results. Finally, the numerical solutions of ship motion characteristics obtained by desingularized method for a Wigley hull and a Container ship compared with experimental data and other available numerical solutions. The computational procedure is shown in Appendix C.

5.1 Numerical Results for Steady Flow Potential

Different numerical simulation runs were carried out for sphere and ellipsoid to demonstrate the accuracy of the desingularized method in potential flow computation. In the first example, a sphere with radius of one is floating in a uniform flow. The fluid flow is from left to right with the speed of $U = 1$. It is worth mentioning that the NURBS surface representation of sphere can be obtained by the revolution of a circle or by surface interpolating through a set of data points. However, since an arbitrary body has no mathematical description and cannot be dealt as the ruled surface, the NURBS surfaces of the sphere and ellipsoid are generated using data points. The basis orders of the NURBS surface are $p \times q$ and the Gaussian orders of the body surface are N_1 and N_2 in the u and v-directions, respectively. For the sphere, four equal-spaced stations are selected in the x-direction and five points on each station are selected so that the distances between them are equal. The coordinates of these points are calculated from the mathematical description of the sphere. The NURBS surface is fitted to these points. Then, the coordinates and other parameters of the Gaussian points on the NURBS surface are computed. The results of total potential for different order of Gaussian points, depicted in Figure 5.1, show a reasonable agreement with the analytical solution. The analytical solution can be found in the hydrodynamic book [44]. Term θ is the angle in the xy-plane from the negative direction of x-axis with $0 \leq \theta \leq \pi$. Figure 5.2 shows the analytical solution and the numerical results of pressure coefficient, C_p, for a sphere with different number of Gaussian points. The

root mean square error of total potential for the sphere defined by

$$RMS = \sqrt{\frac{1}{N}\sum_{i=1}^{N}\left\{\frac{\Phi_i^{analytic} - \Phi_i^{num.}}{\Phi_i^{analytic}}\right\}^2} \tag{5.1}$$

where N is the total number of Gaussian points on the body surface.

The root mean square error for potential is plotted in Figure 5.3 for different order of basis function in NURBS surface.

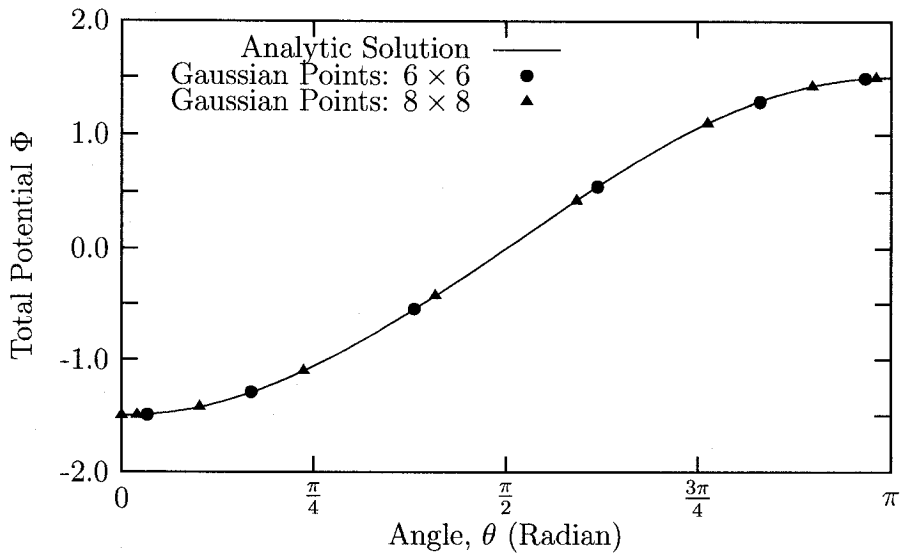

Figure 5.1: Total potential for a sphere

Figure 5.3 indicates that increasing the Gaussian order and the number of Gaussian points in the body surface increases the accuracy of computation. However, it is shown that with a few number of Gaussian points and low order of Gaussian quadrature, accurate result can be obtained.

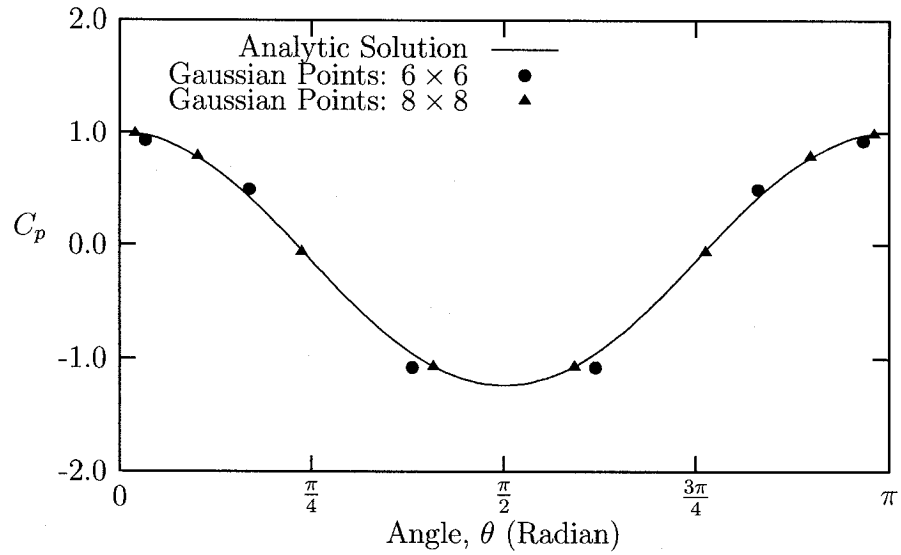

Figure 5.2: Pressure coefficient for a sphere

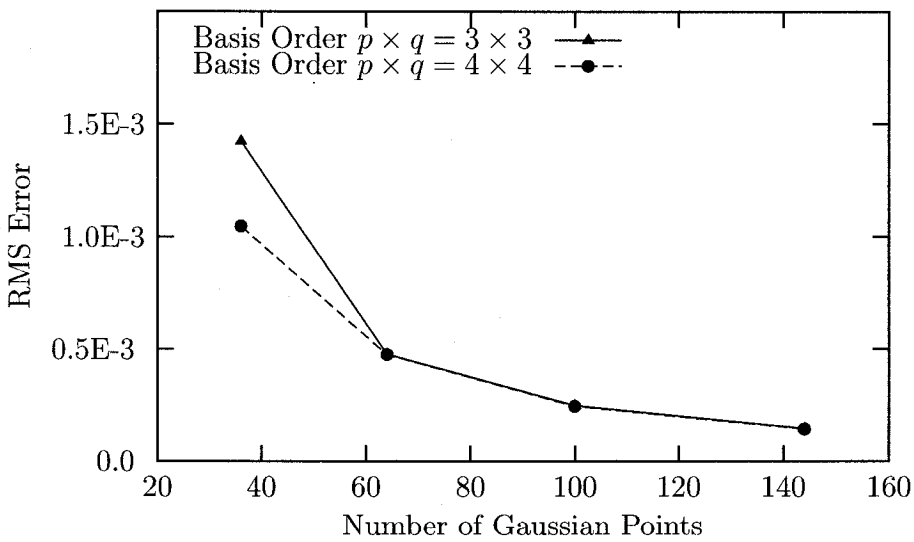

Figure 5.3: Error of potential for a sphere

In order to simulate potential flow for a semi-ellipsoid moving in the calm water, a semi ellipsoid with semi axis $a = 4, b = 1$ and $c = 2$ is chosen. The NURBS surface of the ellipsoid is generated for three cases, for which 256, 192 and 128 Gaussian points are distributed on the body surface. The basis order of the NURBS surfaces for the three cases are 3×3. The NURBS surface with different number of Gaussian points are depicted on Figure 5.5. Table 5.1 shows the analytical solutions and the numerical results of velocity potential for the ellipsoid. The results for three cases show good agreement with the analytical results. The relative error, RE, which is defined by $RE = \left| \frac{\Phi^{analytic} - \Phi^{num.}}{\Phi^{analytic}} \right|$ is shown in Figure 5.4. It is indicated that the relative error is less than 0.1 percent for the points located on the middle part of the surface but the error is greater for the points located on both end parts of the surface of ellipsoid.

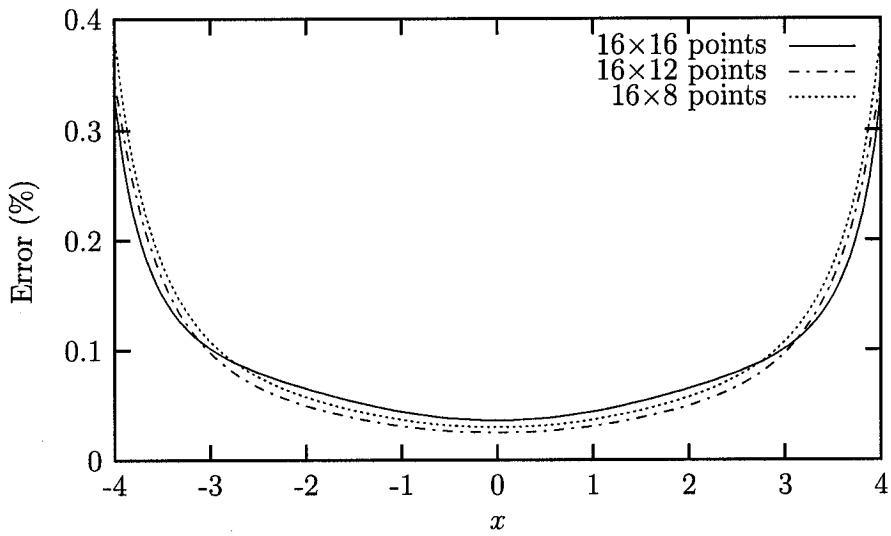

Figure 5.4: Relative error of potential for an ellipsoid

Table 5.1: Velocity potential for an ellipsoid ($a = 4, b = 1, c = 2$)

		Numerical		
x	Analytical*	16×16	16×12	16×8
3.9959	4.5017	4.4868	4.4862	4.4843
3.9078	4.4024	4.3905	4.3883	4.3883
3.6382	4.0987	4.0959	4.0937	4.0926
3.2031	3.6085	3.6124	3.6101	3.6101
2.6338	2.9672	2.9741	2.9718	2.9726
1.9588	2.2067	2.2136	2.2115	2.2126
1.2067	1.3594	1.3642	1.3628	1.3636
0.4075	0.4591	0.4608	0.4603	0.4606
-0.4075	-0.4591	-0.4608	-0.4603	-0.4606
-1.2067	-1.3594	-1.3642	-1.3628	-1.3636
-1.9588	-2.2067	-2.2136	-2.2115	-2.2126
-2.6338	-2.9672	-2.9741	-2.9718	-2.9726
-3.2031	-3.6085	-3.6124	-3.6101	-3.6101
-3.6382	-4.0987	-4.0959	-4.0937	-4.0926
-3.9078	-4.4024	-4.3905	-4.3883	-4.3883
-3.9959	-4.5017	-4.4868	-4.4862	-4.4843

* Analytical solution is obtained from Ref. [44].

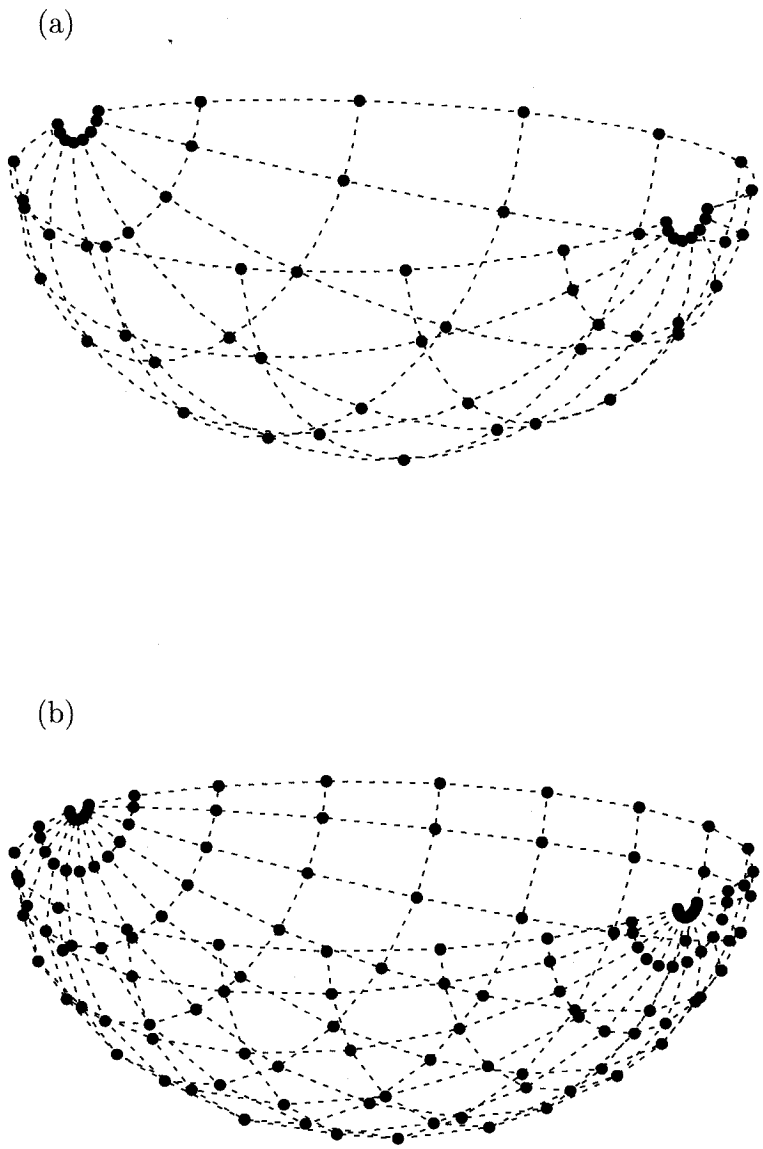

Figure 5.5: Gaussian points on the NURBS representation of a hemi-ellipsoid; (a): 8×8 points, (b): 10×10 points

5.2 Numerical Results for Unsteady Flow Potential

5.2.1 Radiation of a Floating Hemisphere

To investigate the accuracy of the proposed method, simulation studies were performed for the motion of a floating sphere with radius a. The discretized form of the integral equation for radiation problem of a floating sphere, Equation (4.79), can be written in the following matrix form for each mode of motions

$$[\mathcal{A}_{ij}]\{\phi_j\} = [\mathcal{B}_{ij}]\{\frac{\partial \phi}{\partial n_j}\} \tag{5.2}$$

where

$$\begin{cases} \mathcal{A}_{ij} = \left\{ -\frac{\mathbf{r}_{ij}\cdot\mathbf{n}_j}{r_{ij}^3} + \frac{\partial G_{ij}^*}{\partial n_j} \right\} \bar{w}_j & j \neq i \quad \text{and} \quad i,j = 1,...,N \\ \mathcal{A}_{ii} = 4\pi + \left\{ \sum_{j=1,j\neq i}^{N} \frac{\mathbf{r}_{ij}\cdot\mathbf{n}_j}{r_{ij}^3} + \frac{\partial G_{ij}^*}{\partial n_j} \right\} \bar{w}_j \end{cases}$$

and

$$\begin{cases} \mathcal{B}_{ij} = \left\{ -\frac{1}{r_{ij}} + G_{ij}^* \right\} \bar{w}_j & j \neq i \quad \text{and} \quad i,j = 1,...,N \\ \mathcal{B}_{ii} = G_{ii}^* \bar{w}_i - \frac{\phi_e}{\sigma_i} + \sum_{j=1,j\neq i}^{N} \frac{1}{r_{ij}} \frac{\sigma_j}{\sigma_i} \bar{w}_j \end{cases}$$

These complex system of linear integral equations are solved by using a complex matrix inversion subroutine inversion LAPACK. Tables 5.2 through 5.5 display the added-mass and damping coefficients, respectively, for various wave number, ν for both

surge and heave motions. Computations using the panel method are performed by dividing the body surface into 1024 triangular panels. Simulation studies are performed to compute the added-mass and damping coefficients of a hemisphere with desingularized method for different number of collocation points. The results are compared with the analytical results of Hulme [20]. Non-dimensional added-mass μ_{ii} and damping λ_{ii} coefficients for surge ($i = 1$) and heave ($i = 3$) are defined as

$$\mu_{ii} = \frac{\bar{A}_{ii}}{\rho \nabla}, \qquad \lambda_{ii} = \frac{\bar{B}_{ii}}{\rho \nabla \sqrt{g/L}} \tag{5.3}$$

where ∇ stands for volume of the fluid displaced by the body. The total execution time for the panel method with 1024 panels was 1469.73 seconds. The total execution time for desingularized method are 4.25 seconds for 8×8 collocation points distributed on the body surface and 20.74 and 69.33 seconds for 12×12 and 16×16 collocation points, respectively.

Comparison of the results for surge and heave added-mass and damping coefficients show that the numerical results agree with the analytical results of Hulme [20]. For 16×16 points, the difference occurs at most in the fourth decimal point. For 12×12 and 8×8, points the differences also occur at some third decimal points. The results obtained by desingularized method with 16×16 points are more accurate than the results of panel method for many wave numbers while its required executing time is approximately $\frac{1}{20}$ executing time of the panel method. However, it is indicated that the desingularized method with a few number of collocation points gives satisfactory

results, in terms of accuracy.

Table 5.2: Surge added-mass for a floating hemisphere

			Present method		
νa	Hulme	P.M.(1024)*	8×8	12×12	16×16
0.0	0.5000	0.4971	0.5019	0.5006	0.5002
0.1	0.5223	0.5192	0.5242	0.5229	0.5226
0.2	0.5515	0.5481	0.5534	0.5521	0.5518
0.3	0.5848	0.5811	0.5867	0.5854	0.5851
0.4	0.6175	0.6135	0.6194	0.6181	0.6178
0.5	0.6439	0.6397	0.6458	0.6445	0.6442
0.6	0.6586	0.6546	0.6605	0.6592	0.6589
0.7	0.6582	0.6544	0.6601	0.6588	0.6585
0.8	0.6421	0.6388	0.6441	0.6427	0.6424
0.9	0.6127	0.6098	0.6146	0.6133	0.6129
1.0	0.5740	0.5716	0.5759	0.5746	0.5742
1.2	0.4860	0.4844	0.4879	0.4866	0.4862
1.4	0.4038	0.4026	0.4056	0.4043	0.4040
1.6	0.3371	0.3361	0.3390	0.3377	0.3373
1.8	0.2865	0.2856	0.2883	0.2871	0.2868
2.0	0.2493	0.2484	0.2510	0.2498	0.2495
2.5	0.1951	0.1940	0.1966	0.1955	0.1953
3.0	0.1720	0.1706	0.1731	0.1723	0.1721
3.5	0.1634	0.1610	0.1630	0.1633	0.1634
4.0	0.1620	0.1717	0.1795	0.1674	0.1643
4.5	0.1641	0.1643	0.1690	0.1655	0.1647
5.0	0.1679	0.1674	0.1720	0.1690	0.1684
6.0	0.1772	0.1757	0.1810	0.1781	0.1775
7.0	0.1865	0.1749	0.1640	0.1815	0.1844
8.0	0.1949	0.1948	0.2012	0.1965	0.1955
9.0	0.2022	0.2010	0.2110	0.2037	0.2027
10.0	0.2085	0.2042	0.2220	0.2090	0.2085

* Panel method with 1024 panels.

Table 5.3: Surge damping coefficients for a floating hemisphere

			Present method		
νa	Hulme	P.M.(1024)	8×8	12×12	16×16
0.0	0.0000	0.0000	0.0000	0.0000	0.0000
0.1	0.0011	0.0011	0.0011	0.0011	0.0011
0.2	0.0082	0.0080	0.0082	0.0082	0.0082
0.3	0.0255	0.0252	0.0255	0.0255	0.0255
0.4	0.0557	0.0549	0.0557	0.0557	0.0557
0.5	0.0987	0.0974	0.0986	0.0987	0.0987
0.6	0.1516	0.1497	0.1515	0.1515	0.1516
0.7	0.2092	0.2068	0.2091	0.2092	0.2092
0.8	0.2653	0.2625	0.2652	0.2653	0.2653
0.9	0.3145	0.3116	0.3145	0.3145	0.3145
1.0	0.3535	0.3505	0.3534	0.3535	0.3535
1.2	0.3978	0.3950	0.3977	0.3978	0.3978
1.4	0.4061	0.4037	0.4059	0.4060	0.4061
1.6	0.3929	0.3909	0.3926	0.3928	0.3929
1.8	0.3695	0.3678	0.3691	0.3693	0.3694
2.0	0.3424	0.3410	0.3418	0.3422	0.3423
2.5	0.2769	0.2759	0.2757	0.2765	0.2767
3.0	0.2237	0.2230	0.2212	0.2229	0.2233
3.5	0.1826	0.1825	0.1764	0.1808	0.1818
4.0	0.1511	0.1459	0.1844	0.1608	0.1552
4.5	0.1266	0.1256	0.1306	0.1277	0.1271
5.0	0.1073	0.1066	0.1084	0.1076	0.1074
6.0	0.0794	0.0788	0.0763	0.0786	0.0791
7.0	0.0608	0.0569	-0.0365	0.0367	0.0509
8.0	0.0479	0.0476	0.0539	0.0489	0.0483
9.0	0.0386	0.0380	0.0396	0.0377	0.0382
10.0	0.0317	0.0292	-0.0165	0.0209	0.0276

Table 5.4: Heave added-mass for a floating hemisphere

			Present method		
νa	Hulme	P.M.(1024)	8×8	12×12	16×16
0.0	0.8310	0.8248	0.8314	0.8311	0.8310
0.1	0.8627	0.8565	0.8632	0.8629	0.8628
0.2	0.7938	0.7885	0.7943	0.7940	0.7939
0.3	0.7157	0.7112	0.7161	0.7158	0.7157
0.4	0.6452	0.6414	0.6457	0.6453	0.6452
0.5	0.5861	0.5828	0.5865	0.5862	0.5861
0.6	0.5381	0.5352	0.5386	0.5382	0.5382
0.7	0.4999	0.4972	0.5003	0.5000	0.4999
0.8	0.4698	0.4673	0.4702	0.4699	0.4698
0.9	0.4464	0.4441	0.4469	0.4465	0.4465
1.0	0.4284	0.4261	0.4289	0.4286	0.4285
1.2	0.4047	0.4025	0.4052	0.4048	0.4048
1.4	0.3924	0.3900	0.3928	0.3925	0.3924
1.6	0.3871	0.3847	0.3875	0.3872	0.3872
1.8	0.3864	0.3838	0.3868	0.3865	0.3864
2.0	0.3884	0.3856	0.3887	0.3885	0.3884
2.5	0.3988	0.3941	0.3987	0.3988	0.3988
3.0	0.4111	0.4085	0.4115	0.4112	0.4111
4.0	0.4322	0.4291	0.4325	0.4323	0.4322
5.0	0.4471	0.4438	0.4474	0.4472	0.4471
6.0	0.4574	0.4543	0.4578	0.4575	0.4574
7.0	0.4647	0.4614	0.4651	0.4648	0.4647
8.0	0.4700	0.4666	0.4705	0.4701	0.4700
9.0	0.4740	0.4709	0.4741	0.4741	0.4740
10.0	0.4771	0.4738	0.4775	0.4772	0.4771

Table 5.5: Heave damping coefficients for a floating hemisphere

			Present method		
νa	Hulme	P.M.(1024)	8×8	12×12	16×16
0.0	0.0000	0.0000	0.0000	0.0000	0.0000
0.1	0.1816	0.1797	0.1816	0.1816	0.1816
0.2	0.2793	0.2766	0.2793	0.2793	0.2793
0.3	0.3254	0.3224	0.3254	0.3254	0.3254
0.4	0.3410	0.3381	0.3410	0.3410	0.3410
0.5	0.3391	0.3363	0.3391	0.3391	0.3391
0.6	0.3271	0.3247	0.3271	0.3271	0.3271
0.7	0.3098	0.3076	0.3098	0.3098	0.3098
0.8	0.2899	0.2880	0.2899	0.2899	0.2899
0.9	0.2691	0.2674	0.2691	0.2691	0.2691
1.0	0.2484	0.2470	0.2485	0.2484	0.2484
1.2	0.2096	0.2085	0.2096	0.2096	0.2096
1.4	0.1756	0.1749	0.1757	0.1756	0.1756
1.6	0.1469	0.1463	0.1469	0.1469	0.1469
1.8	0.1229	0.1225	0.1229	0.1229	0.1229
2.0	0.1031	0.1027	0.1031	0.1031	0.1031
2.5	0.0674	0.0656	0.0665	0.0671	0.0673
3.0	0.0452	0.0456	0.0453	0.0452	0.0452
4.0	0.0219	0.0222	0.0219	0.0219	0.0219
5.0	0.0116	0.0118	0.0114	0.0116	0.0116
6.0	0.0066	0.0068	0.0070	0.0067	0.0066
7.0	0.0040	0.0041	0.0041	0.0040	0.0040
8.0	0.0026	0.0026	0.0023	0.0025	0.0025
9.0	0.0017	0.0019	0.0025	0.0018	0.0017
10.0	0.0012	0.0012	0.0014	0.0012	0.0012

5.2.2 Irregular Frequencies

In the numerical simulation of boundary integral equations, spurious solutions emerged for a certain range of wave numbers. These solutions exhibit very sharp peaks in the solution and are considered to be a phenomenal. The frequencies in which these spurious solutions appear are known to be irregular frequencies. Significant errors appear near the irregular frequencies in the numerical solution of the boundary integral equation. Several methods have been proposed by the researchers to remove the irregular frequencies. However, the removal of irregular frequencies is beyond the scope of this study.

By linear composition of the potential formulation and its derivative, the modified integral equation can be obtained. Lee and Sclavounos [37] adopted this method to wave-body interaction problems and demonstrated that the irregular frequencies can be removed from potential flow computation for three-dimensional problems. This method was also adopted by Yang [77] and the effectiveness of the method was demonstrated by proper composition of the integral equations. Zhu [79] removed the irregular frequencies for the bodies with two plane of symmetry by adding wave sources or dipoles on the interior free surface to the free surface Green's function.

Figures 5.6 and 5.7 display the added-mass and damping coefficients for a floating hemisphere, respectively. It is shown that the effect of the irregularity near the irregular frequency can be considerably decreased by increasing the number of collocation points on the body surface.

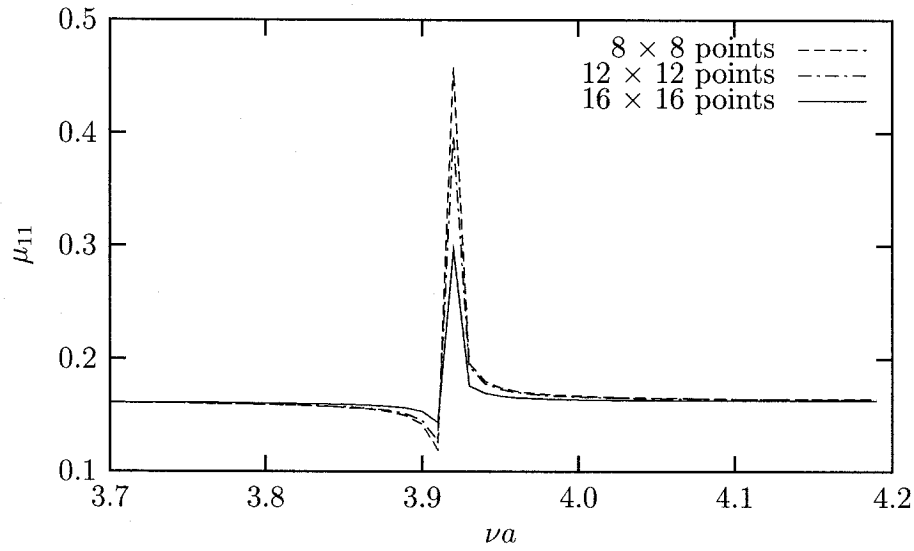

Figure 5.6: Surge added-mass coefficients of a floating hemisphere near the first irregular frequency

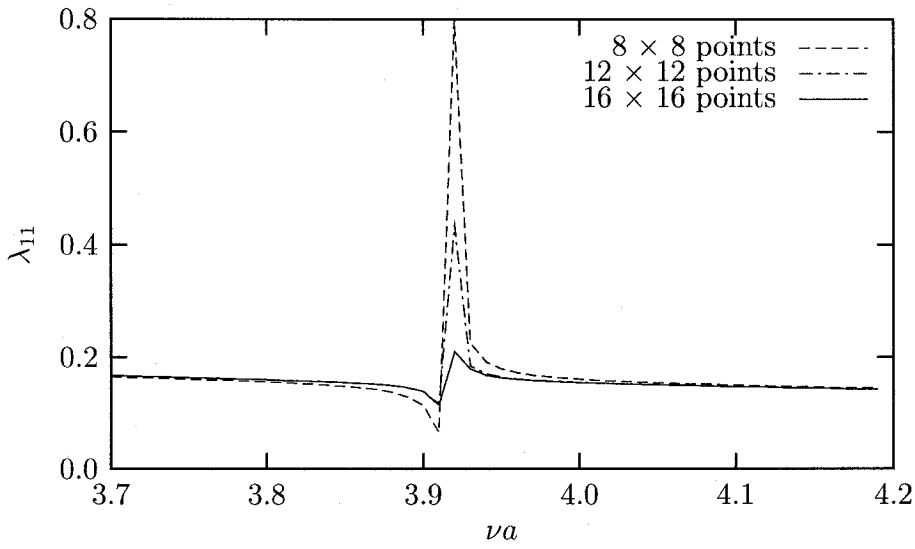

Figure 5.7: Surge damping coefficients of a floating hemisphere near the first irregular frequency

5.2.3 Diffraction of a Submerged Spheroid

The discretized form of the integral equation for diffraction problem, Equation (4.81) can be written in the following form

$$[\mathcal{A}_{ij}]\{\phi_j\} = \mathcal{C}_i \tag{5.4}$$

where $\mathcal{A}_{ij}$ is the same matrix, as defined in Equation (5.2) and $\mathcal{C}_i = 4\pi\,\phi_{Ii}$. The motions of a spheroid with semi axis of $a = 6$ and $b = 1$ in x and y directions, respectively, are computed. The spheroid is submerged in a water of infinite depth. The computation is performed for three different submergence cases. The study of submerged body is important on hydrodynamic computation of submerged structure and submarines. The surface of the ellipsoid is generated by two methods. In the first method, Method I, the NURBS surface is obtained by revolution of a curve about x-axis. This method gives a very accurate surface. In the second method, Method II, the surface is generated using a table of offsets for the ellipsoid. The table of offsets is obtained from mathematical description of the ellipsoid. Since the ship body cannot be dealt as the ruled surface, Method II is more practical in ship hydrodynamic computations. Real and imaginary parts of surge exciting force on a submerged spheroid in regular waves with the depth of submergence $h = 2$ are given in Tables 5.6 and 5.7. The numerical solutions are obtained for four different cases. In Method I, the body surface is generated by rotating a curve and 512 collocation points, 16 points in u and 32 points in v direction, are distributed on the surface. For Method II, in which the body surface is

generated using table of offsets of the spheroid different number of collocation points, namely, 512, 288 and 128 are distributed on the body surface. The real and imaginary parts of the surge exciting force for different values of νa in Method I are the same as the analytical solutions given by Wu and Taylor [73] for four decimal digits when $\nu a \leq 1$. For $\nu a > 1$, the accuracy of numerical solutions comparing to the analytical one are up to three decimal digits. When NURBS description of the body surface is obtained from the table of offsets the accuracy of the numerical solutions is less than those computed in Method I.

Tables 5.8 and 5.9 show the convergence of heave forces for different numbers of collocation points. Again the results show good agreement with the analytical solutions. However, the results obtained by Method I are more accurate than those of Method II.

Several other cases for different submergence and aspect ratios are investigated and the results are given in Figures D.1-D.4. This figures indicate that in general, the non-dimensional forces are reduced by increasing the submergence, for νa approximately less than 4.5. It is also indicated that for a given length of minor axis, by increasing the length of the major axis, the non-dimensional forces coefficients are reduced for a certain value of νa, but for νa greater than a certain value, the non-dimensional forces are increased.

More results for added-mass and damping coefficients of the spheroid with different aspect ratios submerging in various depth of water are given in Appendix D. The comparisons are also given for the present computations and the panel method computations.

Table 5.6: Real part of surge exciting force [-$\Re(f_x)$] on a submerged spheroid in regular waves(h=$2b$, a=6b)

		Method I	Method II		
νa	Wu &Taylor	16 × 32*	16 × 32	12 × 24	8 × 16
0.1	0.0000	0.0000	0.0000	0.0000	0.0000
0.2	0.0002	0.0002	0.0002	0.0002	0.0002
0.3	0.0007	0.0007	0.0007	0.0007	0.0007
0.4	0.0017	0.0016	0.0016	0.0016	0.0016
0.5	0.0031	0.0032	0.0031	0.0031	0.0029
0.6	0.0051	0.0051	0.0051	0.0051	0.0048
0.7	0.0077	0.0077	0.0077	0.0077	0.0073
0.8	0.0110	0.0110	0.0111	0.0111	0.0105
0.9	0.0151	0.0151	0.0151	0.0151	0.0144
1.0	0.0198	0.0198	0.0199	0.0199	0.0190
2.0	0.0903	0.0904	0.0910	0.0910	0.0896
3.0	0.1045	0.1046	0.1053	0.1053	0.1058
4.0	0.0486	0.0488	0.0490	0.0490	0.0507
5.0	0.0010	0.0010	0.0010	0.0010	0.0028

* Number of Gaussian points on the body surface

Table 5.7: Imaginary part of surge exciting force [-$\Im(f_x)$] on a submerged spheroid in regular waves(h=$2b$, a=6b)

		Method I	Method II		
νa	Wu &Taylor	$16 \times 32^*$	16×32	12×24	8×16
0.1	1.0542	1.0542	1.0532	1.0532	1.0196
0.2	1.0536	1.0536	1.0526	1.0526	1.0191
0.3	1.0514	1.0514	1.0504	1.0504	1.0171
0.4	1.0475	1.0475	1.0466	1.0466	1.0136
0.5	1.0420	1.0420	1.0411	1.0411	1.0086
0.6	1.0348	1.0348	1.0339	1.0339	1.0020
0.7	1.0258	1.0258	1.0250	1.0249	0.9937
0.8	1.0151	1.0150	1.0142	1.0142	0.9838
0.9	1.0022	1.0022	1.0015	1.0015	0.9720
1.0	0.9875	0.9876	0.9869	0.9869	0.9585
2.0	0.7267	0.7267	0.7265	0.7265	0.7138
3.0	0.3367	0.3366	0.3361	0.3361	0.3384
4.0	0.0356	0.0357	0.0353	0.0354	0.0447
5.0	-0.0995	-0.0995	-0.0997	-0.0996	-0.0926

Table 5.8: Real part of heave exciting force [$\Re(f_z)$] on a submerged spheroid in regular waves(h=2b, a=6b)

		Method I	Method II		
νa	Wu &Taylor	$16 \times 32^*$	16×32	12×24	8×16
0.1	2.0256	2.0285	2.0524	2.0503	2.0846
0.2	2.0344	2.0374	2.0614	2.0593	2.0887
0.3	2.0416	2.0446	2.0688	2.0668	2.0950
0.4	2.0466	2.0497	2.0741	2.0720	2.1001
0.5	2.0487	2.0518	2.0764	2.0743	2.1027
0.6	2.0471	2.0502	2.0750	2.0729	2.1017
0.7	2.0408	2.0439	2.0689	2.0667	2.0962
0.8	2.0301	2.0324	2.0573	2.0552	2.0851
0.9	2.0116	2.0146	2.0395	2.0373	2.0678
1.0	1.9871	1.9902	2.0148	2.0126	2.0435
2.0	1.3913	1.3933	1.4086	1.4072	1.4355
3.0	0.6034	0.6039	0.6086	0.6082	0.6301
4.0	0.0453	0.0457	0.0444	0.0445	0.0541
5.0	-0.1904	-0.1909	-0.1938	-0.1935	-0.1976

Table 5.9: Image part of heave exciting force [-$\Im(f_z)$] on a submerged spheroid in regular waves(h=$2b$, a=6b)

		Method I	Method II		
νa	Wu &Taylor	$16 \times 32^*$	16×32	12×24	8×16
0.1	0.0002	0.0002	0.0002	0.0002	0.0002
0.2	0.0017	0.0017	0.0017	0.0017	0.0018
0.3	0.0054	0.0054	0.0055	0.0055	0.0057
0.4	0.0121	0.0121	0.0124	0.0124	0.0128
0.5	0.0222	0.0223	0.0228	0.0228	0.0236
0.6	0.0361	0.0362	0.0371	0.0370	0.0383
0.7	0.0538	0.0540	0.0553	0.0552	0.0572
0.8	0.0752	0.0753	0.0772	0.0770	0.0797
0.9	0.0995	0.0998	0.1023	0.1020	0.1057
1.0	0.1265	0.1268	0.1299	0.1297	0.1343
2.0	0.3553	0.3563	0.3642	0.3634	0.3747
3.0	0.3043	0.3051	0.3108	0.3101	0.3202
4.0	0.1397	0.1405	0.1427	0.1424	0.1494
5.0	0.0139	0.0138	0.0138	0.0138	0.0156

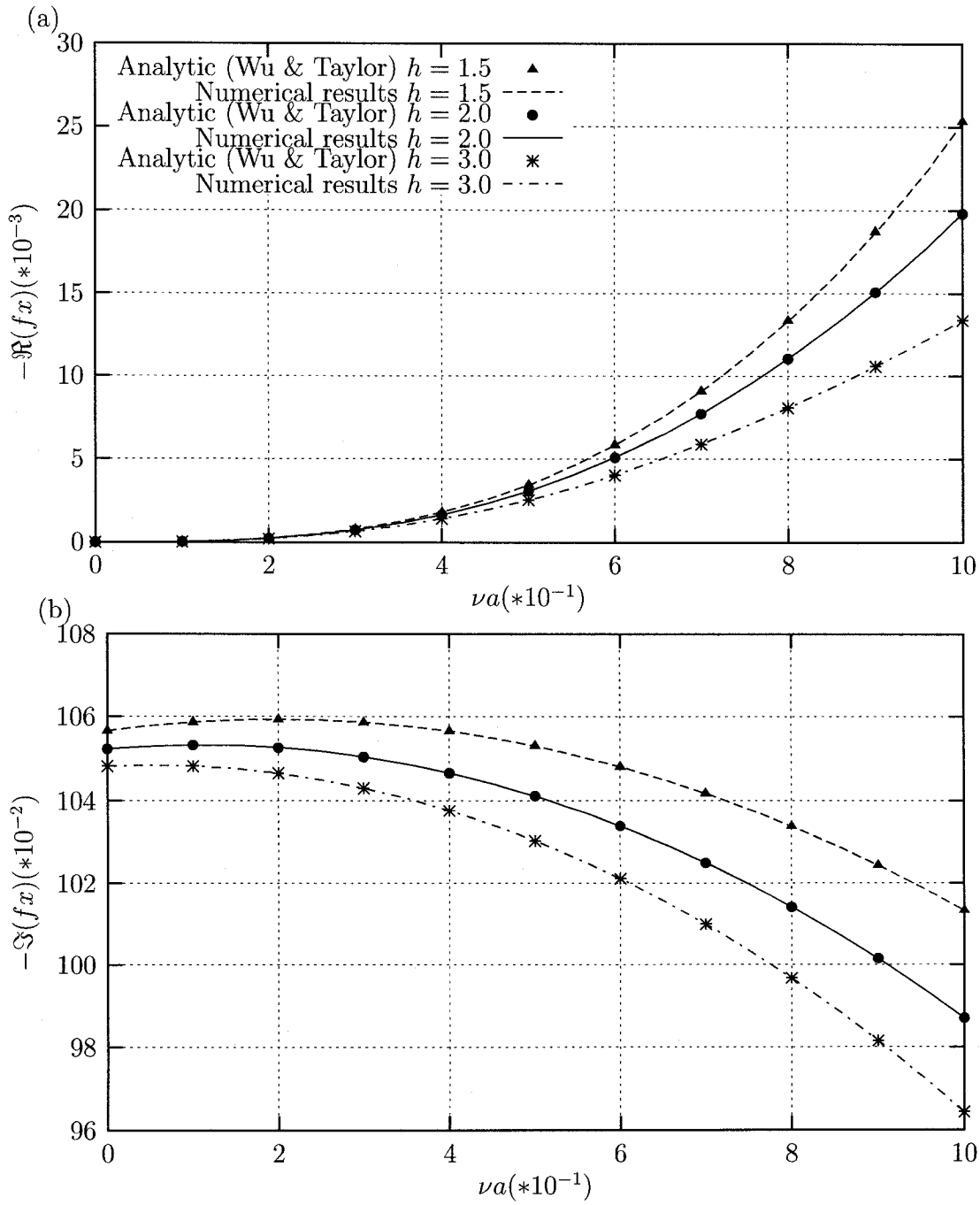

Figure 5.8: Non-dimensional surge force on a spheroid ($a = 6b$) at different submergence; (a) Real part, (b) Imaginary part.

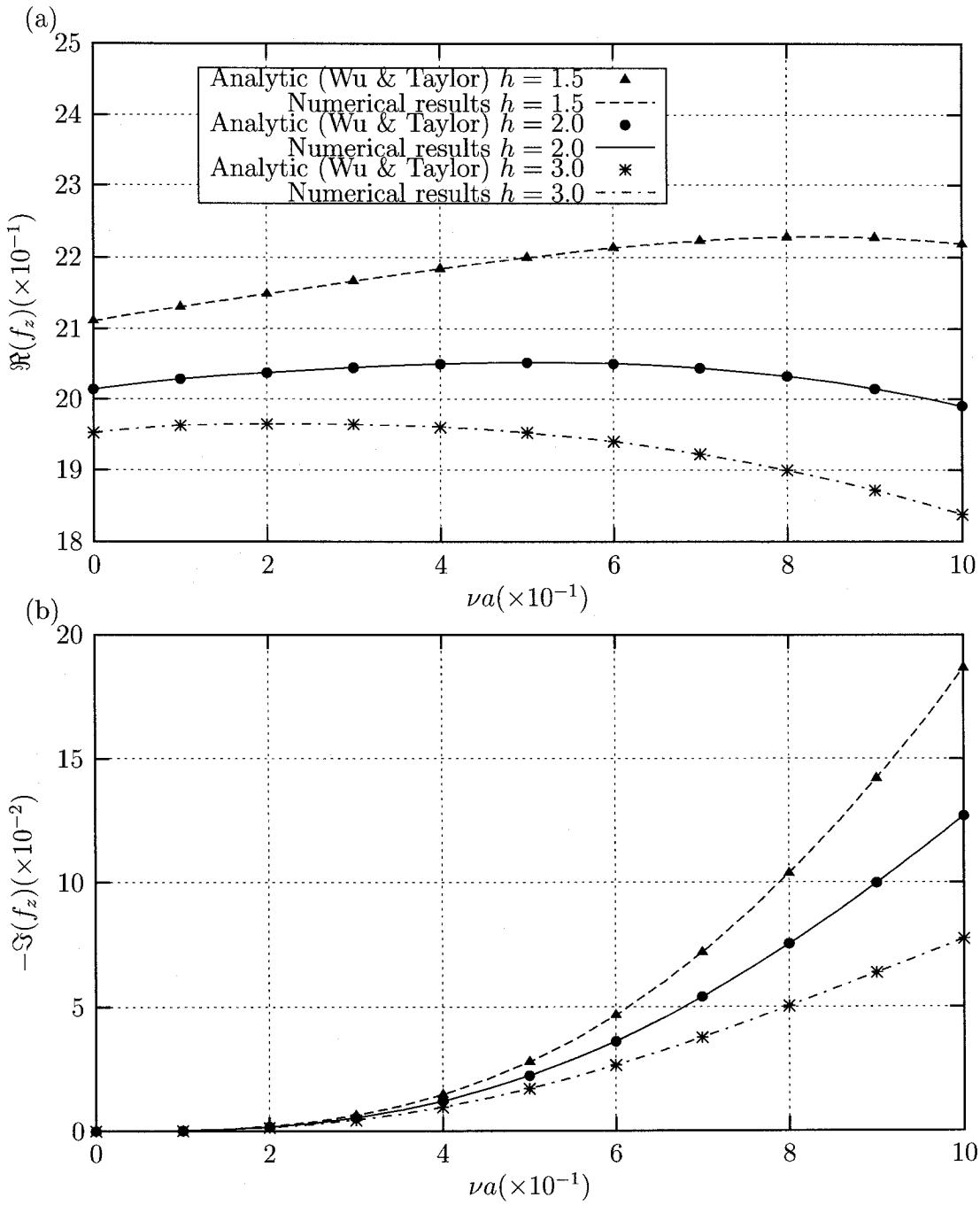

Figure 5.9: Non-dimensional heave force on a spheroid ($a = 6b$) at different submergence; (a) Real part, (b) Imaginary part.

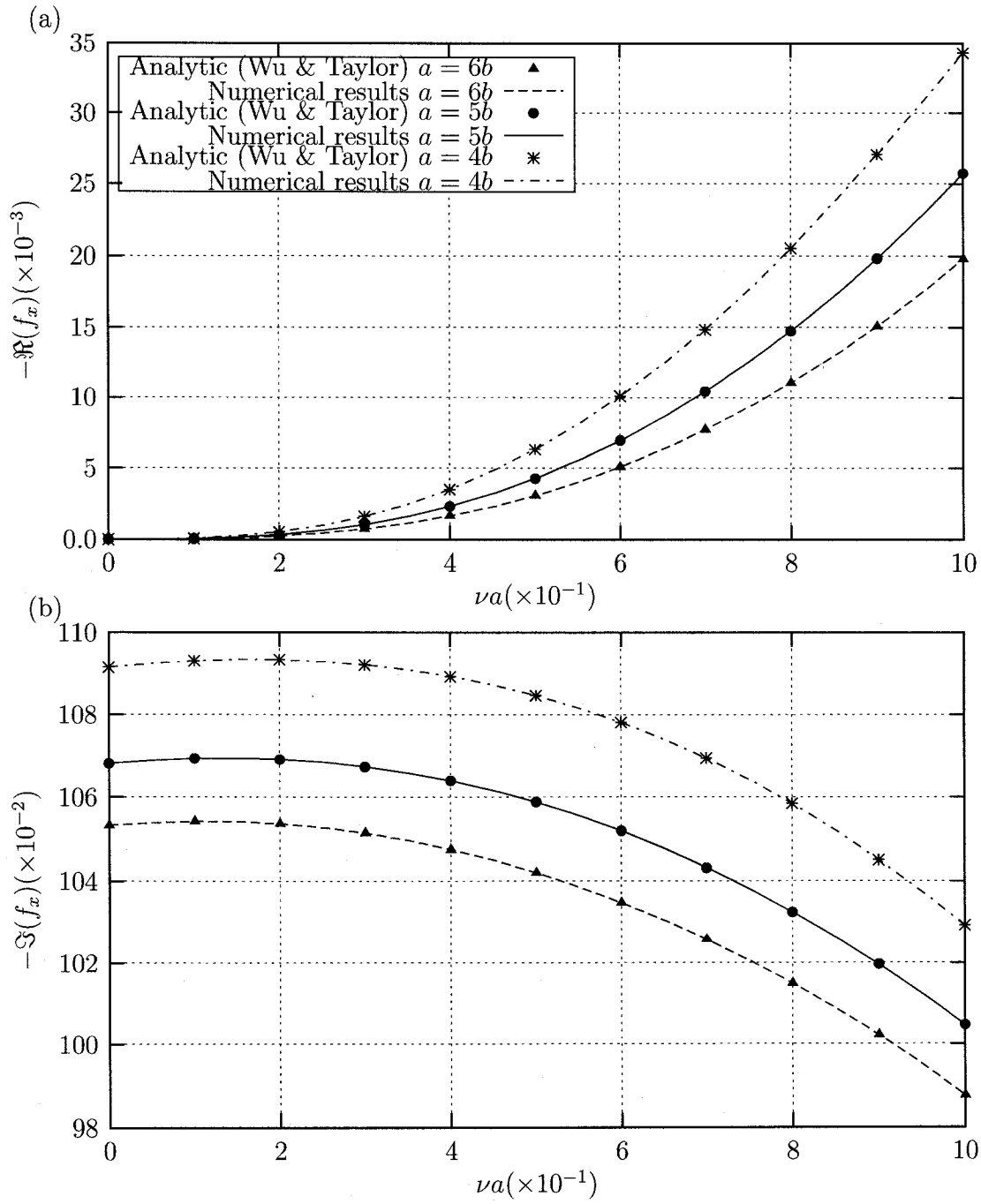

Figure 5.10: Non-dimensional surge force on spheroids of different aspect ratio a/b and $h = 2b$; (a) Real part, (b) Imaginary part.

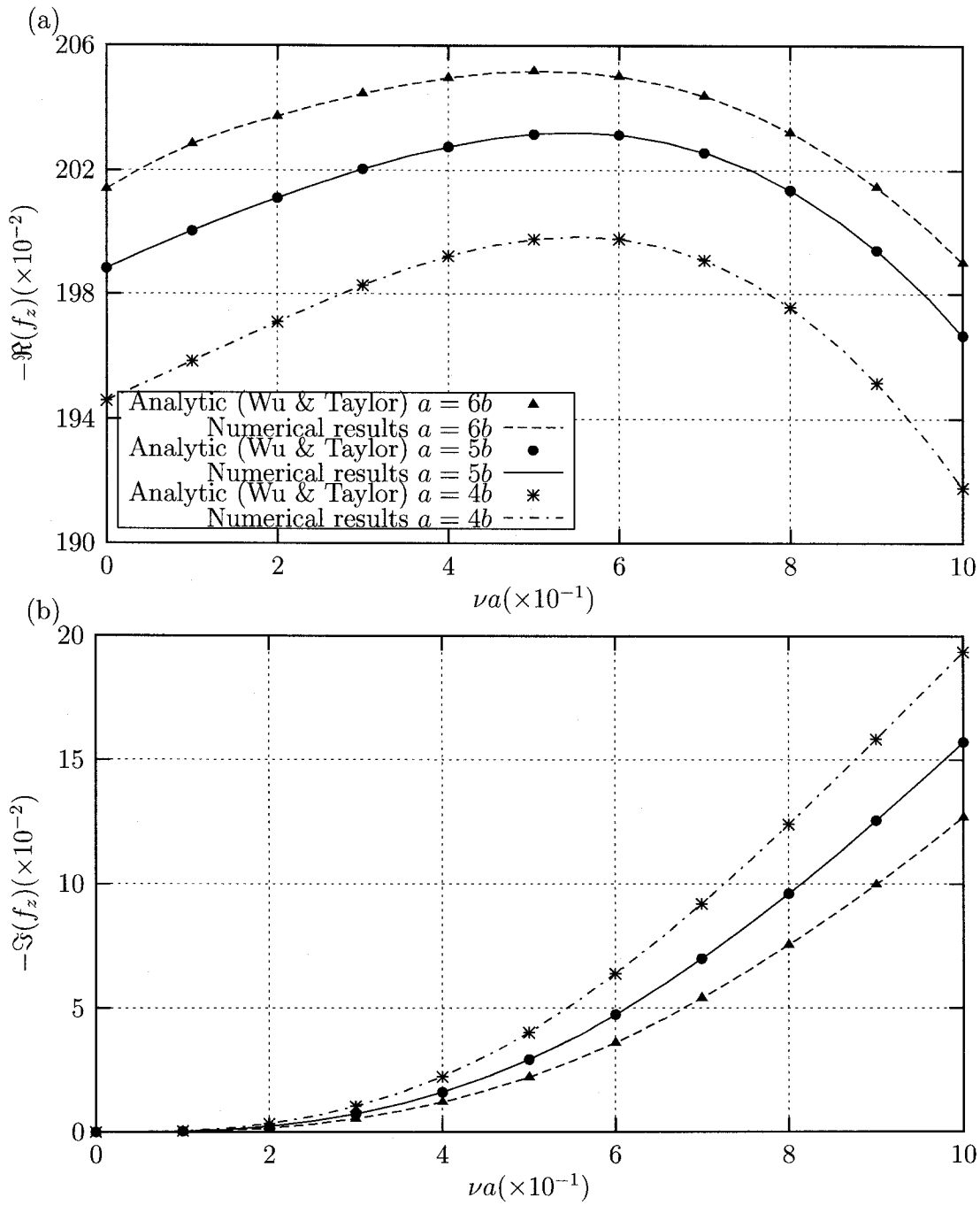

Figure 5.11: Non-dimensional heave force on spheroids of different aspect ratio a/b and $h = 2b$; (a) Real part, (b) Imaginary part.

5.2.4 Comparing Run Times and Relative Error

The comparison of various computational efforts and relative errors is presented in Table 5.10. The comparison is made for added-mass and damping coefficients of an spheroid with semi axis $a = 6$ and $b = 1$ submerging at depth $h = 3$. Computations are performed using panel methods and the desingularized method presented in this study. The results, shown in Table 5.10, are computed for the frequency $\nu a = 0.2$.

For the panel method computation, the body is panelized by triangular panels and the collocation points are chosen to be located on the center of each panel. Three cases corresponding to three different number of panels, namely, 128, 256 and 512 panels are compared with three cases with the same number of Gaussian points. In the desingularized method, the same number of collocation points as for panel methods are distributed on the body surface. The Gaussian points are obtained using Legendre polynomials. The order of Gaussian points are chosen to be $16 \times 8, 16 \times 16$ and 16×32 for three cases, respectively.

Table 5.10 shows that the required execution time [1] of computation with the present method is approximately 70% of that of the panel method when the number of Gaussian points are equal to the number of panels. However, for the same numbers, the relative errors, RE, for the added-mass and damping coefficients computed by present method are much less that those of the panel method. It is indicated that the relative error of added-mass for the case of 128 Gaussian points is 1.07%, which is less than half of the

[1]The CPU time of execution on computer Pentium4, 2.4GHz, 512MB

the relative error of added-mass computed by the panel method with 512 panels. The relative error of damping coefficient obtained by present method with 128 Gaussian points is less than half of the relative error computed by the panel method with 512 panels.

It is also indicated that in the present desingularized method, the increase of number of Gaussian points beyond certain number of points does not necessarily increase the accuracy of computation. This may be due to the distances between two successive points, r_{pq}, appearing in the formulation. In the numerical simulation, the minimum values of r_{pq} for the case of 16×8 and 16×16 and Gaussian points are greater than 0.008 and 0.002, respectively, while for the case of 16×32 Gaussian points, it is less than 0.001. It is believed that in order to obtain accurate results such a number of Gaussian points or arrangement of the distribution of points is needed to have appropriate value for minimum distance of two successive points. From different numerical experiments, the minimum value of r_{pq} is found to be greater than 0.001.

Table 5.10: Comparison of run times and relative error (RE) for added-mass and damping coefficients of an submerged ellipsoid ($a = 6., b = 1., h = 3.$)

	Nomber of points or panels	CPU time [seconds]	RE of Added-mass	RE of Damping Coef.
Panel method	128	1.39	9.3%	19.9 %
Present method	16×8	0.9	1.07 %	2.28%
Panel method	256	4.91	3.45 %	8.4 %
Present method	16×16	3.69	0.53 %	0.77%
Panel method	512	19.87	2.86 %	6.4 %
Present method	16×32	15.3	0.63 %	0.81%

5.2.5 Significance of Element Surface

The element surface is defined by the area of each panel in the panel method or the area surrounding each point in the desingularized method. Since the surface area of each element appears in the integral equations, the accuracy of the element surface significantly influences on the numerical computation of the integral equations.

Table 5.11 shows the relative errors of surface of the spheroid for different cases. When the surface is panelized by 64 triangular panels, the relative error of surface area is 17.75%. By increasing the number of panels, the error decreases and more accurate results from computations can be anticipated. When the Gaussian points are distributed on the surface using Legendre polynomials or Chebyshev polynomials, and the surface is computed by summation of the weighting factors of these polynomials, the relative errors for surface area are much less than those of panelized surface. However, the Legendre polynomial gives more accurate results for surface elements than Chebyshev polynomials as indicated in Table 5.11. Thus, throughout of this study the sources are distribution on the body surface using Legendre polynomials.

5.3 Numerical Results for Ship Motion in Water Waves

Figures 5.12 and 5.13 are the comparisons of added-mass and damping coefficients for a Wigley model for different Froude number. The main dimensions of the Wigley model are given in Table 5.12. This model is the same as the model that was used by Journee [24]. The 3D-WAMIT results shown in the figures are the three-dimensional

Table 5.11: Comparison of area surface of an ellipsoid ($a = 6., b = 1.$)

	Nomber of points or panels	Relative error
Panel method	64	17.75%
Legendre	8×8	0.67%
Chebyshev	8×8	2.53%
Panel method	128	6.99%
Legendre	8×16	0.03%
Chebyshev	8×16	2.51%
Panel method	192	3.91%
Legendre	12×16	0.003%
Chebyshev	12×16	2.48%
Panel method	256	3.53%
Legendre	16×16	0.003%
Chebyshev	16×16	2.46%
Panel method	576	1.74%
Legendre	24×24	0.0001%
Chebyshev	24×24	2.41%

numerical solution based on the WAMIT computer program, developed at the Massachusetts Institute of Technology and the strip theory results are obtained from the computer program developed at Delft University of Technology based on the strip theory. The experimental measurements were carried out on the Ship Hydrodynamics Laboratory, Delft University of Technology. The 3D-WAMIT, strip theory and experimental data are taken from Reference [24]. It is shown that reasonable agreement with experimental data can be obtained by the desingularized method for various frequency of encounter. The main particulars of the Wigley model and the Container ship are given in Table 5.12 and Table 5.13, respectively.

Table 5.12: The main particulars of the Wigley model (from Ref. [24])

Amidship section coefficients, C_m (-)	0.6667
Length to breadth ratio, L/B (-)	10
Length, L (m)	3.0000
Breadth, B (m)	0.3000
Draught, d (m)	0.1875
Trim, t (m)	0.0000
Volume of displacement, ∇ (m^3)	0.0780
Center of rotation above base, $\overline{KR}$ (m)	0.1875
Center of gravity above base, $\overline{KG}$ (m)	0.1700
Radius of inertia for pitch, k_{yy} (m)	0.7500

Table 5.13: The main particulars of the Container ship (from Ref. [7])

Length between perpendiculas, L (m)	270
Breadth, B (m)	32.2
Draught even keel, d (m)	10.85
Volume of displacement, ∇ (m^3)	560970
Block coefficient, C_B (-)	0.598
Waterplane coefficient, C_W (-)	0.757
Waterplane coefficient, C_M (-)	0.950
L. C. G. aft of station 10 $\overline{AG}$ (m)	10.12
Center of gravity above base, $\overline{KG}$ (m)	13.49
Metacentric height$\overline{GM}$ (m)	1.15
Radius of inertia for pitch, k_{yy} ($\%L_PP$)	24.8
Radius of inertia for roll, k_{xx} ($\%B$)	37.5
Natural roll period T_ϕ (second)	24.9
Natural pitch period T_θ (second)	8.6
Natural heave period T_z (second)	8.7

Here, the non-dimensional parameters for the ship motions are defined as follows:

For added-masses:

$$\mu_{ii} = \frac{\bar{A}_{ii}}{\rho \nabla} \qquad (i = 1, 2, 3)$$
$$\mu_{ii} = \frac{\bar{A}_{ii}}{\rho \nabla L^2} \qquad (i = 4, 5, 6)$$

For damping coefficients:

$$\lambda_{ii} = \frac{\bar{B}_{ii}}{\rho \nabla \sqrt{g/L}} \qquad (i = 1, 2, 3)$$
$$\lambda_{ii} = \frac{\bar{B}_{ii}}{\rho \nabla L^2 \sqrt{g/L}} \qquad (i = 4, 5, 6)$$

For ship motion:

$$\bar{\zeta}_i = \frac{|\zeta_i|}{\zeta} \qquad (i = 1, 2, 3)$$
$$\bar{\zeta}_i = \frac{|\zeta_i|}{\zeta \nu} \qquad (i = 4, 5, 6)$$

For wave exiting force:

$$\bar{F}_i = \frac{|F_{w_i}|}{\rho g \zeta L B} \qquad (i = 1, 2, 3)$$
$$\bar{F}_i = \frac{|F_{w_i}|}{\rho g \zeta L^2 B} \qquad (i = 4, 5, 6)$$

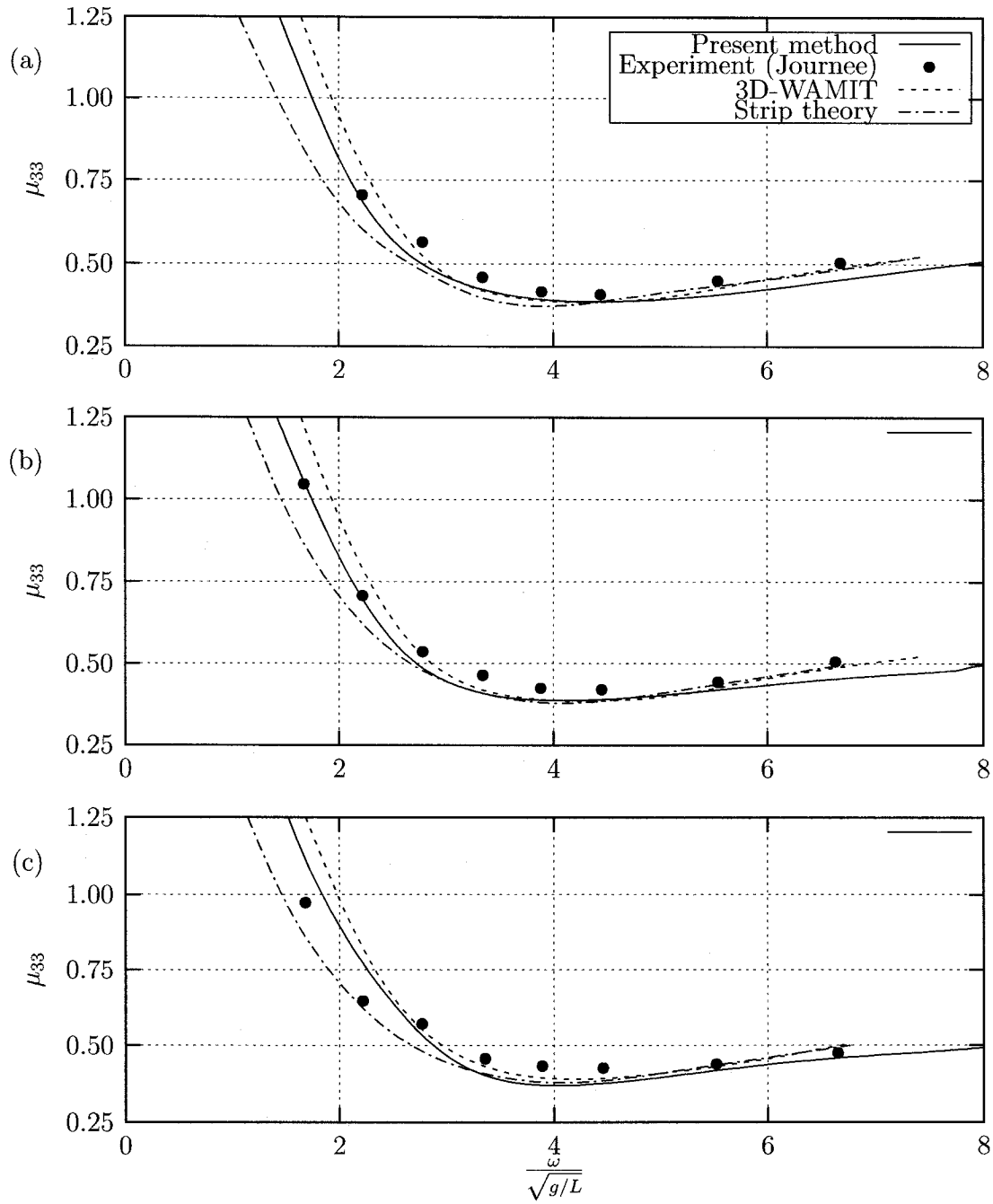

Figure 5.12: Comparisons of measured and calculated of added-mass coefficients for heave motions of a Wigley hull; (a): Fn=0.2, (b): Fn=0.3, (c): Fn=0.4.

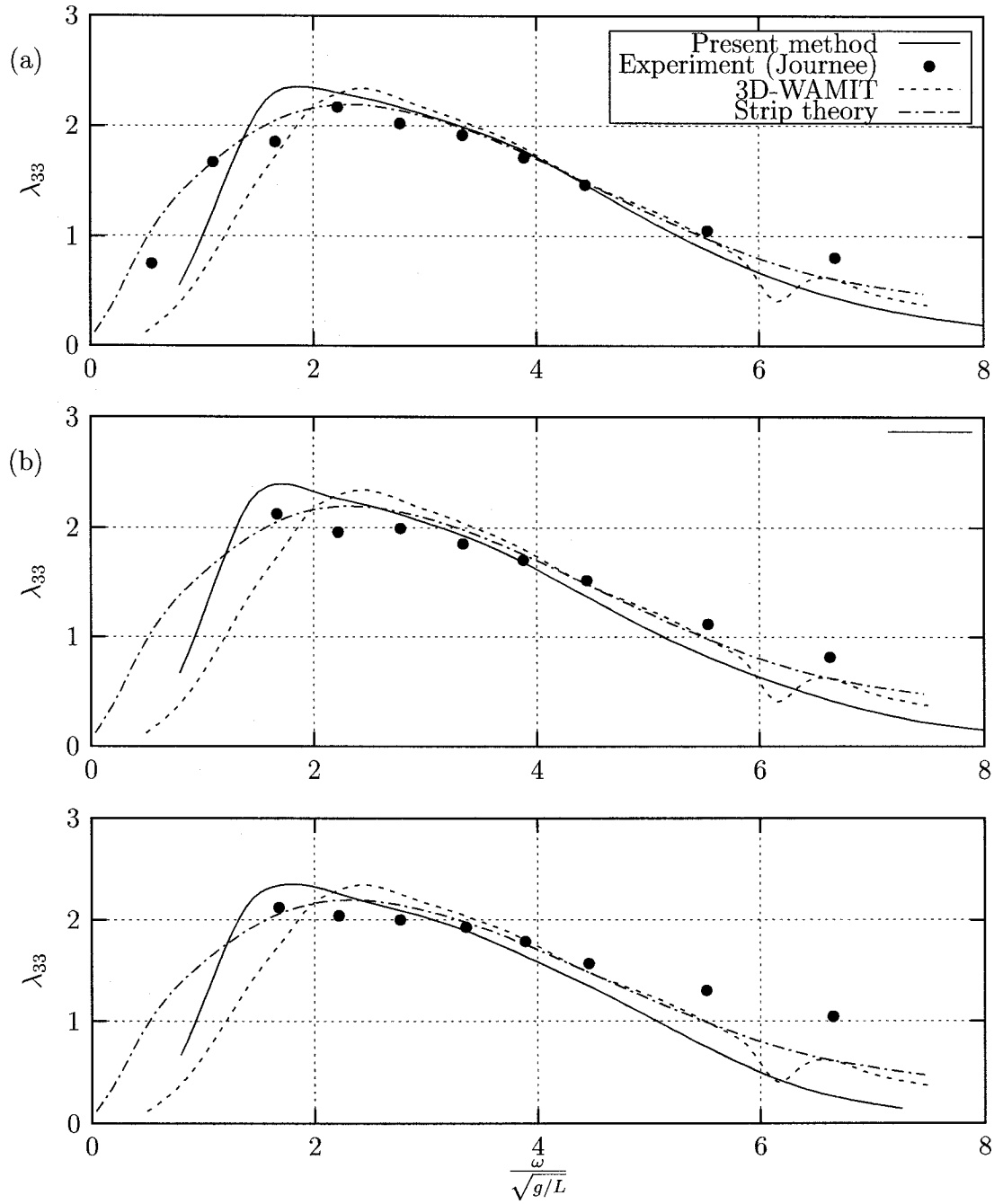

Figure 5.13: Comparisons of measured and calculated of damping coefficients for heave motions of a Wigley hull; (a): Fn=0.2, (b): Fn=0.3, (c): Fn=0.4.

Figure 5.14 is the heave motion of a container ship at various Froude numbers. The main particulars of the ship is given in Table 5.13. The experimental data and strip theory results are taken from Reference [7] and the panel method solutions are taken from Reference [19]. The same hull offsets are used in the strip theory and the panel method. For the heave motion, strip theory and present method have no significant difference in the short wave range. For the long wave range, both method over predict at all three Froude numbers. However, the present method gives results closer to the experimental data.

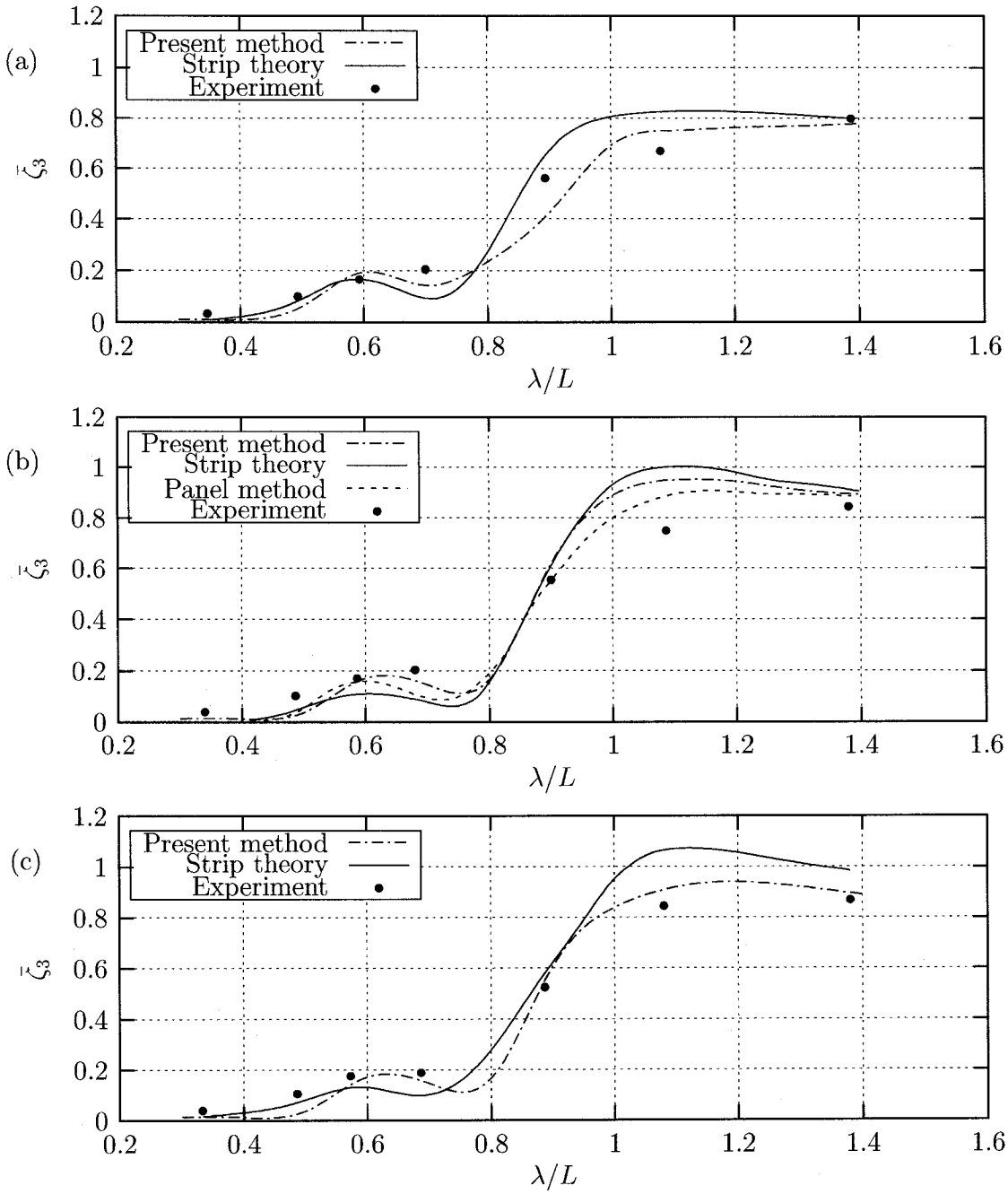

Figure 5.14: Heave motion for the container ship; $\beta = 180^0$, (a): Fn=0.220, (b): Fn=0.245, (c): Fn=0.270.

Figure 5.15 shows the non-dimensional added-mass coefficients for the container ship in head sea for three different Froude numbers. For a zero Froude number, the added-mass coefficients of motions, except for the roll motion, increase as the wave length to ship length ratio is incresed. At Froude number, $F_n = 0.15$, again the added-mass coefficients increases by increasing the wave length to ship length ratio. In high Froude number, $Fn = 0.30$, the added-mass coefficients increase with increasing the wave length to ship length ratio beyond certain value of this ratio (approximately 0.6). The non-dimensional added-mass coefficients for the motions of the container ship for $\beta = 150^0$ are also depicted in Figure 5.16. It is shown that for zero Froude number, the added-mass coefficients of motions increase as the wave length to ship length ratio is increased (except for roll motion). At Froude number, $F_n = 0.15$, for the wave length to ship length ratio greater than 0.5, the added mass coefficients increase as the wave length to ship length ratio is increased.

Figure 5.17 and Figure 5.18 show the non-dimensional damping coefficients of the container ship in head sea and $\beta = 150^0$, respectively. For both headings, the damping coefficients of surge and pitch motions in the case of zero Froude number decreases when the wave length to ship length ratio is approximately greater than 0.8. This is not occur for the cases with $F_n = 0.15$ or $F_n = 0.30$. In the heave motion, the damping coefficients for all three cases, in general, increased with increasing wave length to ship length ratio. The non-dimensional damping coefficients of roll motion for some wave length to ship length ratios in head seas are found to be approximately 0.001, (Figure 5.17). However, for a symmetrical body, these coefficients should theoretically

be equal to zero. This error is believed to be due to the numerical computation and the generation of the body surface.

Non-dimensional wave exciting forces for various Froude numbers are given in Figures 5.19 and 5.20 for head sea and heading $\beta = 150^0$, respectively. It is indicated that for both headings, the wave exciting force becomes greater when the Froude number is increased. The non-dimensional amplitude for various Froude numbers in head sea and heading $\beta = 150^0$ are also presented in Figure 5.21 and Figure 5.22. For surge motion, the smaller Froude number gives the greater non-dimensional amplitude for both headings. For heave and pitch motions, the smaller Froude number has smaller non-dimensional motion amplitude specially for long wave lengths. For sway, roll and yaw motions, which exist in heading $\beta = 150^0$, the non-dimensional motion amplitude is increased by increasing the Froude number for almost all range of wave length to ship length ratio.

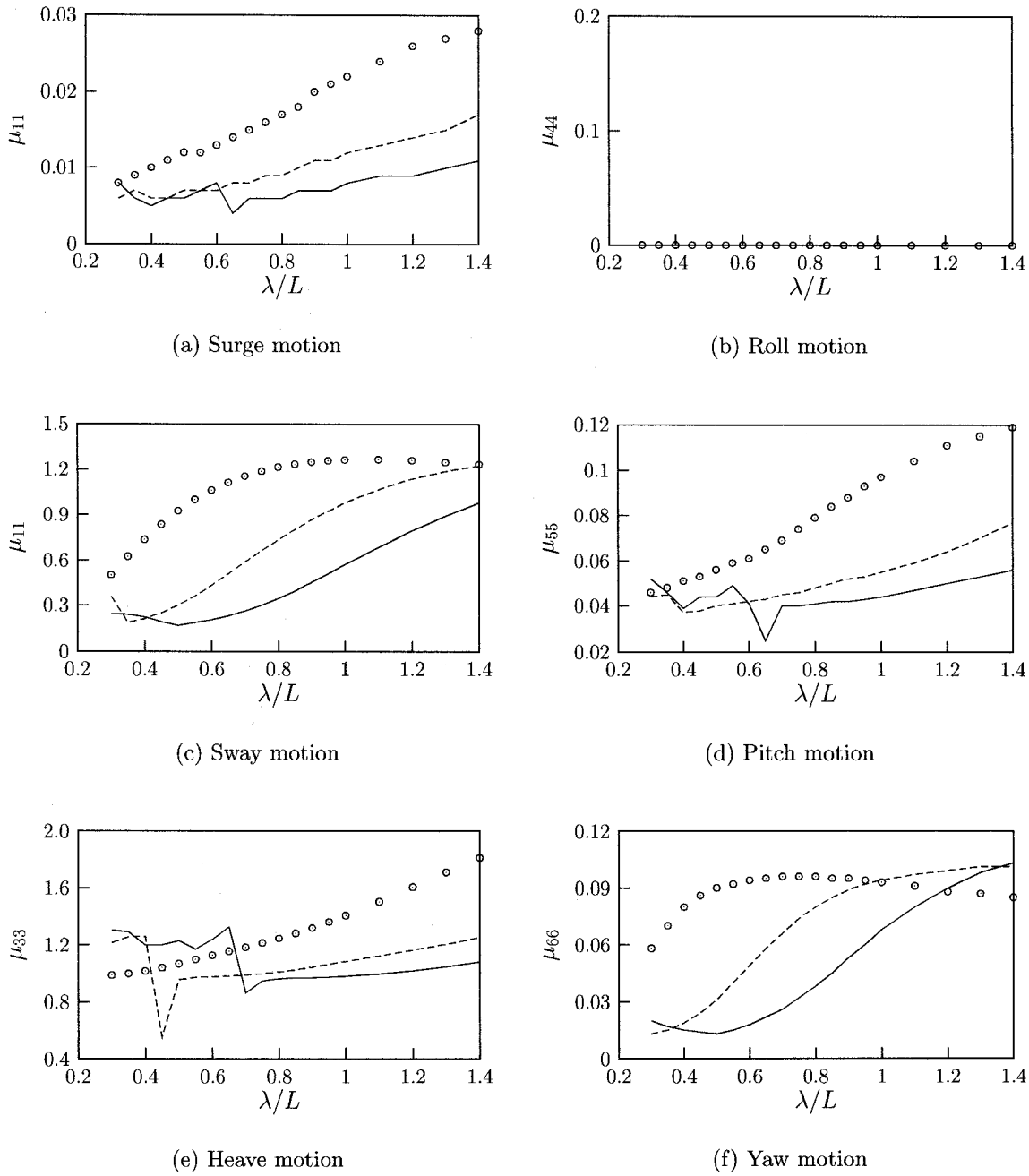

(a) Surge motion

(b) Roll motion

(c) Sway motion

(d) Pitch motion

(e) Heave motion

(f) Yaw motion

Figure 5.15: Non-dimensional added-mass coefficients of the container ship for $\beta = 180$; o o oo Fn=0, - - - - Fn=0.15, ——— Fn=0.30.

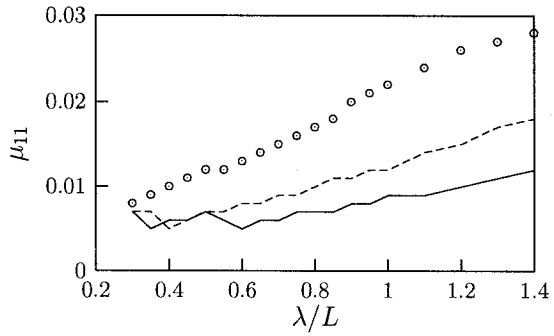

(a) Surge motion

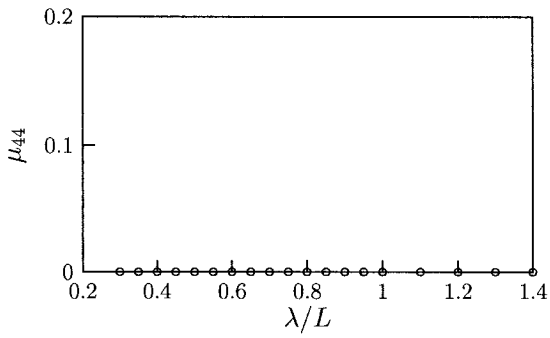

(b) Roll motion

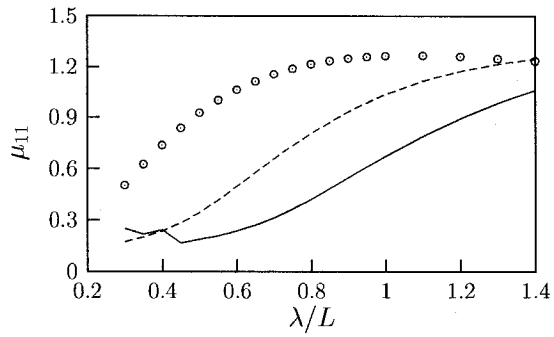

(c) Sway motion

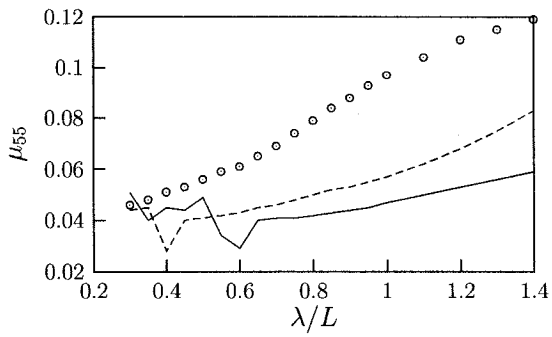

(d) Pitch motion

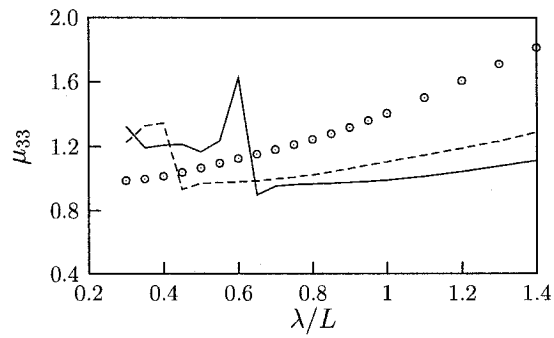

(e) Heave motion

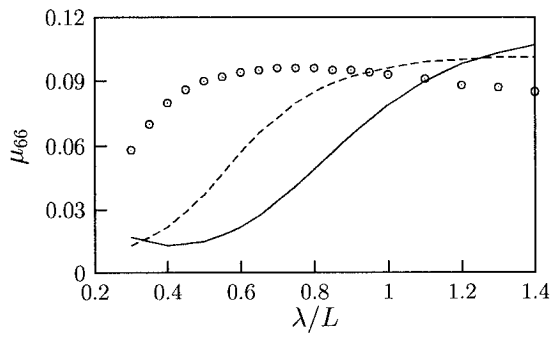

(f) Yaw motion

Figure 5.16: Non-dimensional added-mass coefficients of the container ship for $\beta = 150$; o o oo Fn=0, - - - - Fn=0.15, ——— Fn=0.30.

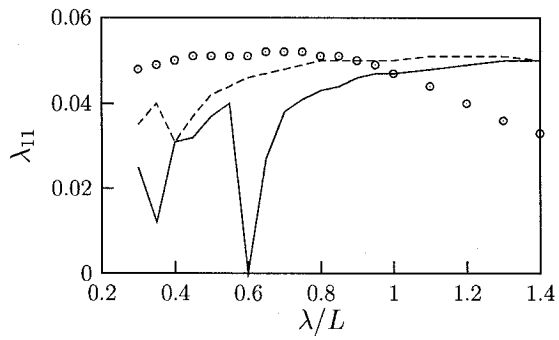

(a) Surge motion

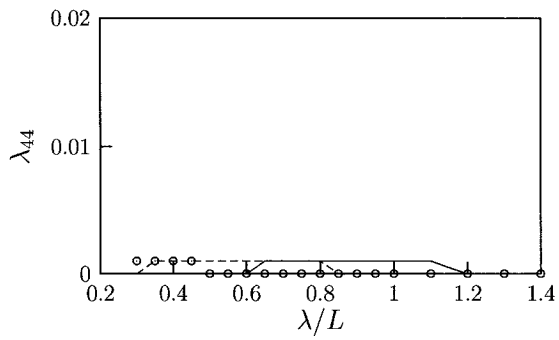

(b) Roll motion

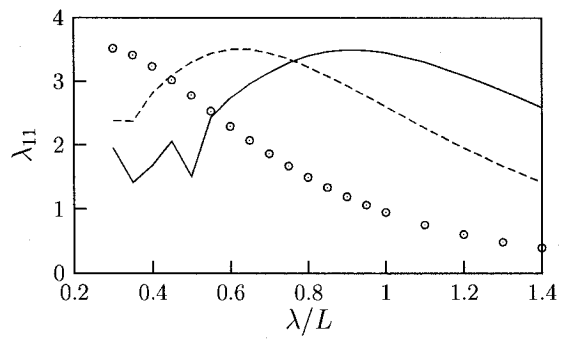

(c) Sway motion

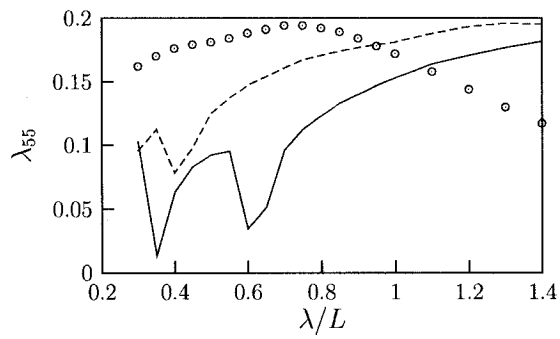

(d) Pitch motion

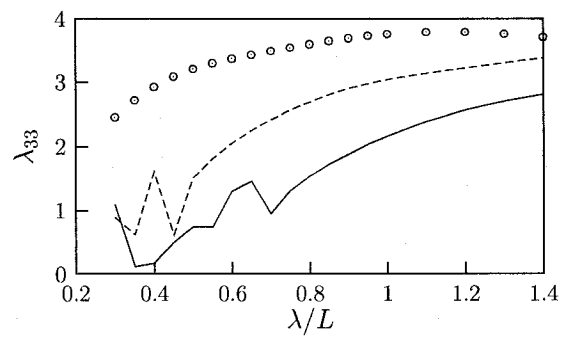

(e) Heave motion

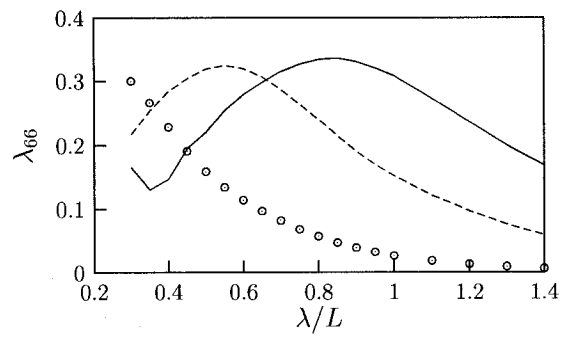

(f) Yaw motion

Figure 5.17: Non-dimensional damping coefficients of the container ship for $\beta = 180$; o o oo Fn=0, - - - - Fn=0.15, ——— Fn=0.30.

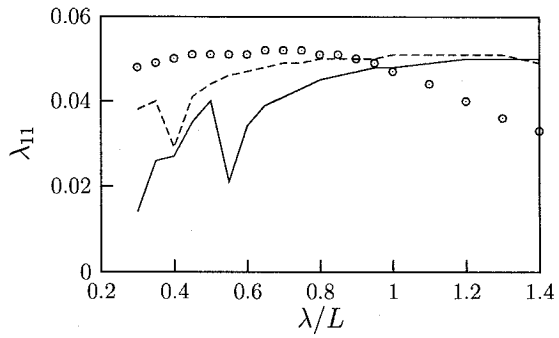

(a) Surge motion

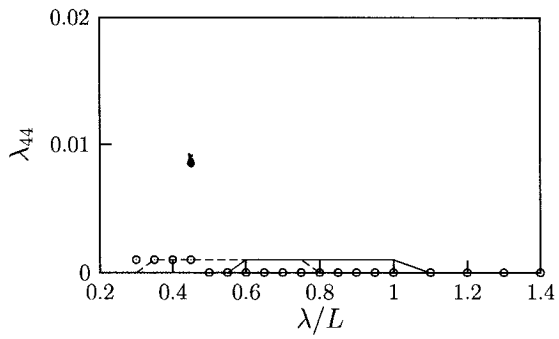

(b) Roll motion

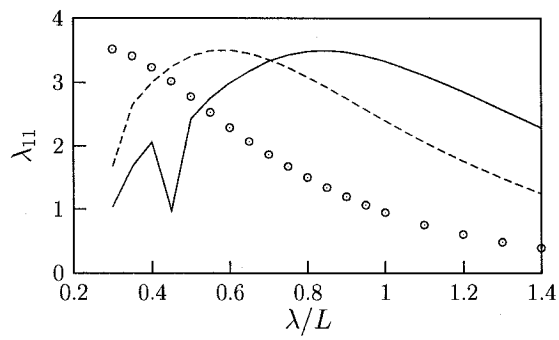

(c) Sway motion

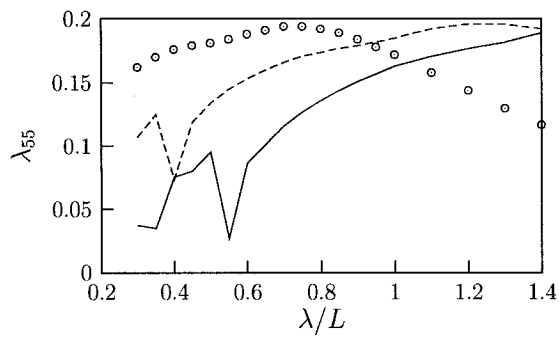

(d) Pitch motion

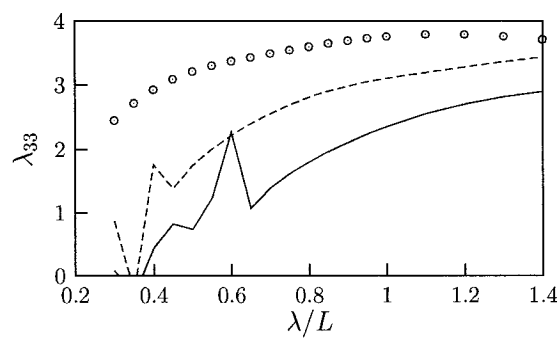

(e) Heave motion

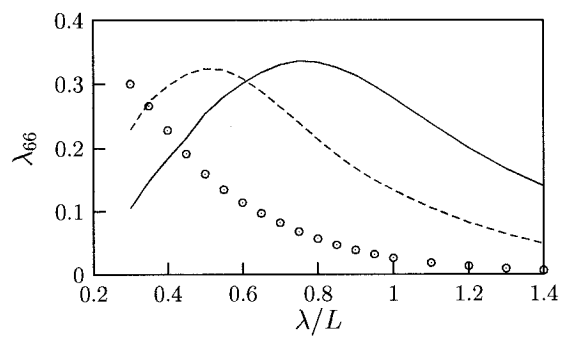

(f) Yaw motion

Figure 5.18: Non-dimensional damping coefficients of the container ship for $\beta = 150$; o o oo Fn=0, - - - - Fn=0.15, ——— Fn=0.30.

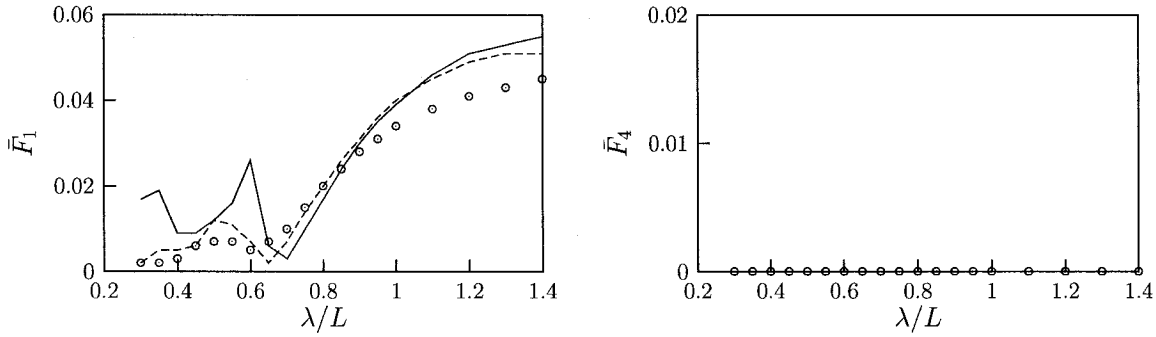

(a) Surge motion

(b) Roll motion

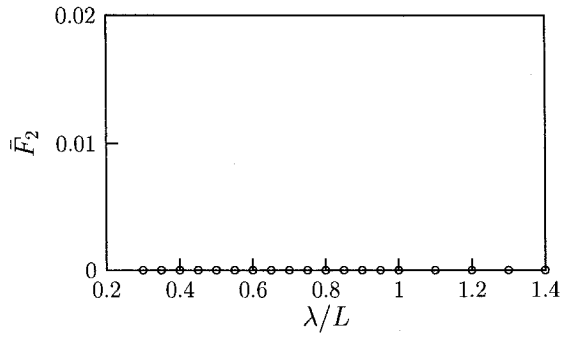

(c) Sway motion

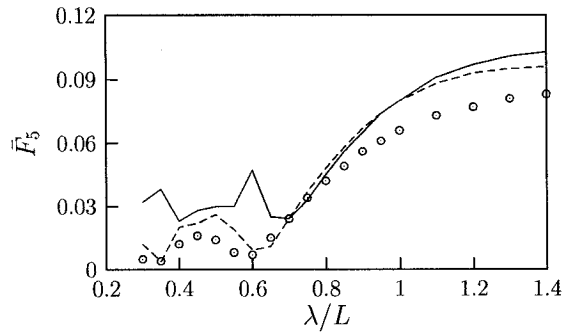

(d) Pitch motion

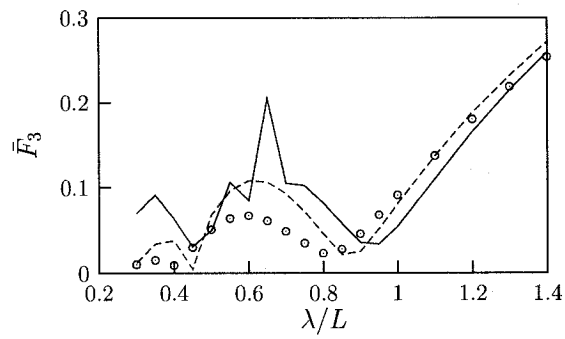

(e) Heave motion

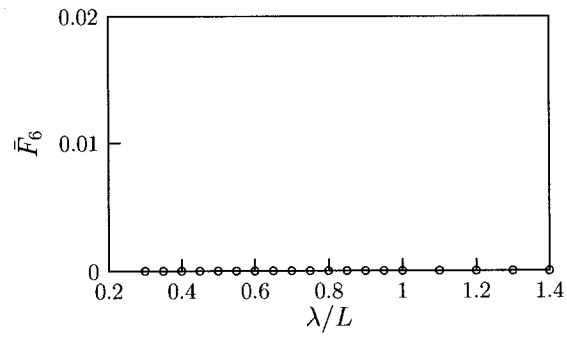

(f) Yaw motion

Figure 5.19: Non-dimensional wave exciting force of the container ship for $\beta = 180$; o o oo Fn=0, - - - - Fn=0.15, ——— Fn=0.30.

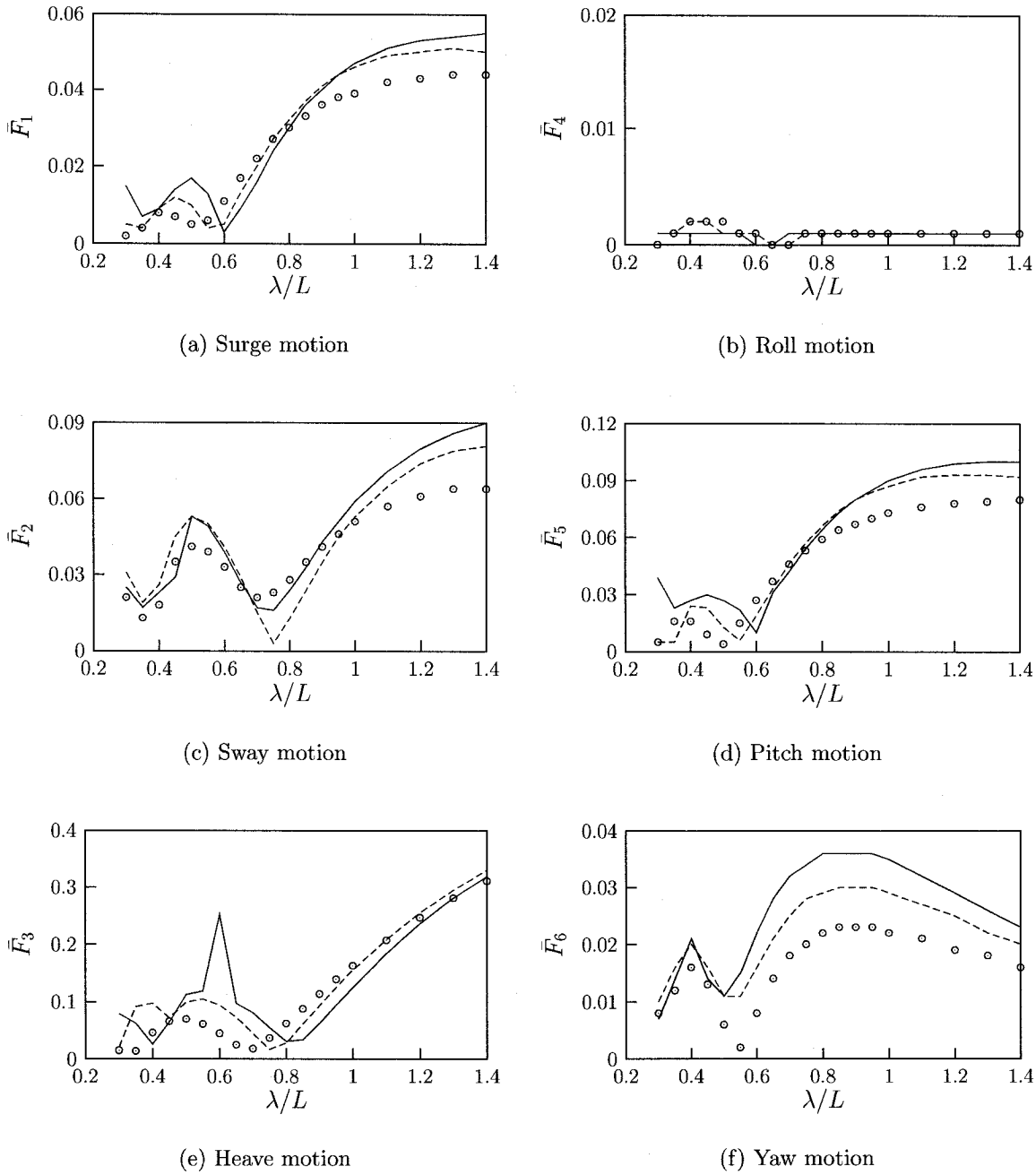

(a) Surge motion

(b) Roll motion

(c) Sway motion

(d) Pitch motion

(e) Heave motion

(f) Yaw motion

Figure 5.20: Non-dimensional wave exciting force of the container ship for $\beta = 150$; o o oo Fn=0, - - - - Fn=0.15, ——— Fn=0.30.

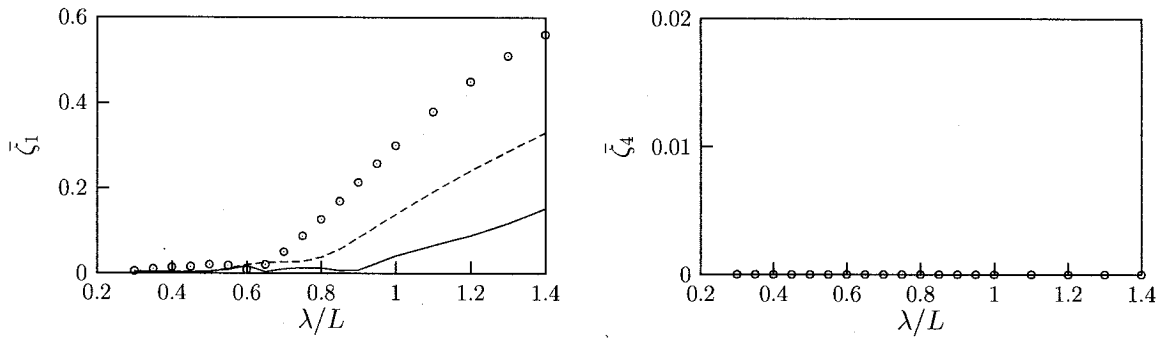

(a) Surge motion

(b) Roll motion

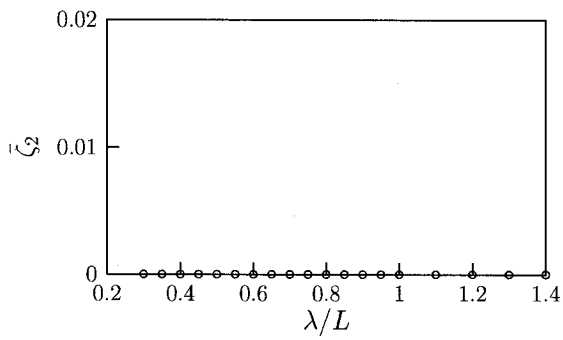

(c) Sway motion

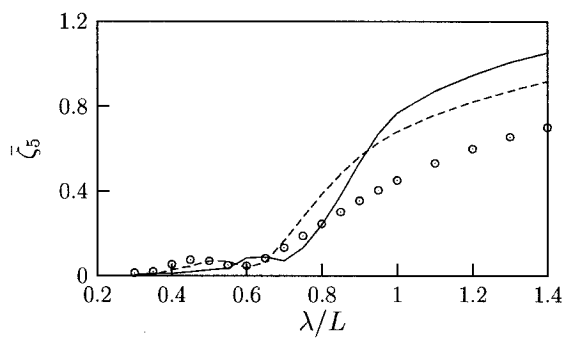

(d) Pitch motion

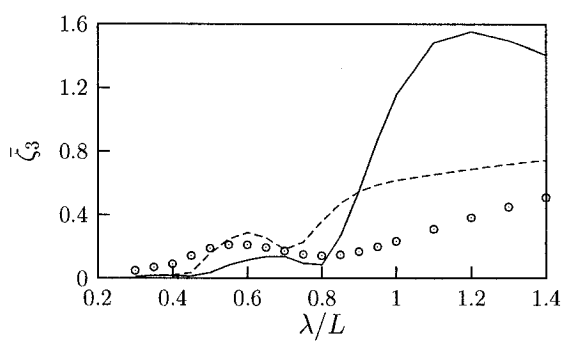

(e) Heave motion

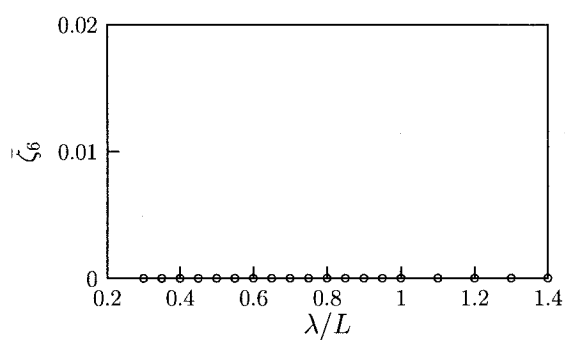

(f) Yaw motion

Figure 5.21: Non-dimensional motion displacement amplitudes of the container ship for $\beta = 180$ o o o o o Fn=0, - - - - Fn=0.15, ——— Fn=0.30.

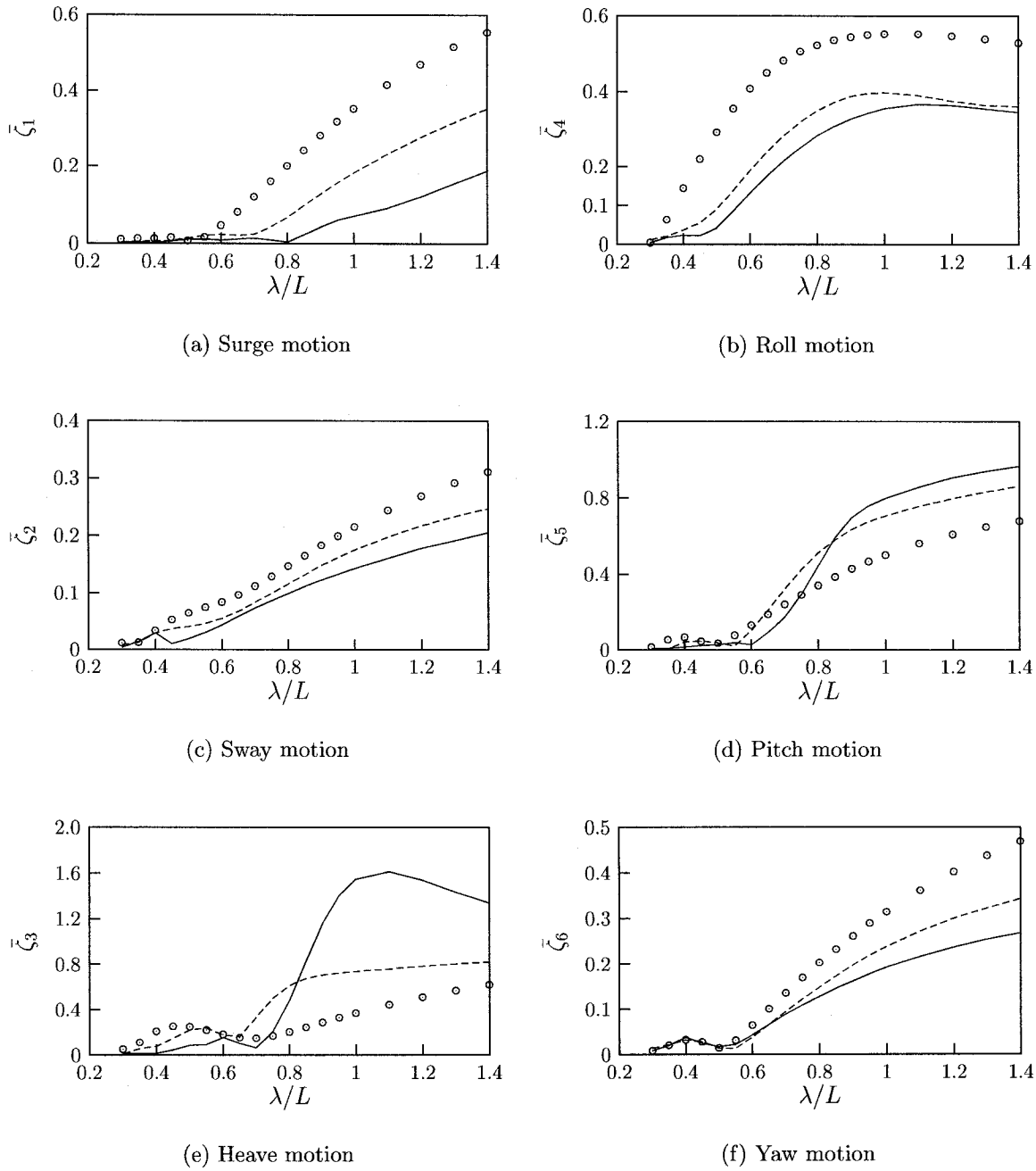

(a) Surge motion

(b) Roll motion

(c) Sway motion

(d) Pitch motion

(e) Heave motion

(f) Yaw motion

Figure 5.22: Non-dimensional motion displacement amplitudes of the container ship for $\beta = 150$; o o oo Fn=0, - - - - Fn=0.15, ——— Fn=0.30.

Chapter 6

Conclusions and Recommendations

Nonlinear solutions of two-dimensional free surface flow is investigated using Cauchy's formula in the first part of this dissertation. The desingularized Cauchy's formula for infinite domain as well as for a body moving beneath the free surface are developed. Numerical solutions of potentials and pressure coefficients for the elliptical cylinder with different dimensions and for Joukowsli airfoil of various size are obtained. Comparisons between numerical simulation and analytical results indicate that desingularized Cauchy's formula give very accurate solutions for potential flow problems in infinite domain. It is indicated that the formulation for complex potential gives more accurate results. For a body moving beneath the free surface, the simulations has been carried out for different bodies. It was found that the converged solution for the problem using Cauchy's formula cannot be obtained for many cases.

However, the results obtained for two-dimensional body moving beneath the free surface indicate that the desingularized Cauchy's formula is not sufficiently accurate,

and hence, not appropriate for fully nonlinear free surface computation. This may be due to highly nonlinearity of the problem and the error due to implementation of Kutta condition.

The main objective of the second part of the dissertation is to develop an algorithm in which the behavior of a ship advancing with constant speed in water waves can be accurately predicted.

The non-singular forms of Green's formula for three-dimensional potential problem are presented. The main advantage of desingularized formulations is that the problem can be solved directly by quadrature formula. Thus, there is no need to locally regularize the singularities in each element as usually is done by conventional panel method. The desingularized formulation has been applied to analyze the radiation and diffraction problems of the floating and submerged three-dimensional bodies with zero forward speed in regular waves.

The analysis of ship motions with forward speed is more difficult due to complexity of the interaction of the steady wave system associated with the forward motion of the ship and the unsteady wave system associated with the oscillatory motion of the ship. In order to predict the ship motion, the forward speed correction theory is used. The speed dependence of the hydrodynamic coefficients are obtained by solving the double body potential of a moving floating body with simplifying the free surface boundary condition as the rigid wall condition.

To properly distribute the collocation points over the body surface, analytical definition or parametric representation of the body surface is required. NURBS surface is

adopted to represent the body surface for its unique capability to describe the complex geometry. Moreover, the coordinates of the points on the body surface can be accurately obtained by NURBS surface. It also enables one to modify the body surface if the required hydrodynamic characteristics for the body are not achieved.

The effectiveness of the present method is demonstrated by computation of the hydrodynamic coefficients of the floating and submerged bodies. The converged solutions for a wide range of wave numbers are obtained. It is shown that the results obtained by this method are more accurate than those obtained by the panel method while the number of points used in the desingularized computation is equal to the number of panels in panel method. If the coordinates of the collocation points used in the computation is obtained from the mathematical description of the body surface, the accuracy of results is up to four decimal digit comparing to the analytical solution.

The hydrodynamic characteristics of a Wigley model and a container ship for various number of Froude number are also presented. Closed agreement between the results obtained by the present method and other existing methods, as well as experimental results shows that satisfactory results for forward-speed ship motion characteristics can be obtained with the present method.

For further work, it is recommended that the algorithm be applied for computation of wave-body interaction in finite-depth by replacing of Green function of infinite depth by finite depth Green functions with some modification in the program. Also, the method should be applied to different types of ships, specially to ships with sharp edges, for further validation and improvements. The usage of Green's function for

steady potential instead of double body potential is also recommended for further development of the algorithm.

References

[1] Atkinson, K.E. A Survey of Boundary Integral Equation Methods for the Numerical Solution of Laplace's Equation in Three-Dimension, *Numerical Solution of Integral equations,* edited by Michael A. Golberg, Plenum Press, New York and London, 1990.

[2] Beck, R.F. and Locken, A.E. Three-Dimensional Effects in Ship Relative Ship Motion Problems, Journal of Ship Research, Vol. 33, No. 4, Dec. 1989.

[3] Campana E., Lalli F. and Bulgarelli U. A Boundary Element Method for a Nonlinear Free Surface Problem, Int. J. Num. Meth. Fluids, Vol. 9, pp. 1195-1206. 1989.

[4] Chen H., Hefazi H. A Panel Method for Two-Dimensional Nonlinear Free Surface Flow , Advance in Fluid Mechanics IV, Vol. 32, pp. 269-278. 2002.

[5] choi, J.k. and Kinnas, S.A. Numerical Watre Tunnel in Two and Three dimensions, Journal of Ship Research, Vol. 42, No. 2, June 1989.

[6] Chuang, J.M. Numerical Studies on Desingularized Cauchy's Formula with Applica-

tions to Interior Potential Problems, International Journal for Numerical Methods in Engineering, Vol. 46, pp. 805-824, 1999.

[7] Flokstra, C. Comparison of Ship Motion Theories with Experiments for a Container Ship, International Shipbuilding Progress, Vol. 21, No. 238, June 1974.

[8] Forbes, L.K. Non-linear Drag-Free Flow Over a Submerged Semi-elliptical Body, Journal of Engineering Mathematics, Vol. 16, pp. 171-180, 1982.

[9] Forbes L.K. Irregular Frequency and Iterative Methods in the Solution of Steady Surface-Wave Problems in Hydrodynamics, Journal of Engineering Mathematics, Vol. 18, pp. 299-313, 1984.

[10] Forbes, L.K. On the Effect of Non-Linearity in Free-Surface Flow About a Submerged Point Vortex, Journal of Engineering Mathematics, Vol. 19, pp. 139-155, 1985.

[11] Forbes, L.K. A Numerical Method for Non-Linear Flow About a Submerged Hydrofoil, Journal of engineering Mathematics, Vol. 19, pp. 29-339, 1985.

[12] Haskind, M.D. Waves Arising From Oscillation of Bodies in Shallow Water, Society of Naval Architects and Marine Engineers, Technical Research Bulletin, n Bul, pp. 1-22, Nov. 1961.

[13] Havelock, T.H. The Wave Pattern of a Doublet in a Stream, Proc. Roy. Soc. of London, A, Vol. 121, pp. 515-523 ,1928.

[14] Hendrix, D.M. Steady Potential Flow due to a Ship Advancing at Constant Speed on a Calm Sea, PhD. Thesis, Miami University, USA, 1995.

[15] Hess J.L. Review of integral-equation techniques for solving potential-flow problems with emphasis on the the surface-source method, Computer methods in Applied Mechanics and Engineering, Vol. 5, pp. 145-196, 1975.

[16] Hess J.L. and Smith A.M. Calculation of Non-Lifting Potential Flow About Arbitrary Three-Dimensional Smooth Bodies, Journal of Ship Research, Vol. 7, pp. 22-44, 1964.

[17] Hormadka,Y.V. and Guymon, G.L. A Complex Variable Boundary Element Method Development. International Journal for Numerical Methods in Engineering, Vol. 20, pp. 25-37, 1984.

[18] Hsiung, C.C. and Huang, Z.J. A New Approach to Computational Sea-keeping Prediction, Technical Report CMVDR, 1990.

[19] Hsiung, C.C. and Huang, Z.J. Comparison of the Strip Theory and the Panel Method in Computing Ship Motion with Forward Speed, Proceedings of Symposium on Selected Topics on Marine Hydrodynamics, St. John's, Nfld, 1991.

[20] Hulme, A. The Wave Forces Acting on a Floating Hemisphere Undergoing Forced Periodic Oscillations. Journal of Fluid Mechanic, Vol. 121, pp. 443-463, 1982.

[21] Hunt, B. The Mathematical Basis and Numerical Principles of the Boundary Integral Method for Incompressible Potential Flow Over 3-D Aerodynamic Config-

urations, *Numerical Methods in Applied Fluid Dynamics* edited by B. Hunt, The Institute of Mathematical and its Application Conference Series, Academic Press Inc. Ltd., London, 1980.

[22] Hwang, W.S. and Huang, Y.Y. Nonsingular Direct Formulation of Boundary Integral Equations for Potential flows, Int. J. Num. Meth. Fluids, Vol. 26, pp. 627-635, 1998.

[23] Inglis, R.B. A Three-Dimensional Analysis of the Motion of a Rigid Ship in Waves, PhD. Thesis, University of London, London, UK, 1980.

[24] Journee J.M.J. Experimental and Calculation on 4 Wigley Hull Forms in Head Waves, Delft University of Technology, Report 0909, May 1992.

[25] Katz, J. and Plotkin, *A Low-Speed Aerodynamics, from Wing Theory to Panel Methods*, McGraw-Hill, USA, 1991.

[26] Kehr, Y.Z. and Chou, S.K. The Application of Higher Order Panel Method on Ship Wave Making Problem, 7th Conference on Naval Architecture and Ocean Engineering, SNAME R.O.C., pp. 391-399, 1994.

[27] Kim, B. and Shin, Y.S. A NURBS Panel Method for Three-Dimensional Radiation and Diffraction Problem, Journal of Ship Research, Vol. 47, No. 2, pp. 177-186,June 2003.

[28] Kim, Y.H., Kin, S.H. and Lucas, T. Advanced Panel Method for Ship Wave in-

viscid Flow Theory (SWIFT), David Taylor Research Center, Ship Hydrodynamics Department Report DTRC-89/09, 1989.

[29] Kim, Y.H. and Lucas, T. Nonlinear Ship Waves, Proceedings, 18th Symposium on Naval Hydrodynamics, Ann Arbor, Michigan, pp. 439-452, 1990.

[30] Kochin N.E., KIbel I.A. and Roze N.V. *Theoretical Hydrodynamics*, Wiley-Interscience, USA, 1964.

[31] Kokkinowrachos, K., Mavrakos, S. and Asorakos, S. Behavior of Vertical Bodies of Revolution in Waves, Ocean Engineering, Vol. 13, No. 6, pp. 505-538, 1986.

[32] Kouh, J.S. and Ho, C.H. A High Order Panel Method Based on Source Distribution and Gaussian Quadrature, Ship Technology Research, Vol. 43, pp. 38-47, 1996.

[33] Kouh, J.S. and Suen, J., A 3D Potential-Based and Desingularized High Order Panel Method, Ocean Engineering, Vol. 28, pp. 1944-1516, 2001.

[34] Lamb, H. *Hydrodynamics*, Dover Publications, New York, 1945.

[35] Landrini, M., Grytoyr, G. and Faltensen, O.M. A B-Spline Based BEM for Unsteady Free-Surface Flow, Journal of Ship Research, Vol. 43, No. 1, pp. 13-24, March 1999.

[36] Landweber, L. and Macagno, M. Irrotational Flow About Ship Forms. IHHR report, Iowa, No. 123, 1969.

[37] Lee, C.-H., Sclavounos, P.D. Removing the Irregular Frequencies from Integral Equations in Wave-Body Interactions, Journal of Fluid Mechanics, Vol. 207, pp. 393-418, Oct. 1989.

[38] Lee, C.-H., Maniar, H., Newman, J. and Zhu,X. Computations of wave loads using a B-Spline panel method, Twenty-First Symposium on Naval Hydrodynamics, 1997.

[39] Mackerle, J. and Brebbia, C.A. *The Boundary element reference book* , Southampton, England, Computational Mechanics, 1988.

[40] Maniar, H.D. A Three-Dimensional Higher Order Panel Method Based on B-Spline, PhD thesis, Massachusetts Institute of Technology, USA, 1995.

[41] Markushevich, A.I. *Theory of Functions of a Complex Variable*, Volume I, Printice-Hall Inc., 1965.

[42] Maruo, H. and Ogiwara, S. A method of computation for steady ship-waves with non-linear free surface conditions, Fourth Int. Conf. Numerical Ship Hydrodynamics, Washington, pp. 218-233, 1985.

[43] Maruo, H. and Song, W.S. Numerical Appraisal of the New Slender Ship Formulation in Steady Motion, Proceedings, 18th symposium on Naval Hydrodynamics, Ann Arbor, Michigan, pp. 239-257, 1990

[44] Milne-Thompson, L.M. *Theoretical Hydrodynamics*, Macmillan, London, 1960.

[45] Muskhelishevili, N.I. *Singular Integral Equations*, Second Edition, Groningen, Holand, 1953.

[46] Newman, J.N. *Marine Hydrodynamics*, Six printing, The MIT Press, US, 1989.

[47] Newman, J.N. Algorithms for Free-Surface Green Function, Journal of Engineering mathematics, Vol. 19, pp. 57-67, 1985.

[48] Newman, J.N. The Theory of Ship Motions. Advances in Applied Mechanics 18, pp. 221-283, 1978.

[49] Newman, J.N. The Damping of an Oscillating Ellipsoid Near a Free Surface, Journal of Ship Research, Vol. 5, pp. 44-58, 1961.

[50] Okan, M.B. and Umpleby, S.M. Free Surface Flow Around Arbitrary Two-Dimwnsional Bodies by B-splines, International Shipbuilding Progress, Vol 32, No. 372, pp, 182-187, Aug. 1985.

[51] Okan, M.B. and Umpleby, S.M. Use of the B-splines for the Calculation of Two-Dimensional Potential Flow Around Arbitrary Bodies, International Shipbuilding Progress, Vol. 32, No. 370, pp. 151-155, June 1985.

[52] Piegl, L. and Tiller W. *The NURBS Book*, 2nd Edition, Speringer, Germany, 1997.

[53] Qiu, W. A Panel Free-Method for Time Domain Analysis of Floating Bodies in Waves, PhD. thesis, Dalhousie University, 2001.

[54] Rahman, M. Effects of Diffraction and Radiation on a Submerged Sphere, IJMMS, Vol. 28, No. 9, pp. 499-515, 2001.

[55] Rahman M. Simulation of Diffraction of Ocean Waves by a Submerged Sphere in Finite Depth, Applied Ocean Research, Vol. 23, No. 6, pp. 305-317, Dec. 2001.

[56] Schutlz, W. and Wong, S.W. Solution of Potential Problems Using an Over Determined Complex Boundary Integral Method, J. Comput. Physics, Vol. 84, pp. 414-440, 1989.

[57] Shen, H.T., Farell, C. Numerical Calculation of the Wave Integrals in the Linearized Theory of Water Waves, Journal of Ship Research, Vol. 21, No. 1, pp. 1-10, March 1977.

[58] Salvesen, N., Tuck, E.O. and Faltinsen, O. Ship Motions and Sea Loads, Transaction of SNAME, Vol. 78, pp. 250-279, 1970.

[59] Scalvounos, P.D. and Nalos, D.E. Stability Analysis of Panel Methods for Free-Surface Flows with Forward Speed. *Proceedings of the 17th Symposium on Naval Hydrodynamics,* The Hague, pp. 173-193, 1988.

[60] Schmitke, R.T. Ship Sway, Roll and Yaw Motions in Oblique Seas, SNAME Transaction, Vol. 86, pp. 24-46, 1978.

[61] Schwartz L.w. Nonlinear Solution for an Applied Overpressure on a Moving Stream, Journal of Engineering Mathematics, Vol. 15, No. 2, pp. 147-156, April 1981.

[62] Sheng, J. Ship Geometry Approximation Using Non-Uniform Rational B-Spline with Application to Computational Hydrodynamics, MASc thesis, Dalhousie University, 2002.

[63] Sladek, V. and Sladek, J. Non-Singular Boundary Integral Representation of Potential Field Gradients, Int. J. Numer. Meth. Engng., Vol. 33, pp. 1181-1195, 1992.

[64] Sladek, V., Sladek, J. and Tanaka, M. Regularization of Hypersingular and Nearly Singular Integrals in the Potential Theory and Elasticity. Int. J. Numer. Meth. Engng., Vol. 36, pp. 1609-1628, 1993.

[65] Söding, H. A Method for Accurate Force Calculation in Potential Flow, Ship Technology Research, Vol. 40, pp. 176-193, 1993.

[66] St. Denis, M. and Pierson, W.G. On the Motion of Ships in Confused Seas, Trans SNAME 61, pp 280-375, 1953.

[67] Tanaka, M., Sladek M.V. and Sladek, J. Regularization Techniques Applied to Boundary Element Methods. ASME Applied Mechanics. Reviews 47, pp. 457-499, 1994.

[68] Telste, J.G. and Noblesse, F. Numerical Evaluation of the Green Function of Water-Wave Radiation and Diffraction , Journal of Ship Research, Vol. 30, No. 2, pp. 69-84, June 1986.

[69] Thiart, G.D. and Bertram, V. Staggered-Grid Panel Method for Hydrofoils with

Fully Nonlinear Free-Surface Effects, International Shipbuilding Progress, Vol. 45, No. 444, pp. 313-328, Dec. 1998.

[70] Ursell, F. On the Heave Motion of Circular Cylinder in the Surface of Fluid, Quarter Journal of Mechanics and Applied Mathematics, Vol. 2, pp. 335-353, 1949.

[71] Webster, W.C. The Flow About Arbitrary Three-Dimensional Smooth Bodies, Journal of Ship Research, pp. 206-218, 1975.

[72] Wehausen, J.V. and Laiton, E.V. Surface Waves, In Handbuck der Physik, Springer, Berlin, pp. 446-778, 1960.

[73] Wu, G.X. and Taylor, R.E. The Exciting Force on a Submerged Spheroid in Regular Waves, Journal of Fluid Mechanics, Vol. 182, pp. 411-426, 1987.

[74] Wu, G.X. A Numerical Scheme for Calculating the m_j Terms in Wave-Current-Body Interaction, Applied Ocean Research, Vol 13, No. 6, pp 317-319, Dec. 1991.

[75] Wu, G.X. Hydrodynamic Forces on a Submerged Cylinder Advancing in Water of Finite Depth, Journal of Fluid Mechanics, No. 224, pp. 645-659, 1991.

[76] Xü, H. Numerical Study of Fully Nonlinear Water Waves in Three-Dimensions, PhD. thesis, Department of Ocean Engineering, Massachusetts Institute of Technology, 1992.

[77] Yang, S.A. On the Singularities of Green's Formula and Its Normal Derivative,

with an Application to Surface-Wave-Body Interaction Problem. Int, J. Numer. Meth. Engng., Vol, 47, pp. 1841-1864, 2000.

[78] Yükselen, M.A. Superposition Technique for Potential Flow Around an Airfoil and Control of the Circulation, International Journal for Numerical Methods in Fluids, Vol. 22, pp. 1013-1022, 1996.

[79] Zhu, X. Irregular Frequency Removal from the Boundary Integral Equation for the Wave-Body Problem, MSc. thesis, Massachusetts Institute of Technology, Aug. 1994.

Appendix A

Steady Flow Computation

A.1 Steady Flow Formulation

Consider a body moving with a constant velocity in semi infinite ideal fluid with a free surface without surface tension. Assume that the flow is irrotational. The steady three-dimensional flow is described by a total velocity potential, Φ

$$\Phi = \phi_I + \phi_d \tag{A.1}$$

where ϕ_I is the velocity potential of the uniform flow Ux, and ϕ_d is the disturbance velocity potential which must satisfy the following conditions:

$$\nabla^2 \phi_d = 0 \qquad \text{in the fluid domain} \tag{A.2}$$

$$\frac{\partial \phi_d}{\partial n} = -\vec{U}.\vec{n} \qquad \text{on the body surface} \tag{A.3}$$

$$\frac{\partial \phi_d}{\partial z} = 0 \qquad for \qquad z = 0 \tag{A.4}$$

$$\nabla \phi_d = 0 \qquad at\ infinity \tag{A.5}$$

where $\vec{n}$ is the outward normal on the body surface.

The associated boundary integral equation for the total velocity potential is given by Hwang and Huang [22]

$$4\pi\Phi(p) + \int_{S_b} \{\Phi(q) - \Phi(p)\} \frac{\partial G(p,q)}{\partial n_q} ds_q = 4\phi_I(p) \tag{A.6}$$

which is the nonsingular form of the boundary integral equation.

The green function of image is applied to solve the boundary integral equation

$$G(p,q) = \frac{1}{r_{pq}} + \frac{1}{r_{pq'}} \tag{A.7}$$

where p and q are the field and source points on the body surface and q' is the image of q with respect to $z = 0$. Consequently $r_{pq} = \sqrt{(x_q - x_p)^2 + (y_q - y_p)^2 + (z_q - z_p)^2}$ and $r_{pq'} = \sqrt{(x_q - x_p)^2 + (y_q - y_p)^2 + (z_q + z_p)^2}$. By substituting the green function, Equation (A.6) can be expressed as:

$$4\pi\Phi(p) - \int_{S_b} \{\Phi(q) - \Phi(p)\} \left\{ \frac{\vec{r}_{pq}.\vec{n}_q}{r_{pq}^3} + \frac{\vec{r}_{pq'}.\vec{n}_q}{r_{pq'}^3} \right\} ds_q = 4\phi_I(p) \tag{A.8}$$

Gaussian quadrature of arbitrary order K_1 and K_2 are used to discretize the integral

equation. The discretized equation is written as:

$$4\pi\Phi_i - \sum_{j=1,j\neq i}^{K} \left\{ \frac{\vec{r}_{ij}.\vec{n}_j}{r_{ij}^3} + \frac{\vec{r}_{ij'}.\vec{n}_j}{r_{ij'}^3} \right\} (\Phi_j - \Phi_i) J_j w_j = 4\phi_{I_i} \tag{A.9}$$

where J and w are the scaling factor and weights of the Gaussian quadrature. K is the total number of Gaussian points on the free surface, $K = K_1 \times K_2$. Equation (A.9) can be written in matrix form

$$[A_{ij}]\Phi_j = 4\phi_{Ii} \tag{A.10}$$

where

$$\begin{cases} A_{ij} = \sum_{j=1,j\neq i}^{K} \left\{ \frac{\vec{r}_{ij}.\vec{n}_j}{r_{ij}^3} + \frac{\vec{r}_{ij'}.\vec{n}_j}{r_{ij'}^3} \right\} J_j w_j & j \neq i \\ A_{ii} = 4\pi + \sum_{j=1,j\neq i}^{K} \left\{ \frac{\vec{r}_{ij}.\vec{n}_j}{r_{ij}^3} + \frac{\vec{r}_{ij'}.\vec{n}_j}{r_{ij'}^3} \right\} J_j w_j \end{cases} \tag{A.11}$$

Appendix B

Description of the Body surface by NURBS

B.1 Curve Representation with NURBS

The geometry of a two- or three-dimensional body can be modeled by NURBS in a $(\bar{u})$ or $(\bar{u}, \bar{v})$ parametric space respectively. A curve in a parametric space can be defined by [52]

$$\vec{Q}(\bar{u}) = (x(\bar{u}), y(\bar{u})) = \frac{\sum_{i=1}^{n} \mathcal{N}_{i,p}(\bar{u}) P_i \bar{w}_i}{\sum_{i=1}^{n} \mathcal{N}_{i,p}(\bar{u}) \bar{w}_i} \tag{B.1}$$

where x and y are the position of the points on the curve, $\bar{u}$ is the parametric value of the NURBS curve, $n+1$ is the number of control point in the u direction, P_i are the control points and the $\bar{w}_i$ are the weights. $\mathcal{N}_{i,p}$ are the pth-degree B-spline basis

function defined as

$$\mathcal{N}_{i,p} = \begin{cases} 1 & \text{if} \quad u_i \leq u < u_{i+1} \\ 0 & \text{otherwise} \end{cases}$$

$$\mathcal{N}_{i,p} = \frac{u - u_i}{u_{i+p} - u_i}\mathcal{N}_{i,p-1} + \frac{u_{i+p+1} - u}{u_{i+p+1} - u_{i+1}}\mathcal{N}_{i+1,p-1} \tag{B.2}$$

Using normalized cord length $\bar{u}_k$ can be described

$$\bar{u}_0 = 0 \ , \bar{u}_n = 1 \ \ and \ \ \bar{u}_k = u_{k-1} + \frac{|\vec{Q}_k - \vec{Q}_{k-1}|}{d} \qquad k = 1, ...n-1 \tag{B.3}$$

where d in the total cord length

$$d = \sum_{k=1}^{n} |\vec{Q}_k - \vec{Q}_{k-1}| \tag{B.4}$$

After $\bar{u}_k$ is is defined for given data points $\vec{Q}_k$, the technique of averaging can be used to compute the components u_i's of the nonuniform knot vector $\bar{U}$

$$\bar{U} = \{\underbrace{0, ..., 0}_{p+1}, u_{p+1}, ..., u_{m-p-1}, \underbrace{1, ..., 1}_{p+1}\}$$

where

$$u_0 = \cdots = u_p = 0 \qquad u_{m-p} = \cdots = u_p = 1$$

$$u_{j+p} = \frac{1}{p}\sum_{i=j}^{j+p-1} \bar{u}_i \qquad \text{for} \quad j = 1, ..., n-p \tag{B.5}$$

Using Equations (B.3), (B.4) and (B.5), the basis function can be computed from Euations (B.2). By setting the weight factor equal to one for each control points, a system of linear equation with $n+1$ unknown, P_i, can be formed from Equation (B.1)

$$[\mathcal{N}_{i,p}(\bar{u})]\{P_i\} = \{Q_i\} \tag{B.6}$$

B.2 Surface Representation by NURBS

The Non Uniform Rational B-Spline (NURBS) method can be used to model the geometry of an arbitrary body. The NURBS surface is given by Piegl and Tiller [52] as

$$\vec{\mathcal{S}}(\bar{u}, \bar{v}) = (x(\bar{u}, \bar{v}), y(\bar{u}, \bar{v}), z(\bar{u}, \bar{v}) = \frac{\sum_{i=1}^{n}\sum_{j=1}^{m}\mathcal{N}_{i,p}(\bar{u})\mathcal{N}_{j,q}(\bar{v})P_{i,j}\bar{w}_{i,j}}{\sum_{i=1}^{n}\sum_{j=1}^{m}\mathcal{N}_{i,p}(\bar{u})\mathcal{N}_{j,q}(\bar{v})\bar{w}_{i,j}} \tag{B.7}$$

where, x, y and z represent the position of the points in the NURBS surface. Also, u and v are the parametric values of the NURBS surface and n and m are the number of control points in the $\bar{u}$ and $\bar{v}$ directions, $0 \leq u, v \leq 1$. $P_{i,j}$ and $\bar{w}_{i,j}$ are the control points and weighted functions respectively. $\mathcal{N}_{i,p}(\bar{u})$ and $\mathcal{N}_{j,q}(\bar{v})$ are basis functions with degrees of p and q in $\bar{u}$ and $\bar{v}$ directions, respectively.

With unit weighting factors, a non rational B-spline surface interpolating a set of

$n \times m$ given data points $\mathcal{X}_{k,l}$, can be written as:

$$\mathcal{X}_{k,l} = \vec{\mathcal{S}}(\bar{u}, \bar{v}) = \sum_{i=1}^{n}\sum_{j=1}^{m}\mathcal{N}_{i,p}(\bar{u})\mathcal{N}_{j,q}(\bar{v})P_{i,j} \tag{B.8}$$

Equation (B.8) represents $n \times m$ linear equations in the unknown $P_{i,j}$. The $P_{i,j}$ can be obtained as a sequence of curve interpolations.

$$\mathcal{X}_{k,l} = \sum_{i=1}^{n}\mathcal{N}_{i,p}(\bar{u})\left\{\sum_{j=1}^{m}\mathcal{N}_{j,q}(\bar{v})P_{i,j}\right\} = \sum_{i=1}^{n}\mathcal{N}_{i,p}(\bar{u})\mathcal{R}_{i,l} \tag{B.9}$$

where

$$\mathcal{R}_{i,l} = \sum_{j=1}^{m}\mathcal{N}_{j,q}(\bar{v})P_{i,j} \tag{B.10}$$

Equation (B.9) is a curve interpolation through the points $\mathcal{X}_{k,l}$, $k = 1, ..., n$ and fixed l. The $\mathcal{R}_{i,l}$ obtained in Equation (B.9) are the control points of the curve on the surface at fixed $\bar{v}_l$. Equation (B.10) is again a curve interpolation through the points $\mathcal{R}_{i,l}$ for fixed i and varying l. Letting i vary, all the $P_{i,j}$ can be obtained.

One of the common methods of computing reasonable values for the $\bar{u}_k$ and $\bar{v}_l$ is to use the total cord length as used in curve interpolation through a set of data points . Parameters $\bar{u}_1^l, ..., \bar{u}_n^l$ are computed for each l, and then each $\bar{u}_k$ is obtained by averaging across all $\bar{u}_k^l$.

$$\bar{u}_k^l = \bar{u}_{k-1}^l + \frac{\mathcal{X}_{k,l} - \mathcal{X}_{k-1,l}}{\sum_{i=1}^{n}\mathcal{X}_{k,l} - \mathcal{X}_{k-1,l}} \qquad for \qquad l = 1, ..., n \tag{B.11}$$

$$\bar{u}_k = \frac{1}{m}\sum_{l=1}^{m}\bar{u}_k^l \qquad \text{for} \quad m = 1, ..., n \tag{B.12}$$

$\bar{u}_1 = 0$ and $\bar{u}_k = 1$. The procedure of obtaining $\bar{v}_l$ is analogous to $\bar{u}_k$.

The NURBS provides construction of a very accurate surface for ruled surface. In fact, for the ruled surface in parametric space $(\bar{u}, \bar{v})$, which is constructed by rotation of a curve about an axis, one of the parameters $\bar{u}$ or $\bar{v}$ is constant. NURBS surface description of some three-dimensional bodies can also be obtained by scaling of another curve or surface. For instance, a sphere surface can be obtained by rotating a circle through its center. By scaling a sphere in different axis, the spheroid and ellipsoid with different dimensions can be obtained.

To demonstrate the technique, two different surface, one for ellipsoid and the other for the Wigley hull are generated. It is obvious that the NURBS surface representation of ellipsoid can be obtained by the scaling of a circle or by surface interpolating through a set of data points. However, since an arbitrary body has no mathematical description and cannot be dealt as the ruled surface, generating of the body surface through a set of given data points is more practical in hydrodynamic applications.

Figure B.1 shows an ellipsoid obtained by scaling a sphere with semi axis of $6, 2, 1$ in x, y and z direction respectively. The sphere is obtained from rotation of a circle about its center. The knots, weights and control points used to generate the circle are

$$\bar{U} = \left\{0, 0, 0, \frac{1}{4}, \frac{1}{4}, \frac{1}{2}, \frac{1}{2}, \frac{3}{4}, \frac{3}{4}, 1, 1, 1\right\}$$

$$\{\bar{w}_i\} = \left\{1, \frac{\sqrt{2}}{2}, 1, \frac{\sqrt{2}}{2}, 1, \frac{\sqrt{2}}{2}, 1, \frac{\sqrt{2}}{2}, 1\right\}$$

$$\{P_i\} = \{(1,0),(1,1),(0,1),(-1,1),(-1,0),(-1,-1),(0,-1),(1,-1),(1,0)\}$$

In this case the root mean square error of normals (RMS_n)is less than 10^{-7}. The Root Mean Square of normals is defined as

$$RMS_n = \sqrt{\frac{1}{k}\sum_{i=1}^{k}\left\{\left(\frac{n_{x_i} - \bar{n}_{x_i}}{\bar{n}_{x_i}}\right)^2 + \left(\frac{n_{y_i} - \bar{n}_{y_i}}{\bar{n}_{y_i}}\right)^2 + \left(\frac{n_{z_i} - \bar{n}_{z_i}}{\bar{n}_{z_i}}\right)^2\right\}} \tag{B.13}$$

where n and $\bar{n}$ denote the normals on the exact geometry and the NURBS description of the body surface, respectively. An ellipsoid with the same dimensions is also generated using the data points of the surface. Seven equal-spaced stations are selected in the x-direction and seven equal-spaced water lines in the z-direction. The coordinates of these points are obtained from the mathematical description of the ellipsoid. The NURBS surface is fitted to these points and the coordinates and other parameters of the Gaussian points on the NURBS surface are computed. The root mean square error of normals and coordinates for NURBS surface of an ellipsoid with different numbers of Gaussian points are depicted in Figure B.2. It is shown that the error for normals and coordinates are almost independent of the number of Gaussian points. However, the error of normals is much less than the error of coordinates.

Figure B.3 shows the body surface of a Wigley hull. This Wigley hull is mathemat-

ically described by [24]

$$y = \frac{B}{2}\left[1 - \left(\frac{2x}{L}\right)^2\right]\left[1 - \left(\frac{z}{D}\right)^2\right] \tag{B.14}$$

where L, B and D are the length, breadth and depth of the hull, respectively. The offsets for ten sections and six water lines are calculated from the mathematical description of the hull. The NURBS surface is then fitted to these points and the coordinates and other parameters of the Gaussian points on the NURBS surface are computed. The root mean square error of normals are depicted on Figure B.4. Again, more accurate results are obtained by increasing the number of Gaussian points.

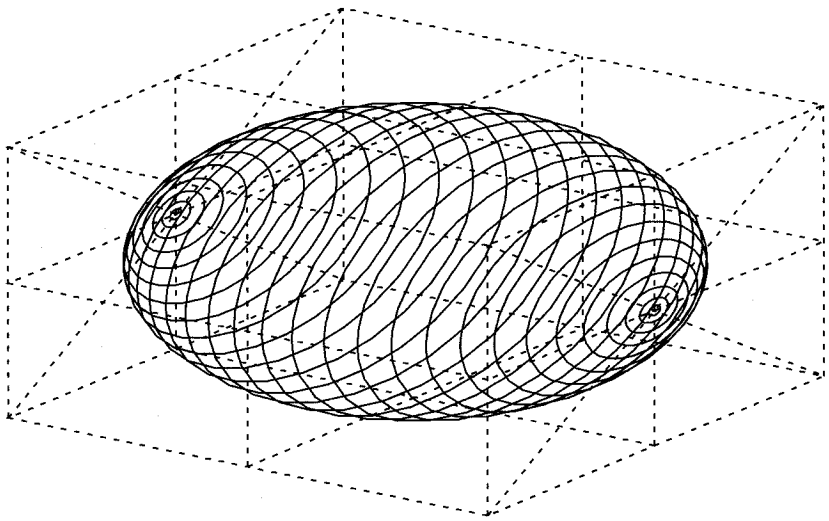

Figure B.1: NURBS description of an ellipsoid obtained by scaling a sphere

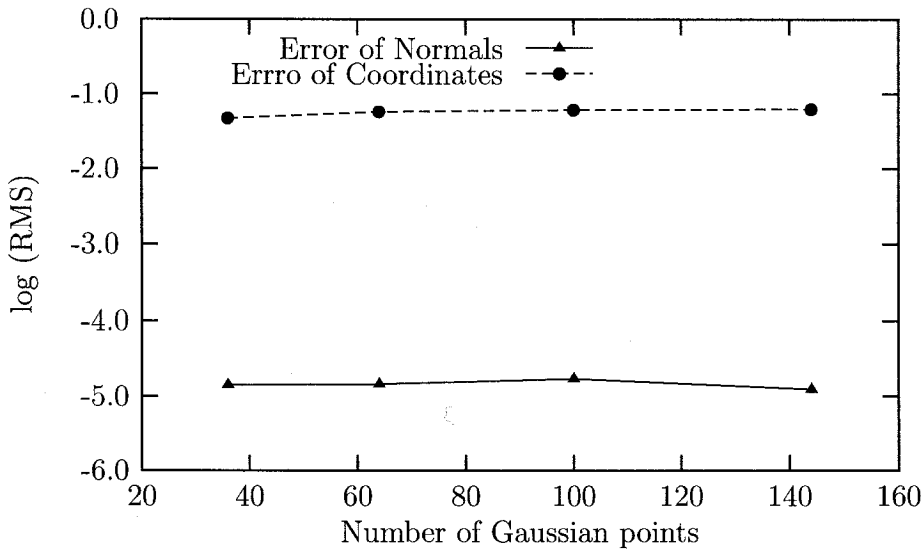

Figure B.2: Root mean square error of normals for an ellipsoid

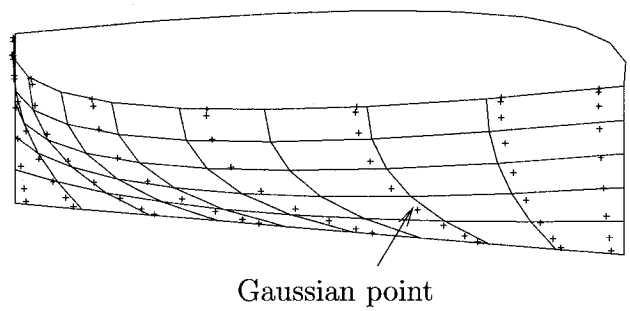

Figure B.3: Geometry of a Wigley hull; (——) Given sections and water lines, (+) Gaussian points on NURBS surface.

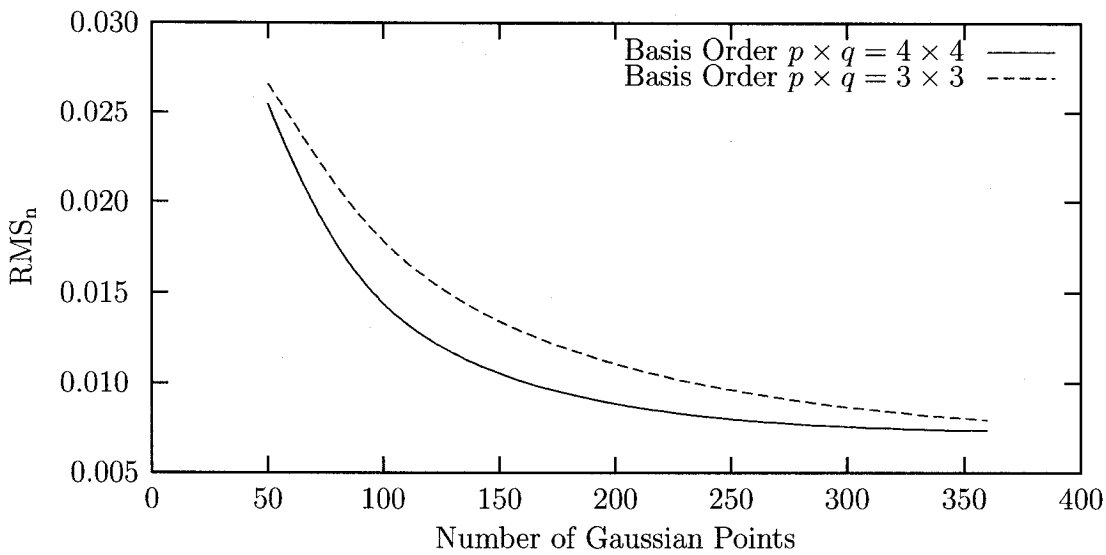

Figure B.4: Root Mean Square error of normals for a Wigley hull

Appendix C

Numerical Procedure

The procedure for numerical computation of ship motions described in Part Two of this study is given in Figure C.1.

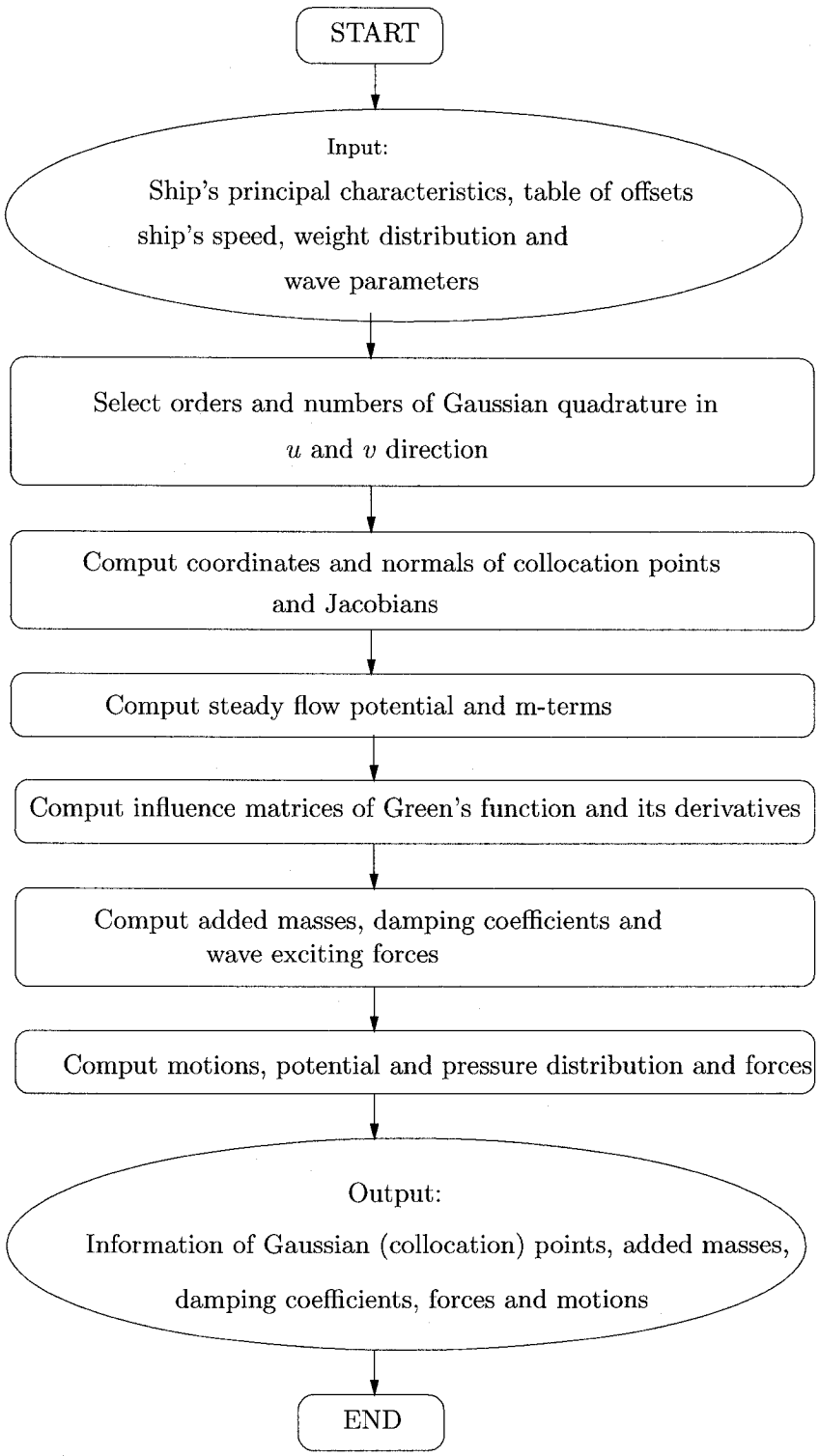

Figure C.1: Flow chart of numerical procedure.

Appendix D

Exciting Forces for a Spheroid

The numerical simulation results for surge and heave motions of a spheroid with different aspect ratio, a/b, are given in this Appendix. Figures D.1 through D.4 show the converge solutions for surge and heave exiting forces for different submergence and wave numbers. The converged results for different aspect ratio are also given in Figures D.3 and D.4. Added-mass and damping coefficients for surge and heave motions of a spheroid with the depth of submergence, $h = 3$, are given in Figures D.5 and D.6. These results are obtained based on the desingularized method developed in this dissertation and the panel method which also developed for comparison purpose. The results of the present method are in good agreement with the analytical results given by Wu and Taylor [73]. As it is shown, the present method with 512 points gives more accurate results than the panel method with 1280 panels.

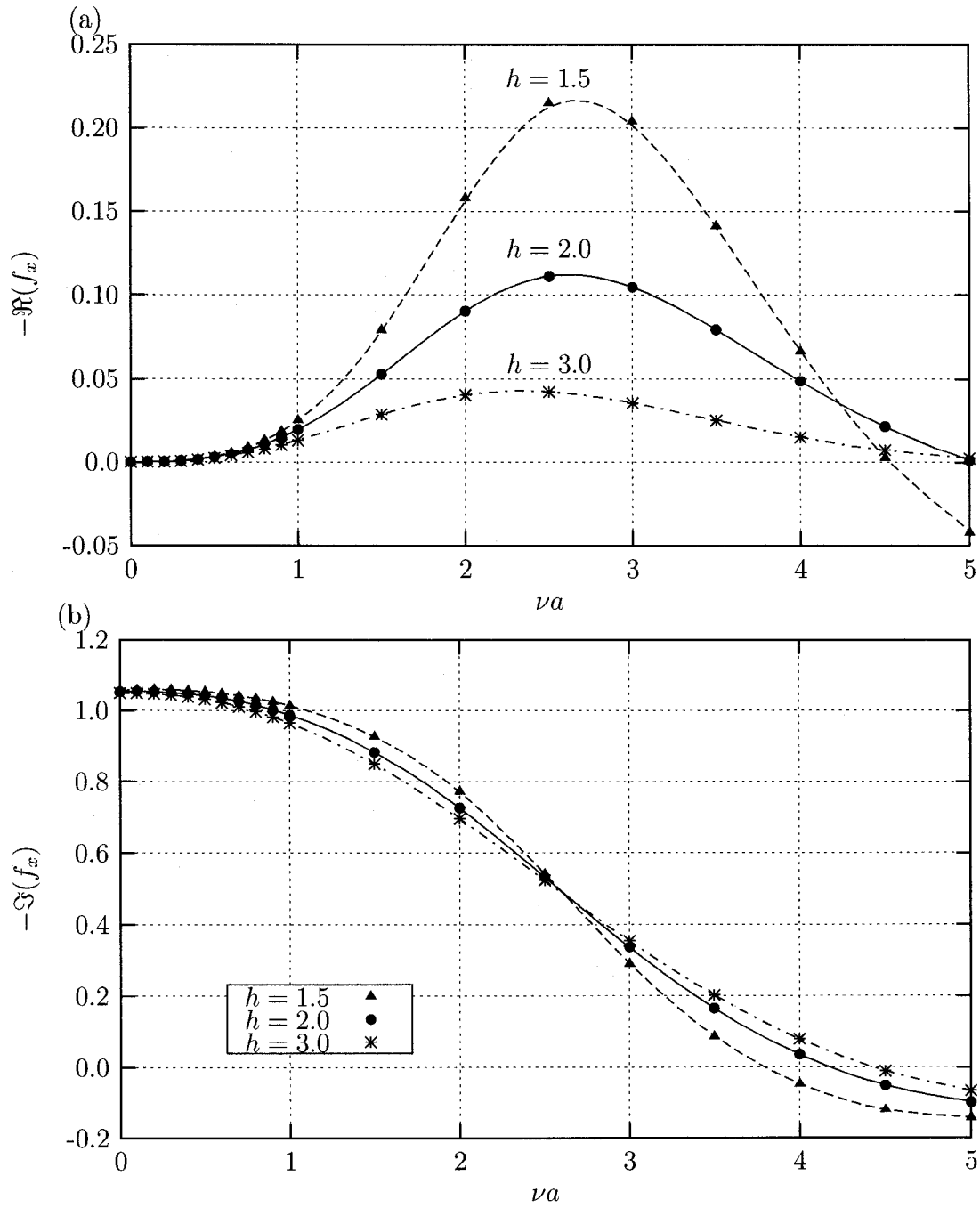

Figure D.1: Numerical results of non-dimensional surge force on a spheroid ($a = 6b$) with 16×32 Gaussian points; (a) Real part, (b) Imaginary part.

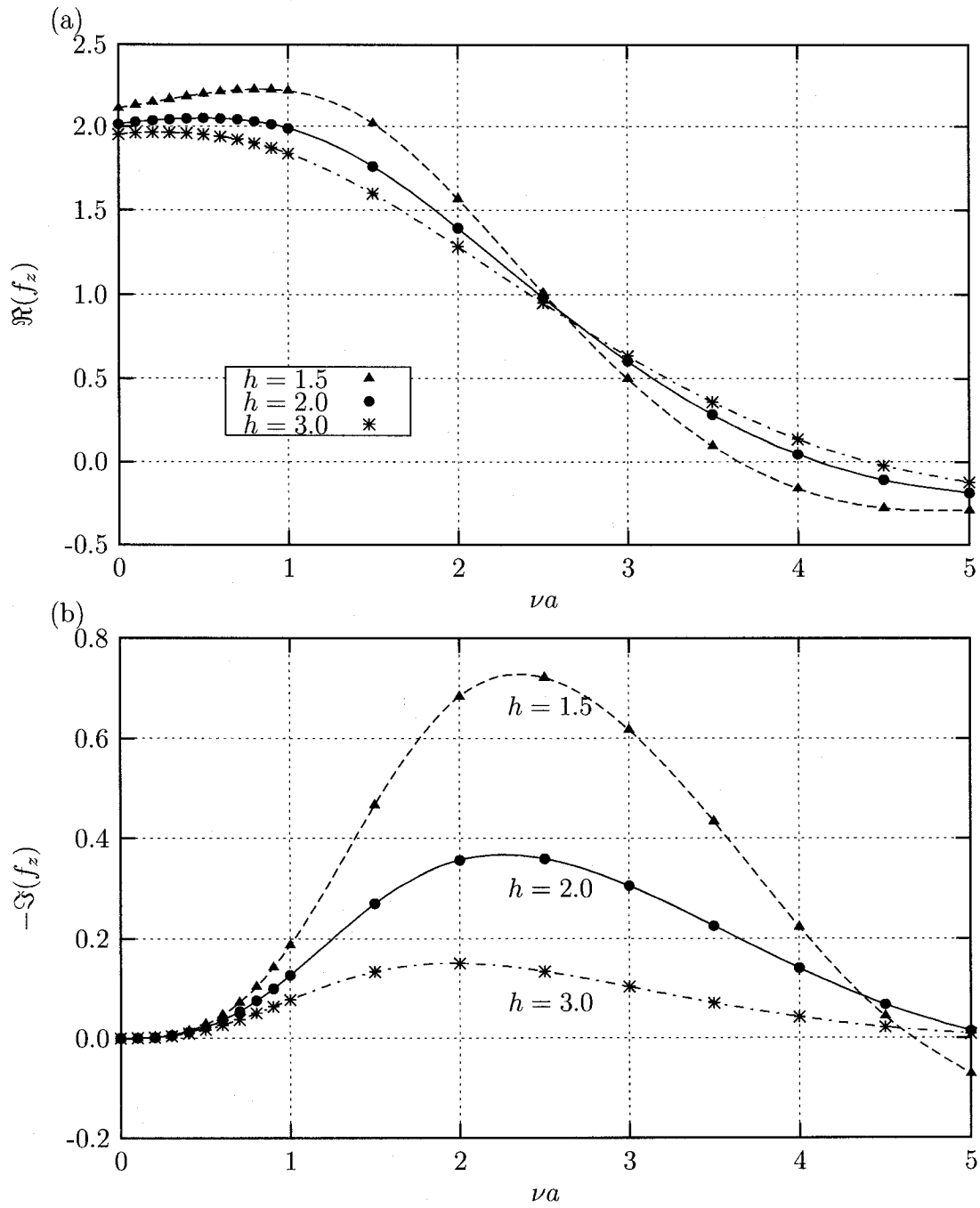

Figure D.2: Numerical results of non-dimensional heave force on a spheroid ($a = 6b$) with 32×32 Gaussian points; (a) Real part, (b) Imaginary part.

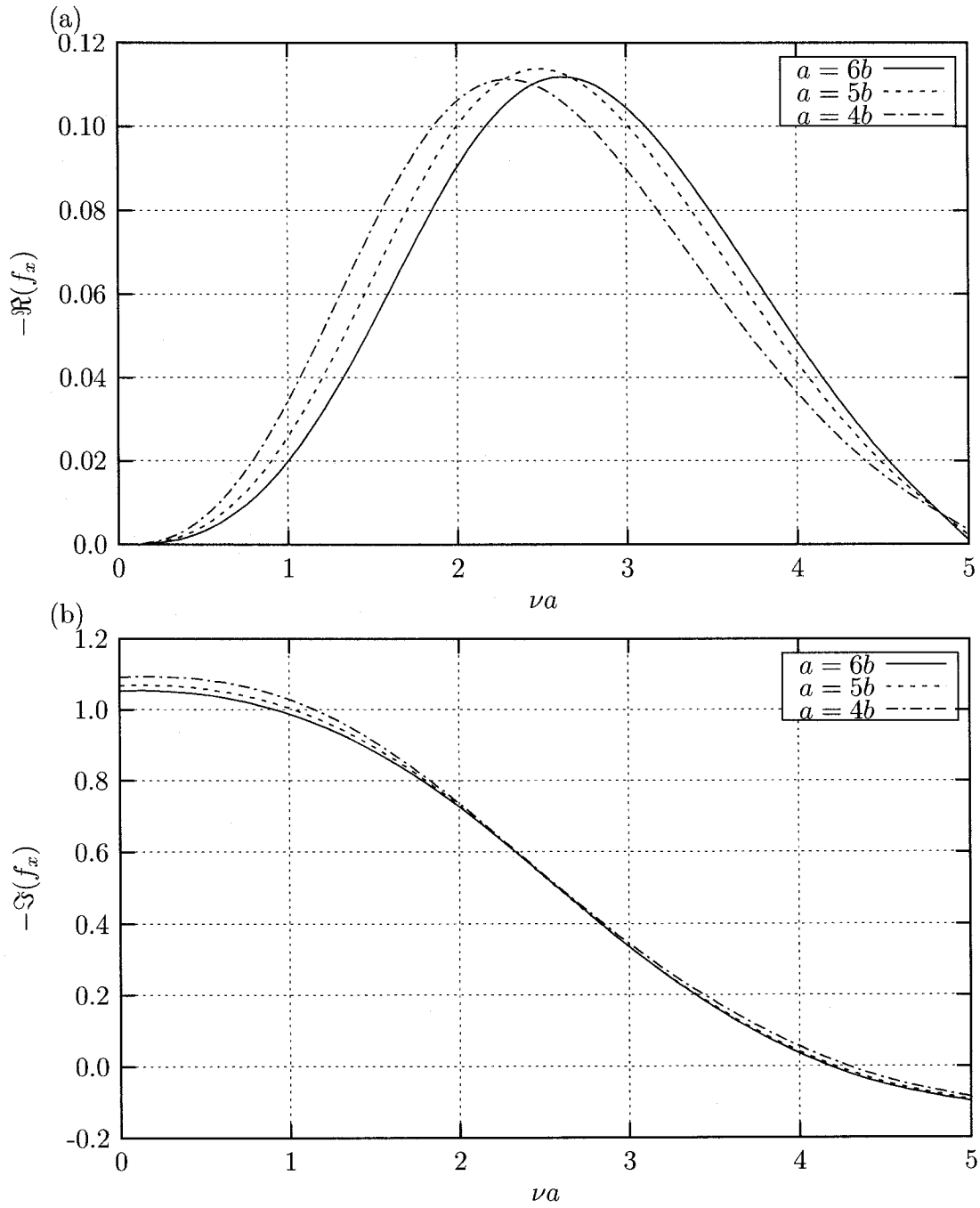

Figure D.3: Numerical results of non-dimensional surge force on spheroid of different aspect ratio a/b and $h = 2b$; (a) Real part, (b) Imaginary part.

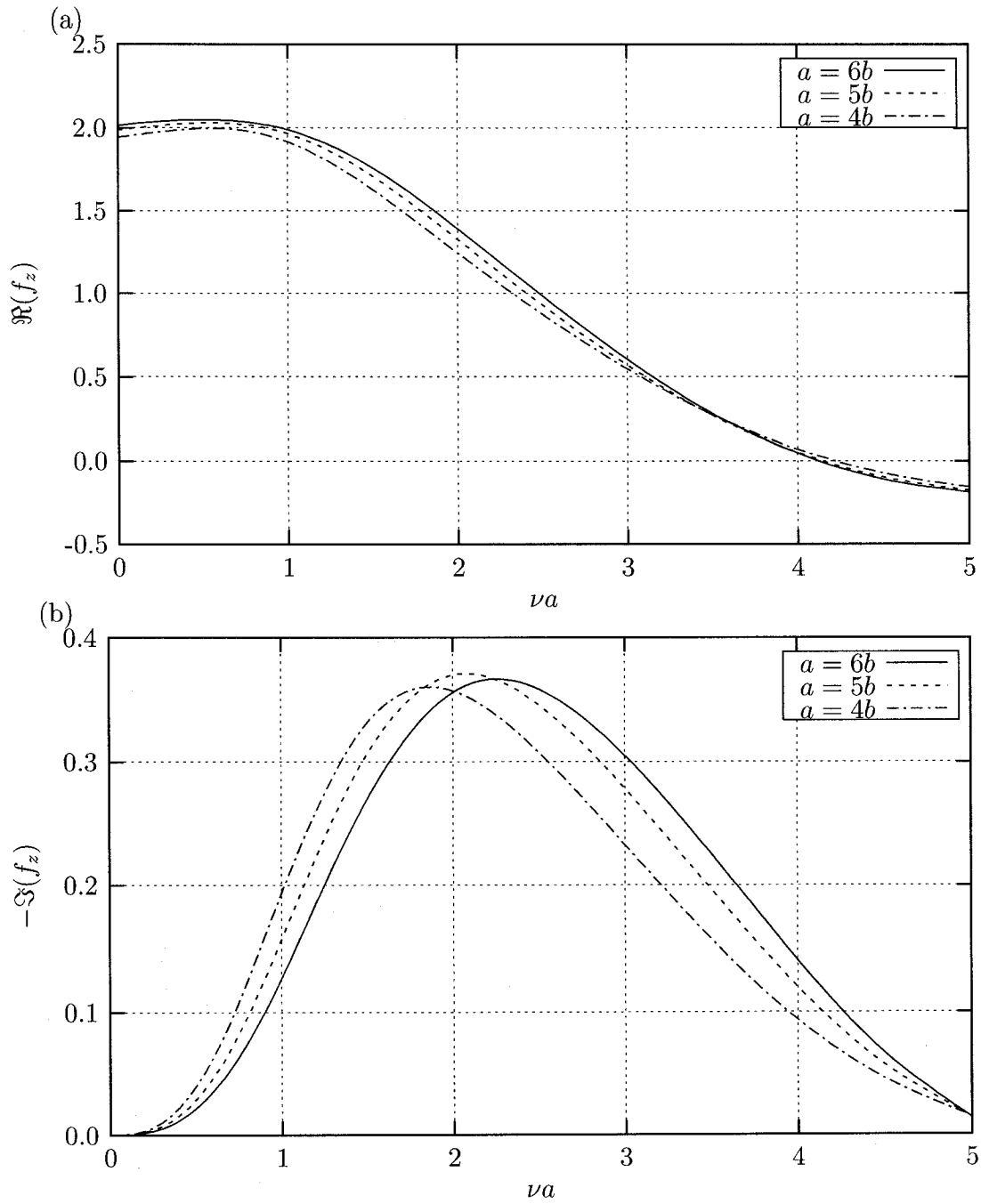

Figure D.4: Numerical results of non-dimensional heave force on spheroid of different aspect ratio a/b and $h = 2b$; (a) Real part, (b) Imaginary part.

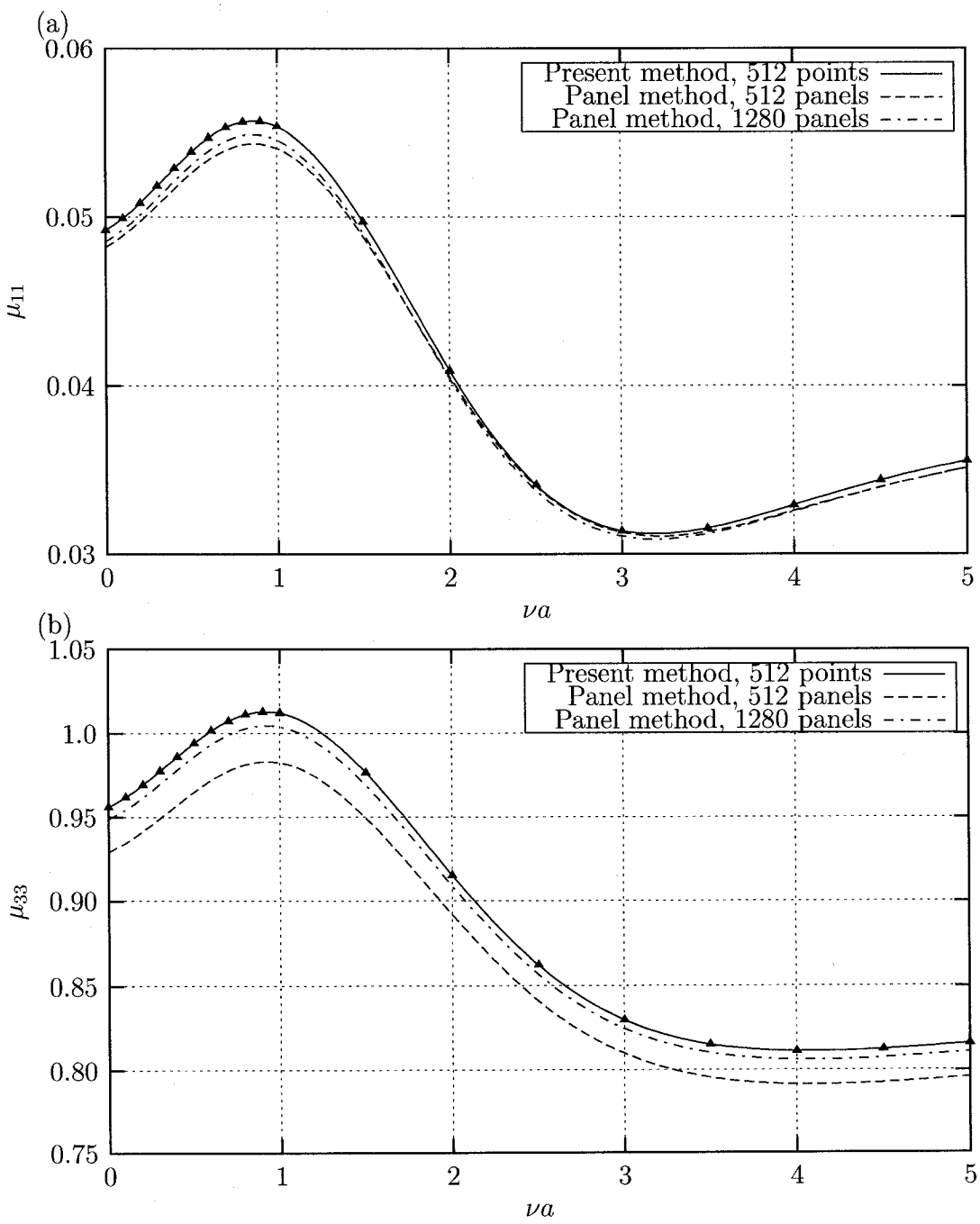

Figure D.5: Surge (a) and heave (b) added-mass of a spheroid; $a = 6b$ and $h = 3b$.

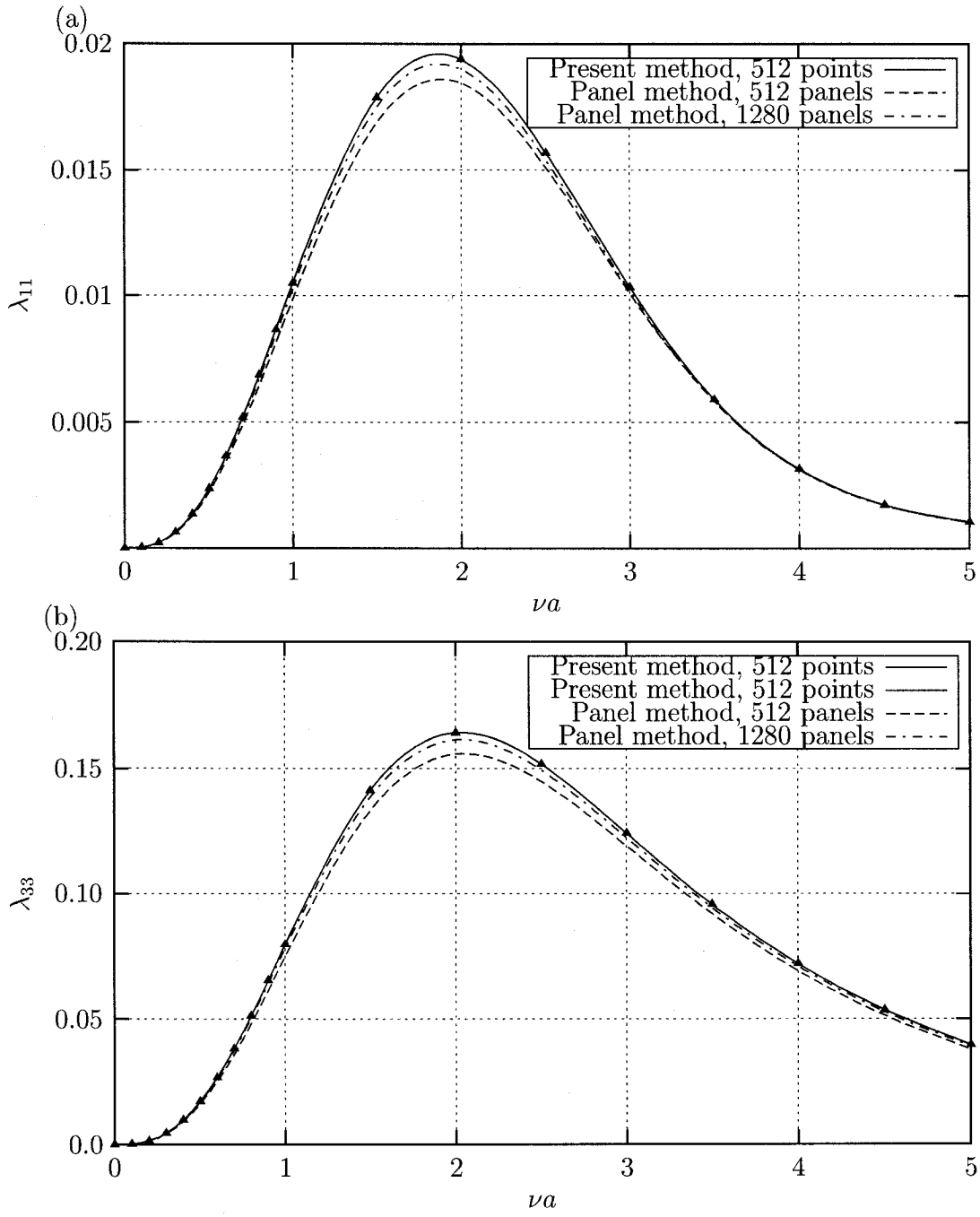

Figure D.6: Surge (a) and heave (b) damping coefficient of a spheroid; $a = 6b$ and $h = 3b$.